

**Chirality Dependent Empirical Modeling of Optical Transitions and Bandgaps in
Carbon Nanotubes and Graphene Nanoribbons**

by

Golam Rasul Ahmed Jamal


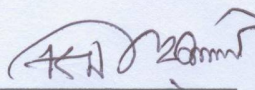
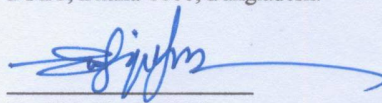
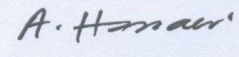
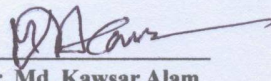
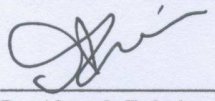
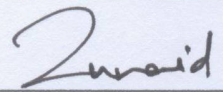
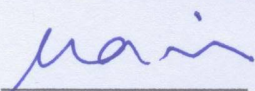
DOCTOR OF PHILOSOPHY

Department of Electrical and Electronic Engineering
BANGLADESH UNIVERSITY OF ENGINEERING AND TECHNOLOGY
May, 2022

CERTIFICATION

The thesis titled “Chirality Dependent Empirical Modeling of Optical Transitions and Bandgaps in Carbon Nanotubes and Graphene Nanoribbons” submitted by Golam Rasul Ahmed Jamal, Roll No.: 1012064002P, Session: October, 2012 has been accepted as satisfactory in partial fulfillment of the requirement for the degree of Doctor of Philosophy on 9 May, 2022.

BOARD OF EXAMINERS

- 
1. **Dr. Sharif Mohammad Mominuzzaman**
Professor
Department of Electrical and Electronic Engineering
BUET, Dhaka-1000, Bangladesh. Chairman
(Supervisor)
- 
2. **Dr. Md. Kamrul Hasan**
Professor and Head
Department of Electrical and Electronic Engineering
BUET, Dhaka-1000, Bangladesh. (Ex-officio)
- 
3. **Dr. Md. Shafiqul Islam**
Professor
Department of Electrical and Electronic Engineering
BUET, Dhaka-1000, Bangladesh. Member
- 
4. **Dr. A. K. M. Akther Hossain**
Professor
Department of Physics
BUET, Dhaka-1000, Bangladesh. Member
- 
5. **Dr. Md. Kawsar Alam**
Professor
Department of Electrical and Electronic Engineering
BUET, Dhaka-1000, Bangladesh. Member
- 
6. **Dr. Ahmed Zubair**
Associate Professor
Department of Electrical and Electronic Engineering
BUET, Dhaka-1000, Bangladesh. Member
- 
7. **Dr. Md. Zunaid Baten**
Associate Professor
Department of Electrical and Electronic Engineering
BUET, Dhaka-1000, Bangladesh. Member
- 
8. **Dr. Kazi Haniun Maria**
Professor
Department of Physics
Dhaka University, Dhaka-1000, Bangladesh. Member
(External)

DECLARATION

It is hereby declared that this thesis or any part of it has not been submitted elsewhere for the award of any degree or diploma.

Signature of the Candidate



Golam Rasul Ahmed Jamal

DEDICATION

To My Parents

ACKNOWLEDGEMENTS

I am grateful to Almighty Allah for giving me the skill and strength to complete this work. I wish to offer my heartiest gratitude and profound respect to my thesis supervisor Dr. Sharif Mohammad Mominuzzaman, Professor, Department of Electrical and Electronic Engineering, Bangladesh University of Engineering and Technology, Dhaka, Bangladesh, for giving me the opportunity to work with him and for acquainting me with the world of advanced research. I am indebted to him for his continuous guidance, suggestions and wholehearted supervision throughout the progress of this work.

I am also indebted to the members of the Doctoral committee who, along with my supervisor, guided me throughout the way by their insightful observations and suggestions. They also extended their efforts to scrutinize the write up in this thesis work thoroughly and suggested necessary corrections and additions. Without those valuable corrections and suggested additions, this work would not take its current form.

I am grateful to the Head of the Department of EEE, BUET, who provided all necessary administrative support from the department to complete this work. My cordial thanks goes to the BPGS secretary, tabulator and all the academic and administrative officers and staffs in EEE Department as well as in CASR office and Exam controller's office for their sincere help in completing various official formalities to submit this thesis work.

Finally, I am grateful to my family members, who always encouraged me to complete this work and supported me throughout the way.

Abstract

Single wall carbon nanotubes (SWCNTs), double wall carbon nanotubes (DWCNTs) and graphene nanoribbons (GNRs) have unique electronic and optical properties. SWCNT is uniquely characterized by two positive integers (n , m), termed as chirality and DWCNT is identified by constituent SWCNTs whereas GNR is identified by type of its cross-section at the edges and number of dimer lines N . Selection of appropriate CNTs or GNRs for various applications requires prior information of their chirality and interband optical transition energies. Each SWCNT has a unique set of interband optical transition energies which depends on their chirality and other factors. Optical transitions of DWCNTs vary according to constituent SWCNTs whereas bandgaps of GNRs vary according to type and width of GNRs. Calculation of optical transitions of CNTs and GNRs from existing models was found to be deviated significantly from experimental results. It also ignored excitonic effects in optical transitions. A set of empirical models is proposed to predict different optical transitions in CNTs and bandgaps of GNRs. Experimental values of optical transitions of a large number of SWCNTs species (4, 2) to (35, 34) having diameter range 0.42 nm to 4.75 nm are considered here. There are total 654 SWCNTs in between these two chiral indices where 426 are semiconducting tubes and 228 are metallic tubes. Besides, DWCNTs and armchair GNRs of different chiralities synthesized and reported so far are studied. Based on the observations and findings, the empirical model is developed that gives a set of effective empirical equations to predict optical transitions in semiconducting and metallic SWCNTs and DWCNTs as well as bandgaps in GNRs with high accuracy. Calculated values from the empirical relations showed excellent agreement with experimental values. Such relations also lead to new method for characterizing CNTs or GNRs after synthesis. Empirical relations and family behavior of SWCNTs are also exploited to find a new technique for chirality assignment of individual SWCNT. Implications of the proposed empirical model in CNT-based devices are also demonstrated.

CONTENTS

Declaration	iii
Dedication	iv
Acknowledgements	v
Abstract	vi
Contents	vii
List of Figures	xi
List of Tables	xvi
Acronyms	xviii
Chapter 1: Introduction	1
1.1 Structure of Single Wall and Double Wall Carbon Nanotubes and Graphene Nanoribbons	1
1.1.1 Single Wall Carbon Nanotubes	1
1.1.2 Double Wall Carbon Nanotubes	3
1.2 Graphene Nanoribbons	4
1.3 Motivation of the Research	5
1.5 Objectives of the Research	6
1.6 Outline of This Dissertation	6
Chapter 2: Optical Transitions in Carbon Nanotubes and Graphene Nanoribbons	7
2.1 Optical Transitions in Single Wall Carbon Nanotubes	7

2.1.1 Optical polarization in SWCNTs	7
2.1.2 Selection rules for optical transitions in SWCNTs	8
2.2 Perpendicular Polarization and Antenna Effect	9
2.3 Optical Transitions in SWCNTs for Parallel Polarization	18
2.3.1 Experimental Observations Regarding Optical Transitions in SWCNTs	20
2.3.2 Factors Contributing Variations of Optical Transitions in SWCNTs	23
2.3.3 Improved Models for Optical Transition of SWCNTs	25
2.3.4 First Principle Calculation of Optical Transitions	26
2.4 Optical Transitions in Double Wall Carbon Nanotubes	31
2.4.1 Introduction to the Structure and Properties of DWCNT	31
2.4.2 Electronic Structure and Bandgaps of DWCNTs	32
2.5 Electronic Structure and Bandgaps in Graphene Nanoribbons	35
2.5.1 Structure and Electronic Properties of GNRs	35
2.5.2 Earlier Models for Calculating Bandgaps in Armchair GNRs	37
2.5.3 Limitations of the Earlier Models for Bandgaps of GNRs	40
2.5.4 Improved Models	42
2.6 Utility of Knowing Optical Transitions in SWCNTs and Bandgaps in GNRs	43
2.6.1 Characterizing SWCNTs and DWCNTs from higher optical transitions	43
2.6.2 Describing Emission Spectra of CNT Based LEDs	44

2.6.3 Selecting Appropriate SWCNTs in CNT based LEDs for Visible and NIR Spectrum	49
Chapter 3: Empirical Modeling of Optical Transitions in SWCNTs	53
3.1 Empirical Modeling of Different Optical Transitions in SWCNTs	53
3.1.1 Semiconducting SWCNTs	53
3.1.2 Metallic SWCNTs:	59
3.1.3 Zigzag SWCNTs	65
3.2 Conclusions	73
Chapter 4: Potential Applications of the Proposed Empirical Models for SWCNTs	75
4.1 Potential Applications of the Proposed Model	75
4.2 Improved technique for chirality assignment of SWCNTs	75
4.2.1 Chirality assignment using the empirical model	76
4.2.2 Assignment of chiral index (n, m) using the proposed method	80
4.2.3 Characterizing SWCNTs and DWCNTs from Higher Optical Transitions using the proposed empirical model	80
4.3 Using Proposed Empirical Model to Describe Emission Spectra of CNT Based LEDs	83
4.4 Empirical calculation of optical transitions for perpendicular polarization of light	85
4.5 Selection of SWCNTs in CNT Based LEDs for Visible and NIR Spectrum Using the Empirical Model	88
4.5.1 SWCNTs for Emitting Light in Visible Spectrum	88
4.5.2 SWCNTs for Emitting Light in CIR (Color Infrared) Spectrum	89

4.6 Conclusions	90
Chapter 5: Many Body Correction for Higher Optical Transitions in Semiconducting SWCNTs	91
5.1 Excitons in SWCNTs	91
5.2 Effect of Excitons on Optical Transitions in SWCNTs	92
5.3 Developing Semi-empirical Model for Many Body Correction in SWCNTs	95
5.4 Conclusions	100
Chapter 6: Empirical Modeling of Inner Tube Optical Transitions in Double Wall Carbon Nanotubes	102
6.1 Zigzag@zigzag DWCNTs	102
6.2 Empirical Model for Optical Transitions of Inner Semiconducting tubes of DWCNTs	105
6.3 Conclusions	114
Chapter 7: Empirical Model for Bandgaps in Graphene Nanoribbons	115
7.1 Experimental Observations Regarding Armchair GNRs	115
7.2 Proposed Empirical Model for Bandgaps of Armchair GNRs	116
CHAPTER 8: Conclusions	123
8.1 Novelty of the Work	123
8.2 Limitations	124
8.3 Future Scopes	124
References	125

List of Figures

Figure 1.1	(a) The unrolled honeycomb lattice of a nanotube. (b) Three different rolling direction of graphene sheet results three different types of nanotubes.	2
Figure 1.2	Double wall carbon nanotube	3
Figure 1.3	The finite-width honeycomb structure of GNRs The lattice of a (a) 6-ZGNR and (b) 9-AGNR	4
Figure 2.1	Sketch of the absorption energy transitions in carbon nanotubes for parallel ($//$) and perpendicular (\perp) light polarization, also called parallel and cross-polarized configuration, respectively	8
Figure 2.2	(a) Schematics of optical transitions in SWNTs corresponding to collinear, parallel- polarized (red and green color) and perpendicular, cross-polarized (blue color) excitations with the directions of the respective transition dipole moments μ_{ij} .	11
Figure 2.3	Absorption and Raman spectroscopy of a free-standing individual (22,6) semiconducting SWNT. (a) Absolute absorption cross-section spectrum for incident light parallel (full dots) and perpendicular (open dots) to the nanotube. (b) Light polarization-dependent absorption cross-section for two laser excitation energies	15
Figure 2.4	a) Polarization-optimized homodyne detection of (24,24) single-walled carbon nanotube. The absolute optical absorption cross-section per carbon atom with both parallel ($//$) and perpendicular (\perp) light polarization to nanotube axis. b)Cutting line scheme of optical transitions between subbands with angular momentum difference of $\pm Z$ in nanotubes	16
Figure 2.5	Polarized photocurrent spectroscopy on a p-n junction. Light polarized parallel (black) and perpendicular (red) to the carbon nanotube axis for (a) E_{11} transition and (b) E_{22} transitions. In both cases, for light polarized perpendicular to the carbon nanotube axis (red) suppresses optical transitions. Inset (a) & (b) angular dependence of the photocurrent (units: pA) on the polarization angle of the excitation light.	18

Figure 2.6	Schematic density of states diagram for a semiconducting single-walled carbon nanotube, in a simple band theory model	19
Figure 2.7	An illustration of Kataura plot. The gray symbols indicate mod 1 (closed circles) and mod 2 (open circles) semiconducting tubes. The lines connect $2n + m$ families	21
Figure 2.8	Comparison of fluorescence spectroscopy result with TB calculation. (a) Measured ratios of excitation to emission frequencies (b) Computed ratio from an extended TB model for mod 1 type (blue) and mod 2 type (red). Solid lines connect families with equal $n - m$ values and dotted line connects $2n+m$ families	22
Figure 2.9	Observed ‘blue shift’ of optical transition energies measured from fluorescence spectroscopy, for mod 1 type ($v = +1$) and mod 2 type ($v = -1$) semiconducting SWCNTs. The solid line gives the prediction of linearized TB model theory.	22
Figure 2.10	Band gaps of (4, 0) to (20, 0) zigzag tubes versus diameter. The squares show TB values, while the diamonds show DFT results.	27
Figure 2.11	Electronic band structure and DOS of the Zigzag a) (6,0) b) (7,0), c) armchair (7,7) and d) chiral (6, 2) nanotubes.	28
Figure 2.12	Electronic band gaps for semiconducting zigzag SWCNT, corresponding to optical transitions. Black discs and white circles are first-principles GW results for mod 1 and mod 2 zigzag CNTs, respectively, compared with theoretical estimates (green line) for generic tubes, for mod 1 (purple line) and mod 2 (brown line) zigzag tubes along with the experimental STS measurement (blue).	29
Figure 2.13	(a) Band gaps of zigzag SWNTs and (b) metallic zigzag (3m,0) SWNTs calculated by B3LYP (blue circles) as a function of diameter and compared with experimental, PBE, LDA and LDA+GW approximation + many-body effects.	30
Figure 2.14	The finite-width honeycomb structure of GNRs. The lattice of a (a) 6-ZGNR and (b) 9-AGNR. The dashed box represents the primitive unit cell. The open circles at the edges denote passivation atoms such as hydrogen. The bold gray lines are the zigzag or armchair chains that are used to determine N_z or N_a respectively.	36

Figure 2.15	Rayleigh and Raman spectra of (a) an armchair M-SWNT assigned to (19,19) or (20,20) (b) a near zigzag semiconducting SWNT assigned to (20,3) or (21,1). Rayleigh spectra of (c) a single undoped nanotube assigned to (26,0) or (25,2) (d) (7,6)@(16,6) DWCNT and (e) (10, 6)@(14, 13) DWCNT.	44
Figure 2.16	Structure and characteristics of a CNT light-emitting diode. (a) Schematic diagram illustrating the structure of an asymmetrically contacted CNT device. (b) EL spectrum of the diode when operated at large forward bias.	45
Figure 2.17	Device structure and electronic characteristics. (a) Schematic of the carbon nanotube LED. (b) Electroluminescence spectrum of a nanotube diode at the device. (c) Comparison between electroluminescence spectra at two different gate biases (normalized) for the same device with different SWCNT.	46
Figure 2.18	Structure and operation principle of CNT LED arrays. a) SEM image showing serpentine-CNT-based diode arrays on quartz. b) EL spectrum obtained from the CNT-diode-array device. This spectrum can be fitted by using two Gaussian functions (red lines) that peak at 0.85 and 0.94 eV. The lower peak corresponds to E_{11} of the SWCNT.	46
Figure 2.19	(a) Schematic cross section of the (9,7)-nanotube device. (b) Evolution of the electroluminescence spectra with driving power of (9,7)-CNT device.	47
Figure 2.20	Photoluminescence spectra from 10 adjacent devices on a (9,7) SWCNT array, for 800 nm excitation wavelength. Each shows emission at 1345 nm, indicating the presence of a (9,7) SWCNT.	48
Figure 2.21	a) Absorption and photoluminescence (PL) spectra of the (6,5) SWCNTs used as emitter material. The inset shows the molecular structure of a (6,5) SWCNT. b) Schematic illustration for the OLED stack used by Graf <i>et al.</i>	48
Figure 2.22	Human spectral sensitivity to color	50
Figure 2.23	Color Infrared (CIR) Spectrum	51

Figure 3.1	First seven optical transition energies of semiconducting SWCNTs, plotted against their diameters (Experimental ‘Kataura plot’) separately in (a) for odd transitions and in (b) for even transitions. Mod 1 type transitions (blue) form lower branches in odd transitions and upper branches in even transitions. Mod 2 type transitions (green) form lower branches in even transitions and upper branches in odd transitions.	55
Figure3.2	Experimental (black dot) and empirical (green circle) values of first seven optical transitions, plotted against diameters of semiconducting SWCNTs in (a) for four odd transitions and in (b) for three even transitions.	58
Figure 3.3	Experimental value(black), the empirical value from this work(red) and the empirical value from earlier work (blue) of optical transition vs diameter of armchair SWCNTs, a) the second optical transition, b) the third optical transition.	64
Figure 3.4	Experimental Kataura plot. The lines connect $2n + m$ families of both mod 1 and mod 2 type SWCNTs.	68
Figure 3.5	Experimental value(blue dot) and empirical value from this work(red cross) for (a) first transition (E_{11}) and (b) second transition (E_{22}) energies of semiconducting zigzag and nearly zigzag SWCNTs.	70
Figure 3.6	Experimental value(blue dot) and empirical value from this work(red cross) for (a) third transition (E_{33}) and (b) fourth transition (E_{44}) energies of semiconducting zigzag and nearly zigzag SWCNTs.	71
Figure 3.7	Experimental value(blue dot) and empirical value from this work(red cross) for fifth transition (E_{55}) energies of semiconducting zigzag and nearly zigzag SWCNTs.	72
Figure 4.1	Experimental G- shift [141] against calculated d_t from experimental ω_{rbm} [141] for 13 SWCNTs. Dot (blue) shows individual SWCNT and solid lines (black) connect members of same $(2n+m)$ family.	78
Figure 4.2	Empirical E_{22} from proposed model against calculated d_t from experimental ω_{rbm} [141] for 13 SWCNTs. Dot (red) shows individual SWCNT and solid lines (black) connect members of same $(2n+m)$ family.	78

Figure 4.3	Calculated nanotube absorption cross sections cross sections for parallel (solid line) and perpendicular with (dashed line) and without (dotted line) a depolarization correction.	86
Figure 5.1	Experimental value(black dot), calculated value from this work (green triangle) and many body correction (blue dot) of 5 th , 6 th and 7 th optical transitions in (a), (b) and (c), respectively, plotted vs diameter of semiconducting SWCNTs.	99
Figure 6.1	Empirical values of five optical transitions of inner semiconducting tubes of S@M and S@S DWNTs compared with experimental data with respect to average diameter of the DWNTs.	113
Figure 7.1	Measured and calculated bandgaps of AGNRs vs ribbon width including the result from empirical equations. The calculated and experimental bandgaps for AGNRs are taken from different reports.	119

List of Tables

Table 3.1	Parameters A and B for different optical transitions of semiconducting SWCNTs	57
Table 3.2	Experimental and the empirical values of the second optical transition energy of 16 armchair SWCNTs	62
Table 3.3	Experimental and the empirical values of the third optical transition energy of 13 armchair SWCNTs	63
Table 3.4	Parameters A and B for different optical transitions of semiconducting zigzag SWCNTs	69
Table 4.1	Assignment of chiral index (n, m)	81
Table 4.2	Reported chirality assignment of CNTs and validation from proposed empirical model	82
Table 4.3	SWCNTs for emitting light in visible spectrum	88
Table 4.4	SWCNTs for emitting light in CIR spectrum	89
Table 5.1	Fitting parameters for 5 th , 6 th and 7 th optical transitions of semiconducting SWCNTs	98
Table 6.1	Possible combinations of inner and outer tubes of Double Wall Carbon Nanotubes	104
Table 6.2	Optical transitions in Inner Semiconducting Tubes (ISCT) of DWNTs and corresponding isolated SWCNTs of same chirality	107
Table 6.3	Parameters A and B for different optical transitions of ISCTs of DWNTs	110

Table 6.4	Optical transitions in Inner Semiconducting Tubes (ISCT) of DWNTs calculated from the proposed empirical model	111
Table 7.1	For AGNRs with $N=3p$	117
Table 7.2	For AGNRs with $N=3p+1$	118
Table 7.3	SWCNTs and AGNRs for emitting light in visible Spectrum	120
Table 7.4	SWCNTs and AGNRs for emitting light in CIR Spectrum	121

ACRONYMS

CNT	Carbon Nanotube
SWCNT	Single-Wall Carbon Nanotube
DWCNT	Double-Wall Carbon Nanotube
MWCNT	Multi-Wall Carbon Nanotube
ISCT	Inner Semiconducting Tube
GNR	Graphene Nanoribbon
AGNR	Armchair Graphene Nanoribbon
ZGNR	Zigzag Graphene Nanoribbon
TB	Tight Binding
QM	Quantum Mechanical
DFT	Density Functional Theory
LDA	Local Density Approximations
B3LYP	Becke -Lee -Yang Parr
GWA	GW Approximations
IC	Image Charge
RRS	Resonant Raman Spectroscopy
PL	Photoluminescence
TEM	Transmission Electron Microscopy
STM/STS	Scanning Tunneling Microscopy/Spectroscopy

CHAPTER 1

INTRODUCTION

Carbon nanotubes (CNTs) and graphene nanoribbons (GNRs) are two most intensively studied materials in current decade [1-4]. For their unique nanostructure and extraordinary electronic, optical, mechanical and chemical properties, both CNTs and GNRs are considered as ideal building block of next-generation electronic devices and circuits. The research effort devoted by both academic and industrial community has induced a great advance of the science and technology for CNTs and GNRs including their synthesis, property and device applications. It is becoming evident that CNTs and GNRs have the ability to replace silicon in electronic devices that dominates the present data driven world [1-4].

1.1 Structure of Single Wall and Double Wall Carbon Nanotubes and Graphene Nanoribbons

1.1.1 Single wall carbon nanotubes

Carbon nanotubes can be single-walled, double-walled or multi-walled. First two categories can be either semiconducting or metallic depending on their geometrical structure whereas the third category is always metallic [1, 2].

A single wall carbon nanotube (SWCNT) can be viewed as a hollow cylinder formed by rolling graphite sheets. Bonding in CNTs is essentially sp^2 . When a graphene sheet is rolled over to form a nanotube, the sp^2 hybrid orbital is deformed for rehybridization of sp^2 toward sp^3 orbital or σ - π bond mixing. This re-hybridization structural feature, together with π electron confinement, gives nanotubes' unique properties. Consequently, nanotubes are electrically and thermally more conductive, mechanically stronger and chemically and biologically more active than graphite [1, 5, 6].

The structure of a single wall carbon nanotube (SWCNT) can be uniquely characterized by a vector \mathbf{C}_h in terms of two positive integers (n, m), $\mathbf{C}_h = n\mathbf{a}_1 + m\mathbf{a}_2 \equiv (n, m)$, as shown in Fig. 1.1(a).

Where, a_1 and a_2 are the basis vectors of graphite lattice separated by 60° . The SWCNT is constructed by rolling up the sheet such that the two end-points of the vector C_h are superimposed. The vector C_h connects two crystallographically equivalent sites O and A on a two-dimensional (2D) graphene sheet. When the line AB' is joined to the parallel line OB in Fig.1.1 (a), a seamlessly joined SWCNT classified by the integers (n, m) is found, since the parallel lines AB' and OB cross the honeycomb lattice at equivalent points. C_h is also termed as the circumferential vector. The direction of SWCNT axis corresponds to OB .

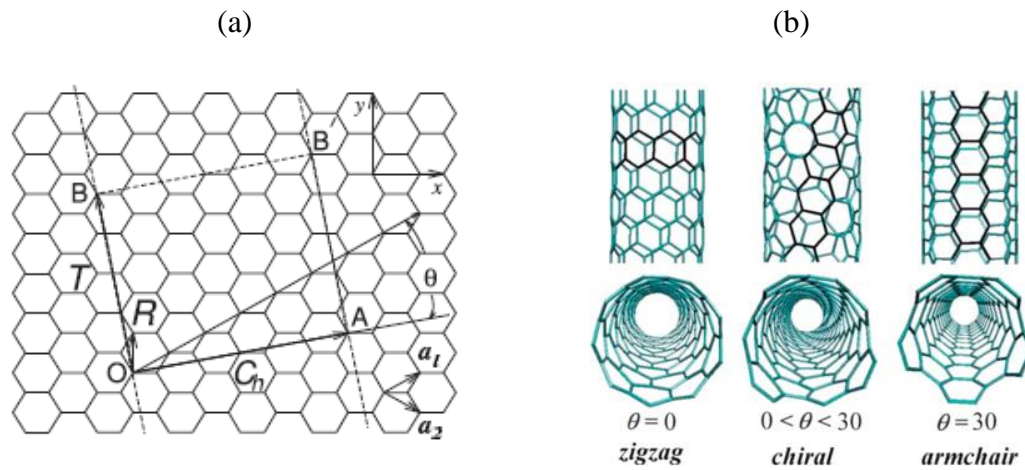


Figure 1.1: (a) The unrolled honeycomb lattice of a nanotube. (b) Three different rolling direction of graphene sheet results three different types of nanotubes [6].

Three categories of SWCNTs can be formed, as shown in Fig.1.1 (b): the armchair (n, n) , the zigzag $(n, 0)$, and the chiral (n, m) with $n > m > 0$. When the circumferential vector C_h is along the direction exactly between the two basis vectors, $n = m$, C-C bonds become perpendicular to the tube axis and the carbon nanotube is said to be of “armchair” type. When the circumferential vector C_h lies purely along one of the two basis vectors, $m=0$, C-C bonds become parallel to the tube axis and the carbon nanotube is said to be of “zigzag” type. Any other directions of circumferential vector results ‘chiral’ type nanotube [1, 5, 6].

The diameter of a (n, m) nanotube d_t is given by, $d_t = L/\pi = a_0 \sqrt{(n^2 + nm + m^2)} / \pi$, where, $a_0 =$ length of graphite basis vector (lattice constant) $= |a_1| = |a_2| = \sqrt{3}a_{cc} = 0.249$ nm with $a_{cc} =$ C–C bond length $= 0.144$ nm and $L = |C_h| =$ length of the chiral vector C_h .

The chiral angle (θ) is defined as the angle between the chiral vector \mathbf{C}_h and the zigzag direction \mathbf{a}_1 , $\theta = \tan^{-1} \frac{\sqrt{3}m}{2n+m}$. For zigzag, armchair and chiral nanotubes, Chiral angle, $\theta = 0^\circ$, $\theta = 30^\circ$, and $0 \leq |\theta| \leq 30^\circ$, respectively.

In terms of electronics property, a SWCNT (n, m) will be metallic if its $n-m = 3k$ (k is integer), i.e. $\text{mod}(n-m, 3) = 0$ and it will be semiconducting if its $n-m \neq 3k$, i.e. $\text{mod}(n-m, 3) = 1$ or 2 [7]. This relation is always found true except for SWCNT with very small diameter, where curvature effect dominates its properties [8, 9]. This relation indicates that theoretically two third of the total SWCNTs are semiconducting and one third are metallic.

1.1.2 Double wall carbon nanotubes

A double wall carbon nanotube (DWCNT) is made of two concentric SWNT-equivalent nanotubes with an inter-wall spacing < 0.5 nm [2, 10], as shown in Fig. 1.2. Electronic band gap of the DWNTs depend on the interwall distance as well as on the chirality and intrinsic properties of the constituent SWCNTs [11]. However, the electronic properties of DWNTs may not be a simple superposition of the electronic properties of inner and outer layer. The inter-wall distance may also affect the electronic properties of a DWNT. Interwall distance and average diameter of DWNT can be calculated from chirality of constituent SWCNTs. For a DWNT, average diameter, $D = \frac{1}{2}(d_o + d_i)$, and inter wall

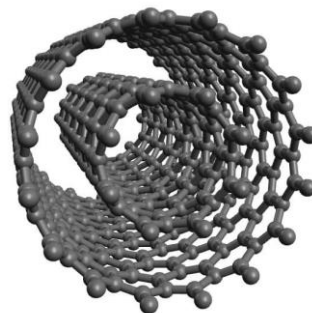


Figure 1.2: Double wall carbon nanotube [2]

separation, $w = \frac{1}{2}(d_o - d_i)$, where, d_o and d_i are outer tube and inner tube diameter, respectively.

1.2 Graphene Nanoribbons

Graphene is a two-dimensional (2D) monolayer honeycomb structure of carbon [12]. Graphene nanoribbons (GNRs) are strips of graphene with ultra-thin width on the order of nanometers up to tens of nanometers. The nanoribbons can have arbitrarily long length and, as a result of their high aspect ratio, they are considered quasi-1D nanomaterials. GNRs are a relatively new class of nanomaterials that can have metallic or semiconducting character, and are currently being investigated for their interesting electrical, optical, mechanical, thermal, and quantum-mechanical properties [3].

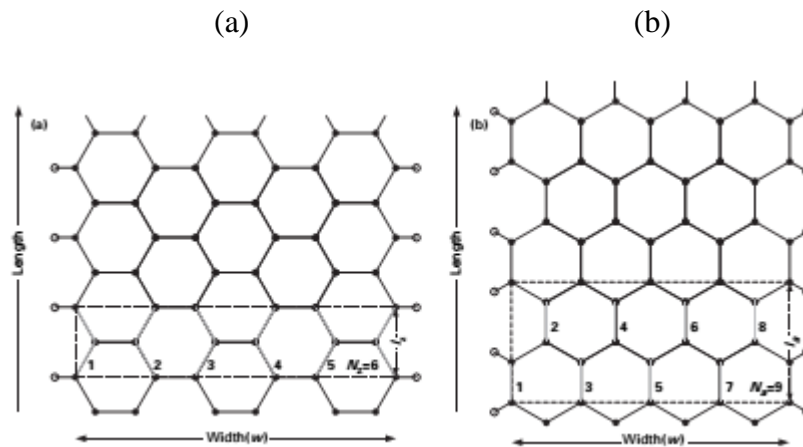


Figure 1.3: The finite-width honeycomb structure of GNRs The lattice of a (a) 6-ZGNR and (b) 9-AGNR [3].

There are two types of ideal GNR, which are called armchair GNRs (AGNRs) and zigzag GNRs (ZGNRs). The AGNR has an armchair cross-section at the edges, while the ZGNR has a zigzag cross-section, both illustrated in Fig. 1.3. In addition, the GNRs are also labeled by the number of armchair or zigzag chains present in the width direction of the AGNR and ZGNR respectively. If N_a be the number of armchair chains and N_z the number of zigzag chains, then the nanoribbon can be conveniently denoted as N_a -AGNR and N_z -ZGNR respectively. The three types of AGNR are determined from whether $N_a = 3p$ or $N_a = 3p + 1$ or $N_a = 3p + 2$, where p is a positive integer.

Earlier theoretical studies [13-15], mainly based on simple tight-binding (TB) approximations, predicted that GNRs can be either metallic or semiconducting depending on GNR types. As per TB calculations, zigzag-edged GNRs are all metallic regardless of their widths, and armchair-edged N_a -AGNR is metallic if $N_a = 3p + 2$ (where p is a positive integer) otherwise, it is semiconducting [3, 15].

Recently, both theoretical and experimental works have shown that quantum confinement and edge effects introduce a band gap in narrow GNRs independent of their chirality [3]. According to first-principles calculations there are no metallic nanoribbons [15]. Density functional theory (DFT) calculation clearly showed that all zigzag-edged and armchair-edged GNRs have a finite band gap [3] and this energy gap depends strongly on the width of the channel for GNRs [15]. Sub-10 nm GNRs with smooth edges were obtained recently and demonstrated to be semiconductors with band gap inversely proportional to w [3]. All the sub-10-nm GNRs were found semiconducting with adequate bandgaps [3].

1.3 Motivation of the Research

Each SWCNT has a unique set of interband optical transition energies that depend on their chirality. Optical transitions of DWCNTs vary according to constituent SWCNTs whereas bandgaps of GNRs vary according to type and width of GNRs. Both CNTs and GNRs are highly sensitive to their chirality and a slight change in chirality can drastically changes their electronic properties. Besides, any application of CNTs or GNRs in the field of electronics or optoelectronics requires prior information of their optical transition energies. Hence, accurate calculation of their optical transition energies is a necessity. Calculation of optical transitions of CNTs and GNRs from existing models was found to be deviated significantly from experimental results. This motivated us to develop a set of empirical models to predict different optical transitions in CNTs and bandgaps of GNRs. Proposed empirical relations and family behavior of SWCNTs can be also exploited to find a new technique for chirality assignment of individual SWCNT. The proposed empirical model help in selecting appropriate CNT and GNR for relevant applications and can predict the absorption and emission in CNT-based devices.

1.4 Objectives of the Research

The objectives of this research are,

- i. To develop empirical relations of inter-band optical transitions of semiconducting and metallic SWCNTs and DWCNTs with their physical structures denoted by chirality.
- ii. To formulate empirical relations for bandgaps of armchair GNRs.
- iii. To validate proposed model by comparing estimated results from this work with relevant experimental reports.
- iv. To demonstrate the potential of the proposed empirical model in selecting appropriate CNT and GNR for relevant applications and predicting the absorption and emission in CNT-based devices.

1.5 Outline of the Dissertation

Succeeding chapters of this dissertation are organized to provide background theory, related previous works and the methodology and results of proposed empirical models. In order to build the context of present work, chapter-2 will give the detailed background and previous works that lead to the necessity of developing proposed empirical models. The empirical models for optical transitions in SWCNTs are developed in Chapter-3 and Chapter-5 and the empirical models for bandgaps in DWCNTs and AGNRs are developed in Chapter-6 and Chapter-7, respectively. Besides, potential applications of the proposed empirical models are presented in Chapter-4. Finally, the overall conclusions, limitations of this work and future scopes are presented in chapter-8.

CHAPTER 2

OPTICAL TRANSITIONS IN CARBON NANOTUBES AND GRAPHENE NANORIBBONS

2.1 Optical Transitions in Single Wall Carbon Nanotubes

Electronic and optical properties of single-wall carbon nanotubes (SWCNT) are directly associated with their geometrical structures [4-6] which are uniquely specified by a pair of chiral index (n, m) . A SWCNT (n, m) will be metallic if its $n-m = 3k$ (k is integer), i.e. $\text{mod}(n-m, 3) = 0$ and it will be semiconducting if its $n-m \neq 3k$, i.e. $\text{mod}(n-m, 3) = 1$ or 2 [7]. This relation gives two types of semiconducting SWCNTs, mod 1 type and mod 2 types, except for very small diameter tubes [7], where curvature effect dominates [8, 9]. Also, this relation indicates that theoretically two third of the total SWCNTs are semiconducting and one third are metallic.

Accurate information of various optical transition energies of single-wall carbon nanotubes (SWCNTs) has been always a necessity for their characterization and potential applications as well as for pure theoretical interest about their internal band structure. The one-dimensionality of the nanotubes gives rise to 1D sub-bands instead of one wide electronic energy band in nanotube density of states (DOS), as shown in Fig. 2.1. Each SWCNT (n, m) has a unique set of interband transition energies E_{ij} denoting the energy differences between the i -th conduction and j -th valence bands and optical transitions can only occur between these sub-bands [7, 8]. These singularities are unique feature of nanotubes and also primarily responsible for many distinguished electronic and optical properties of SWCNTs. Due to the one-dimensional nature of SWCNTs, their optical responses are strongly dependent on the polarization direction of the incident light with respect to the nanotube axis. The next section will highlight this matter in details.

2.1.1 Optical polarization in SWCNTs

SWCNTs are extremely anisotropic which leads to significantly differing polarizabilities for external fields applied parallel and perpendicular to the tube axis. Therefore, light polarization can be used as an external parameter for tuning the optical properties of

nanotube-based optoelectronic devices. This is of importance since, in this case, internal changes to the device will not be needed, and the orientation of the device with respect to the incident light can modify the wavelength of absorption or emission.

2.1.2 Selection rules for optical transitions in SWCNTs

To properly predict, model, and interpret the optical properties of SWCNTs in their respective spectra in processes like optical absorption and Raman scattering, it needs to be known which optical transitions are allowed between which energy states [16].

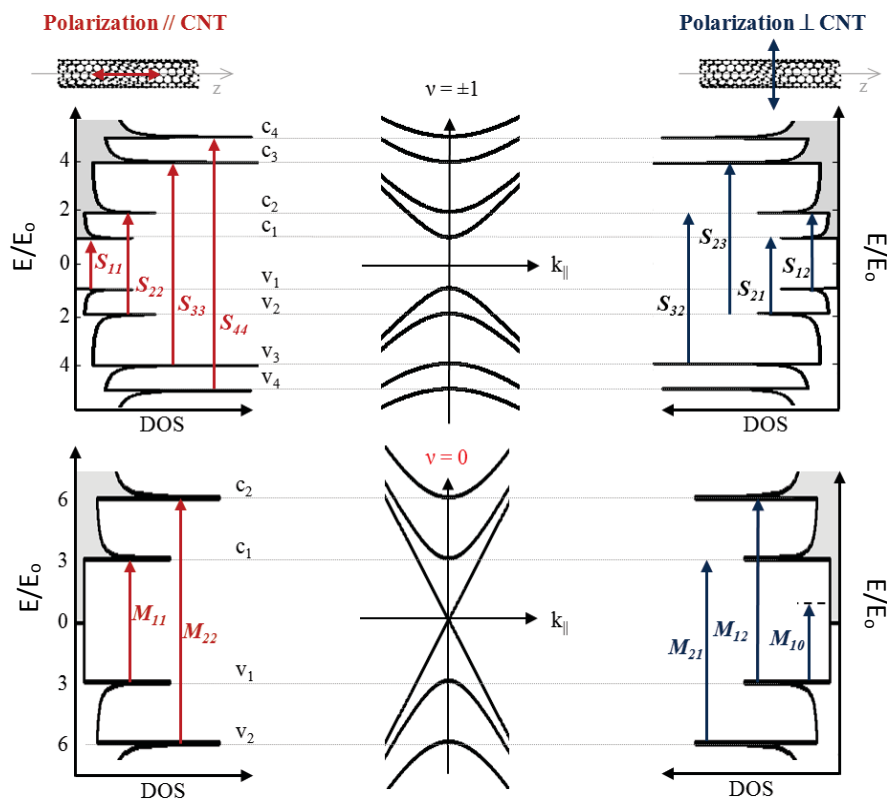


Figure 2.1: Sketch of the absorption energy transitions in carbon nanotubes for parallel (//) and perpendicular (\perp) light polarization, also called parallel and cross-polarized configuration, respectively [17].

Using the $k \cdot p$ method [17], Ajiki and Ando [18] first predicted the allowed optical transitions and optical conductivities for SWCNT. According to their calculation, interband transitions between the massive, hyperbolic bands of the valence and conduction bands, with the same band index, q , are allowed if the polarization of the incident light is parallel to the nanotube axis. Subsequent theoretical calculations [19-27] and experimental observations [28-37] also support this. However, interband optical

transitions between the massless, linear bands are not allowed for any light polarization due to symmetry. In the case where the polarization of the excitation is perpendicular to the nanotube axis, interband transitions are allowed only between bands where the band index changes by 1, i.e., $\Delta q = \pm 1$ for both massive and massless bands [16, 17].

Similar selection rules are arrived at by Milosevic *et al.* [19] using a group theoretical approach. Subsequently, Jiang *et al.*, [20] using the tight-binding method, calculated the electric dipole matrix elements (whose square is proportional to optical absorption), yielding analytical expressions as a function of chiral index and wavevector, k . By examining the k -dependence of the matrix element, they found that the dipole matrix element reaches a maximum for k -values that coincide with the positions of the van Hove singularities (VHS) in the electronic density-of-states for each band. As a result, the strong optical absorption observed in nanotubes is a result of the combination not only of the singularity in the density-of-states but also the coinciding maxima in dipole matrix elements. Additionally for armchair SWCNTs, it was shown that the dipole matrix element is zero for all bands at the $k = 0$ point, indicating a node in optical absorption for armchair species due to their high symmetry.

The absorption energy transitions, including the selection rules, are sketched in Fig. 2.1 where both conduction and valence bands are labeled with i (or j) starting from the Fermi level. Energy transitions are denoted by E_{ij} with $i, j = \{1, 2, 3, 4, \dots\}$ corresponding to the transitions between the v_i valence subband and the c_j conduction subband. More particularly, in semiconducting and metallic tubes they are labeled S_{ij} and M_{ij} , respectively [17].

2.2 Perpendicular Polarization and Antenna Effect

For a perpendicular electric field, the induced charges on the surface of the nanotube produce a depolarizing field inside the nanotube that largely cancels the external field [18-27]. Such local field suppression does not occur in the parallel field because the induced charges occur only at the ends of the nanotube. Assimilating the CNT to an infinite cylinder, this phenomenon can be understood in the static approximation; the incident E-field creates surface charges as shown in Fig. 2.1 (top), and consequently a depolarization field opposing the incident one is induced on the surface of the nanotube.

In other words, the self-consistently induced charge appearing on the surface of a SWNT in the presence of an electric field perpendicular to the nanotube axis cancels the field of the incident light resulting strong damping of perpendicular-polarized absorption [17]. This self-consistent screening effect depends on the geometry of the nanotubes, and it is thus expected that in a SWNT bundle the screening effect is not perfect, since the depolarization field from the neighboring nanotubes may smear out the perfect cancellation of the electric field that occurs for isolated SWNTs in vacuum [21]. Even for an isolated SWNT on SiO₂ surface, this perfect cancellation might not occur because of the surface effect of the dielectric Si substrate.

This depolarization effect (also called antenna effect) was first described theoretically by Ajiki and Ando [18] combining a tight-binding model and the electrostatic argument. Jiang *et al.* [20] reached similar conclusions for polarization perpendicular to the tube axis, with the further refinement that only transitions between “linear” and parabolic bands are significant in intensity as they are allowed everywhere in k -space. Transitions between massive bands around k -points near the VHSs, however, are heavily suppressed due to the appearance of nodes in the dipole matrix elements at the positions of the VHS. Due to this depolarization effect, perpendicular transitions are expected to be heavily suppressed, although excitonic effects are predicted to retain this transition as a well-defined peak in absorption at a renormalized energy [16].

Compared with the works on parallel-polarized excitation, there are relatively less theoretical and experimental works on perpendicular-polarized excitation. As for the previous theoretical works on cross-polarized excitonic resonances, Ando’s group [18, 22-24] has taken much attribute into the depolarization effect by involving both the screening effect and the dynamical screening effect on interband Coulomb interactions (ICIs). They have also reported the obvious depolarization effect, such as the lower intensity compared with the longitudinal situations and the blue shift of excitation peaks.

Grüneis *et al.* [21] analyzed previously published RBM Raman spectra of SWCNTs and assigned the features that could only be explained by optical transitions with light polarization perpendicular to the SWNT axis. Considering relatively small transition energies, they neglected both the trigonal warping effect and the electron–hole asymmetry and used the following simplification: $E_{12}^S = (E_{22}^S + E_{11}^S)/2$. Thus, the resonance energy E_{12}^S for perpendicular polarization appears in the energy gap of E_{11}^S and E_{22}^S .

Uryu *et al.* [22, 23] systematically studied the exciton absorption for perpendicular light with emphasis on the depolarization effect and dependence on the strength of the Coulomb interaction and the tube diameter. Although a strong depolarization effect tends to shift the position to the higher energy side and suppress the intensity, excitons manifest themselves as prominent peaks because of their large binding energy. The resulting absorption energy is closer to that associated with that of the second gap for light polarized parallel to the axis.

Kilina *et al.* [25] investigated computationally and analyzed in detail the properties of all fundamental excitonic bands arising from E_{11} , E_{12} , and E_{21} single-particle transitions in eight species of SWNTs (Fig. 2.2). The results of their simulations show intricate details of excited state properties in carbon nanotubes focusing on the electronic states corresponding to the cross-polarized transitions responsible for transverse optical

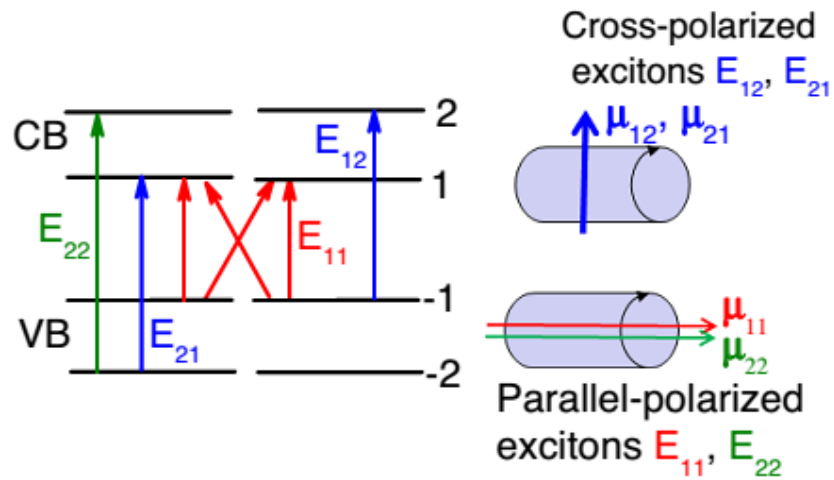


Figure 2.2: Schematics of optical transitions in SWCNTs corresponding to collinear, parallel- polarized (red and green color) and perpendicular, cross-polarized (blue color) excitations with the directions of the respective transition dipole moments μ_{ij} [25].

absorption in nanotubes. Because of degeneracy of the corresponding molecular orbitals, each considered transition between the van Hove singularities gives rise to four distinct excitonic bands. Excitations originating from E_{11} and E_{12}/E_{21} transitions have transition dipole moments parallel- and cross-polarized to the tube axis, respectively. However, most of these transitions are optically forbidden (dark). They observed a single, strongly optically allowed excitation related to the E_{11} transition and two near degenerate, weakly allowed excitations related to the E_{12} and E_{21} transitions. Such properties driven by excitonic effects are dramatically different from predictions of the one electron theory assigning the cross-polarized transition to be exactly in the middle between E_{11} and E_{22} transitions. The distribution of the transition density matrix along a tube axis is similar for all excitons. However, four parallel-polarized excitons associated with the E_{11} transition are more localized along the circumference of a tube, compared with others related to the E_{12} and E_{21} cross-polarized transitions. Calculated splitting between optically active parallel- and cross-polarized transitions increases with tube diameter, which compares well with experimental spectroscopic data.

Motavas *et al.* [26] studied the effect of light polarization on the interband optical transition spectra of nanotubes, independently from the depolarization effect. Using density functional theory, they calculated the absorption spectra of periodic zigzag carbon nanotubes for parallel and perpendicular polarization of light in a wide, infrared-visible-ultraviolet range (0– 11 eV). Their results showed an overall suppression of the transition rate spectra for perpendicular polarization compared to those for parallel polarization in all three nanotubes under investigation, although at certain photon energies (ultraviolet) the probability of absorption for perpendicular light turned out to be surprisingly high. This can be important in optoelectronic applications of carbon nanotubes for ultraviolet absorption and emission.

H. Liu *et al.* [27] derived analytical equations for incident light polarized perpendicular to the tube axis that involve various screened interband Coulomb interactions (ICIs). The strong screening effect on direct ICIs is taken into account in the perpendicular polarized linear excitonic absorption spectra. The calculated E_{12} peak for incident light polarized perpendicular to the tube axis is very close to the longitudinal excitonic peak E_{22} , which is in good agreement with the experimental data [32]. Compared with the previous

theoretical peak positions, the blue-shift of the peak in their results is about 0.5 eV. They showed that the screening effect on the diagonal ICIs (D-ICIs) plays a key role in this big blue-shift.

In resonant Raman processes, the optical selection rules are similar to those of optical absorption with the added considerations of the inclusion of the emission or absorption of a phonon of a given symmetry and the emission of the scattered photon. When the Raman spectra from an isolated SWNT is observed by changing the polarization of the light, usually there is no signal for light with a polarization perpendicular to the nanotube axis [29, 33]. Thus in the assignment of (n, m) values, the resonant condition for the light polarized parallel to the nanotube axis have only been considered. In fact, this assignment is sufficient for explaining most of the Raman spectra observed for isolated SWNTs. However, for SWNT bundles, all the RBM data observed within the Raman process occurring for parallel polarized light cannot be explained without considering resonance Raman process with perpendicular polarization [14, 30]. Because of the strong suppression of perpendicular transitions due to the depolarization effect, phonons excited via E_{ii} typically dominate Raman spectra of ensemble samples [21, 28, 29].

Experimentally this phenomenon was first observed via absorption measurements on assemblies of aligned nanotubes [30]. Rayleigh experiments at the single nanotube level have also confirmed the strong antenna effect in CNTs [28]. On the contrary, weak but distinct peaks have been observed in some photoluminescence experiments of individual single-walled nanotubes (SWNTs) under the perpendicular polarization and its peak position is shifted to the higher energy side [31, 32]. These features are described by advanced theory including excitonic effects [22-25]. The observation of weaker antenna effect is also reported when nanotubes are deposited on various substrates [24, 33]. These suggest that although the depolarization effect is known to play a major role, other factors might also be influential in the polarization dependence of the absorption spectra of nanotubes.

Yu *et al.* [28] obtained Rayleigh scattering spectra and Raman spectra from single bundles of aligned single-wall carbon nanotubes (SWNTs) with dark field optical microscopy and Raman microscopy. Rayleigh scattering spectrum reveals resonance peaks which are completely suppressed when the incident light polarization is

perpendicular to the nanotube axis. In case of polarized Raman measurements, Raman scattering signal was found to be much stronger for polarization of incident laser parallel to the tube axis than that polarized perpendicular to the tube axis with the intensity ratio varying from ~ 20 to more than 100.

Jorio *et al.* [29] studied the polarization dependence of the resonance Raman spectra for several different isolated SWNTs. They showed that a single isolated SWNT acts as a dipolar antenna, polarized along the tube axis, with the emission of Raman scattered light being strongly suppressed when the incident or scattered light is polarized perpendicular to the nanotube axis, in agreement with previous studies. For light polarized parallel to the tube axis, the strong resonance-effect breaks the symmetry-selection rules, and symmetry-forbidden modes appear in the Raman spectrum.

Islam *et al.* [30] presented the first experimental measurements of absolute linear absorption cross sections of single-wall carbon nanotubes for incident light polarized parallel and perpendicular to the nanotube axis. They demonstrated that perfectly aligned ensembles of nanotubes are not necessary to obtain absolute polarized absorbance cross sections. Instead, a combination of Raman scattering and linear optical absorbance can be used to extract the anisotropic optical absorbance spectra, even from samples that are weakly ordered. They found that parallel absorption cross section peaks at energies E_{nm} , while for the perpendicular polarization such diagonal transitions are forbidden and the absorption threshold occurs at E_{12} . Higher peaks in the perpendicular absorption are suppressed due to a vanishing matrix element. Their observations thus explicitly demonstrated the depolarization effect due to screening by induced charge.

Miyauchi *et al.* [31] performed anisotropic photoluminescence excitation (PLE) measurements on SWNTs in aqueous suspension for the UV-VIS-NIR range. They observed distinct absorption peaks of several isolated SWNTs for the polarization perpendicular to the SWNT axis, although the perpendicular excitation has been considered to be strongly suppressed due to the induced self-consistent local field depolarization effect. Using a procedure to determine the fractional contribution of parallel and perpendicular absorption and emission dipoles, they decomposed the PLE spectra into “pure” components for parallel and perpendicularly polarized excitations. The measured transition energies for perpendicular excitations were blueshifted from

$(E_{22}^S + E_{11}^S)/2$ which was the qualitative values predicted within a single-particle theory without considering excitonic effects.

Lefebvre *et al.* [32] reported polarized photoluminescence excitation spectra of twenty-five single-walled carbon nanotube species. Along with longitudinal excitations, several transverse excitations (polarization perpendicular to the SWNT axis) are identified with greatly reduced absorption intensity. Still, resonances not visible for the longitudinal case were present in the transverse spectrum. The transverse E_{12} transition is identified. In the simplest approximation, where electron-hole symmetry is assumed, two degenerate transitions E_{12} and E_{21} (E_{12} and E_{21} are not distinguished here) are expected halfway between E_{11} and E_{22} . In reality, carrier hopping between the two carbon sublattices produces a modest energy splitting. Experimental E_{12} values deviate from the simpler predictions $E_{12} = 0.5E_{22} + 0.5E_{11}$, and are closer to $0.8E_{22} + 0.2E_{11}$. Using $E_{12} = (1-x)E_{22} + xE_{11}$, they found that x ranges from 0 and 0.25. Thus, the transverse E_{12} transition is close to E_{22} , in line with the excitonic picture.

Blancon *et al.* [33] determined the spectrum and amplitude of the absorption cross-section of individual semiconducting single-wall carbon nanotubes using spatial modulation spectroscopy, over a broad optical spectral range (Fig. 2.3). Within the sensitivity limit

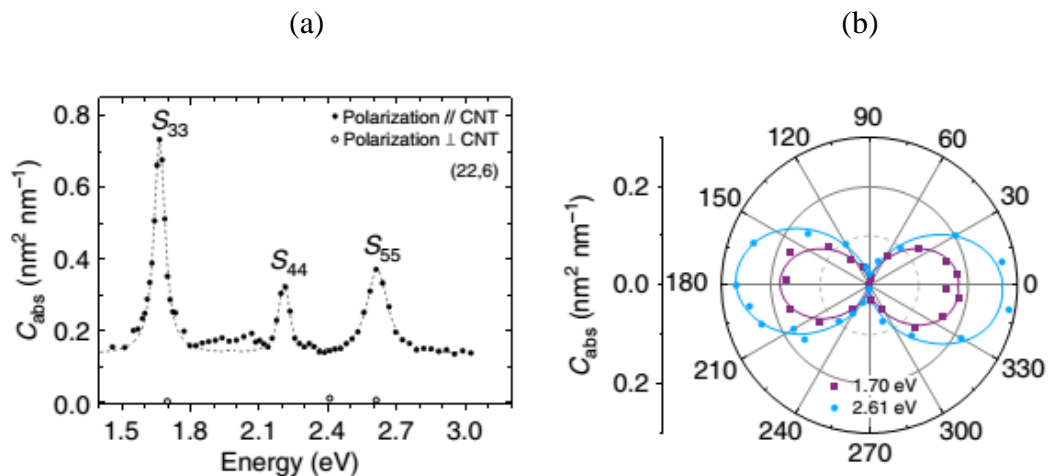


Figure 2.3: Absorption and Raman spectroscopy of a free-standing individual (22,6) semiconducting SWNT. (a) Absolute absorption cross-section spectrum for incident light parallel (full dots) and perpendicular (open dots) to the nanotube. (b) Light polarization-dependent absorption cross-section for two laser excitation energies [33].

of their experimental setup, no absorption was measured for incident light polarized perpendicular to the nanotube main axis (open dots in Fig. 2.3a). This is illustrated by plotting the absorption cross-section measured close to the resonances of lowest and highest energy as a function of the light polarization direction, relative to the CNT axis (Fig. 2.3b).

K Liu *et al.* [34] demonstrated high-sensitivity absorption spectroscopy for more than 50 individual chirality-defined SWCNTs over broad spectral range. They did not observe any resonances in the spectra for perpendicularly polarized light, when transitions between higher subbands are probed. From detailed theoretical analysis, they showed that although transitions between adjacent cutting lines are symmetry allowed, their matrix elements are always zero close to the band gap, except for the S_{12} and S_{21} transitions. This matrix element effect strongly suppresses exciton transition (as well as van Hove singularity at the band edge), resulting in no spectral resonances for higher-order transitions under perpendicularly polarized light (Fig. 2.4a).

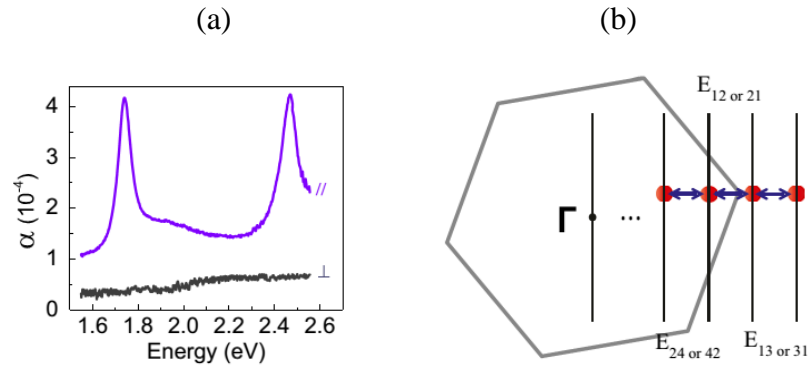


Figure 2.4: (a) Polarization-optimized homodyne detection of (24,24) single-walled carbon nanotube. The absolute optical absorption cross-section per carbon atom with both parallel (//) and perpendicular (\perp) light polarization to nanotube axis. (b) Cutting line scheme of optical transitions between subbands with angular momentum difference of $\pm Z$ in nanotubes [34].

They explained the suppression of higher-order perpendicular transitions as a direct consequence of the pseudospin of Dirac electrons in graphene [34]. As illustrated in (Fig. 2.4b), transitions between subbands with angular momentum difference of $\pm Z$ correspond to transitions between adjacent parallel lines in the graphene Brillouin zone in the zone-folding picture, and the electrical field direction is parallel to the momentum of band gap electrons (red dots in (Fig. 2.4b) in the graphene Brillouin zone. When the electrical field

and electron momentum are parallel to each other, the pseudospin of Dirac electron has to be conserved. For parallel lines at the same side of the K point, conduction and valence states have opposite pseudospin. Therefore, higher-order transitions associated with parallel lines at the same side of K point ((Fig. 2.4b), such as E_{13} and E_{24} , are forbidden. E_{12} and E_{21} transitions, however, are special because the two parallel lines are on the opposite side of the K point. In this case, valence electron in the first subband and conduction electron in the second subband have the same pseudospin, and the transitions are allowed. Indeed, prominent absorption peak corresponding to S_{12} and S_{21} transitions have been observed before by other research groups in semiconducting nanotubes with perpendicular polarization excitation [31, 32].

Barkelid *et al.* [37] performed polarization-dependent photocurrent spectroscopy on a single suspended semiconducting carbon nanotube p–n junction. The E_{11} and E_{22} optical transitions could be readily probed in parallel polarization and is suppressed for perpendicularly polarized light. An external quantum efficiency of 12.3% and 8.7% were measured for the E_{11} and E_{22} optical resonances, respectively, and this states a lower limit for the absorption coefficient for a single semiconducting carbon nanotube. By studying the polarization dependence of the photocurrent, a dielectric constant of 3.6 ± 0.2 was experimentally determined for this semiconducting carbon nanotube. Figure 2.5 displays the photocurrent spectra for light polarized parallel (black) and perpendicular (red) to the carbon nanotube axis. In Fig. 2.5 (a) and (b), clear peaks for the E_{11} and E_{22} transitions are visible at 0.85 eV and 1.36 eV, respectively, which were probed with parallel polarized light and suppressed for perpendicular polarization. The insets in Fig. 2.5 (a) and (b) show the angular dependence of the photocurrent for E_{11} and E_{22} as a function of the polarization angle of the incident laser light. A smaller polarizability of E_{22} was found compared to E_{11} , as a result of the smaller absorption cross section for the E_{22} transition, in agreement with previous calculations [30]. On a resonance the polarizability of the carbon nanotube is a result of both the depolarization effect and the optical selection rules. For light polarized perpendicular to the carbon nanotube axis, though the E_{12} / E_{21} transition was expected to show up on the low-energy side of the E_{22} resonance [32] but, this transition was considerably suppressed as a result of the depolarization effect and therefore not visible in their measurements.

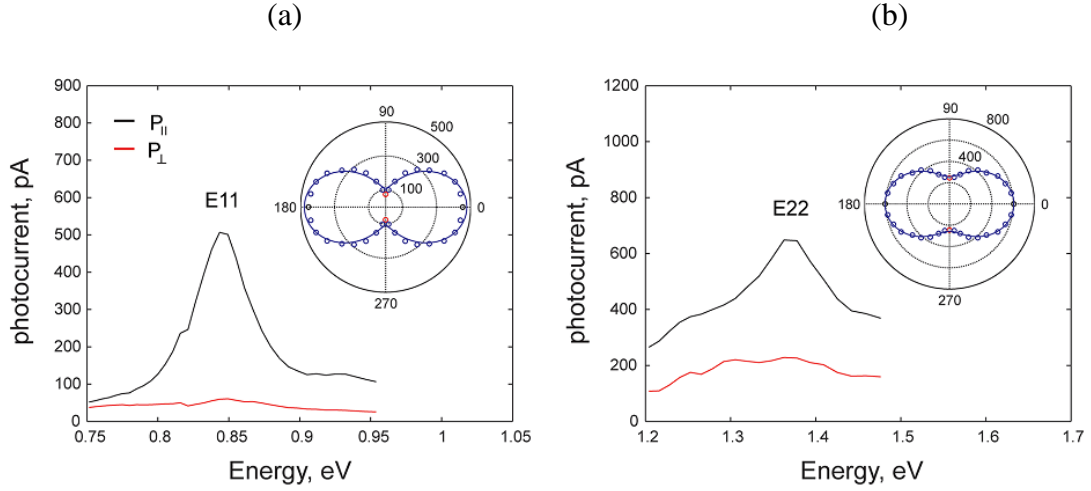


Figure 2.5: Polarized photocurrent spectroscopy on a p-n junction. Light polarized parallel (black) and perpendicular (red) to the carbon nanotube axis for (a) E_{11} transition and (b) E_{22} transitions. In both cases, for light polarized perpendicular to the carbon nanotube axis (red) suppresses optical transitions. Inset (a) and (b) angular dependence of the photocurrent (units: pA) on the polarization angle of the excitation light [37].

Based on all these reports on theoretical investigations and experimental measurements of optical transitions for polarization of incident light perpendicular to nanotube axis, the general conclusion is, perpendicular transitions are highly suppressed except in some cases mentioned above. Thus, in case of SWCNTs, subsequent focus will be on optical transitions due to polarization of incident light parallel to nanotube axis.

2.3 Optical Transitions in SWCNTs for Parallel Polarization

For polarization of incident light parallel to nanotube axis, each SWCNT (n, m) has a unique set of interband transition energies E_{ii} denoting the energy differences between the i -th conduction and valence bands and optical transitions can only occur between these mirror sub-bands [7, 8, 38-40], as shown in Fig. 2.6.

The tight-binding (TB) model of π -bands of graphene using the zone-folding approximation was initially used for modeling electronic band structure of single-wall carbon nanotube (SWCNT) due to its simplicity and low computational cost. In simplest TB model, for polarization of incident light parallel to the nanotube axis, the interband transition energy (E_{ii}) between the i -th pair of sub-bands of semiconducting (S) or metallic (M) SWCNTs is given by [41, 42],

$$E_{ii} = 2ia_{cc}\gamma_0 / d \quad . \quad (2.1)$$

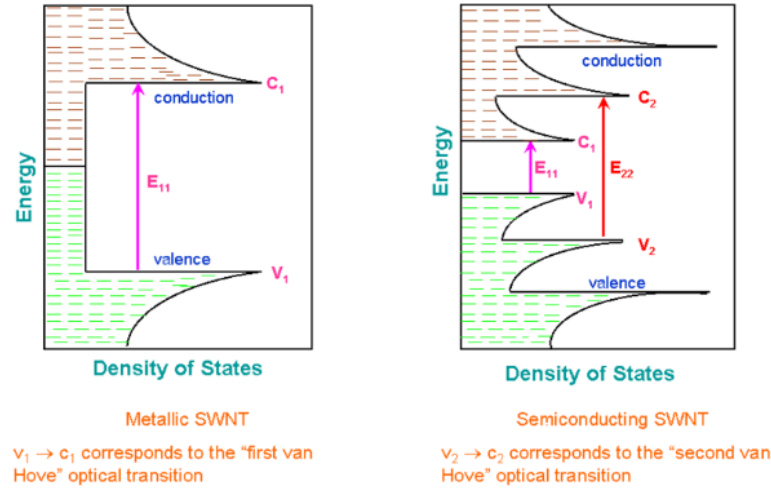


Figure 2.6: Schematic density of states diagram for a semiconducting single-walled carbon nanotube, in a simple band theory model [17].

Here, γ_0 is the nearest-neighbor hopping parameter, $a_{cc} = 1.42 \text{ \AA}$ is carbon-carbon bond length, d is nanotube diameter in nm, given by $d = \sqrt{3(n^2 + nm + m^2)}a_{cc} / \pi$ and j is an integer. E_{ii} corresponds to the first, second, third, fourth..... inter-band transitions (E_{11}^S , E_{22}^S , E_{33}^S , E_{44}^S) of semiconducting SWCNTs when $i = 1, 2, 4, 5...$ and to the first and second interband transitions (E_{11}^M , E_{22}^M) of metallic SWCNTs, when $i = 3$ and 6 , respectively. This inverse proportional trend of optical transitions of SWCNTs with its diameter was also observed from Kataura plot [43] and other optical spectroscopic experiments [44].

Equation (2.1) derived from simple TB model fails both qualitatively and quantitatively to predict various optical transitions [45]. It fails to reflect the experimentally observed fact that, for odd transitions (E_{11}^S , E_{33}^S ,) mod 1 type semiconducting SWCNTs have smaller transition energies than that of mod 2 type with comparable diameters whereas, for even transitions (E_{22}^S , E_{44}^S ,) the matter is reverse [44]. It also fails to account the experimentally observed ratio between different transitions, known as ‘ratio problem’ in literatures [46, 47].

Improved and extended tight binding models were proposed [40-42, 48-50] but, none of those models could completely describe all experimental observations [41, 44, 46, 47]. Consequently, empirical relation became necessary and useful attempts [45, 47, 51-53]

were made to devise model independent empirical equations mainly to predict first two optical transitions of semiconducting SWCNTs. However, calculation of optical transitions using those empirical relations were complicated and also limited in calculating only first two optical transitions. They overlooked the symmetry between different optical transitions and used random forms for different transitions.

Here, we will present a brief review of different computation models for calculating electronic band structure and optical transitions in nanotubes along with their limitations. Then, we will highlight the main factors that cause the existing models to calculate optical transitions that deviate from experimental results.

2.3.1 Experimental observations regarding optical transitions in SWCNTs

Sfeir *et al.* [44] observed from their Rayleigh scattering experiment that the mod 1 type semiconducting SWCNT have smaller transition energies than mod 2 type for odd transitions (E_{11}, E_{33}, \dots) whereas, mod 2 type semiconducting SWCNT have smaller transition energies than mod 1 type for even transitions (E_{22}, E_{44}, \dots) with comparable diameters. This observation is not reflected by Eqn (2.1) as it gives comparable values of transition energies for comparable diameters, irrespective of mod type. Okada *et al.* [54] also reported the relative difference between optical transition energies of mod 1 and mod 2 types. They studied the electronic structure of all the semiconducting SWCNTs having diameters between 0.75 nm and 1.55 nm. The Kataura plot calculated by them differed from the corresponding plot obtained from zone-folding model.

Besides, experimental observation showed a systematic pattern of optical transition energies in Kataura plot (E_{ii} vs d_t plot), depending on their mod $(n-m, 3) = 0, 1$ or 2 . As shown in Fig. 2.7, SWCNTs having same $(2n+m)$ values form branches in kataura plot, showing “family behavior” of transition energies [41, 55]. SWCNTs associated with each branch are termed as member of that $(2n+m)$ family [55]. This family behaviour cannot be explained by TB model predicted simple $E_{ii} \propto 1/d_t$ relation.

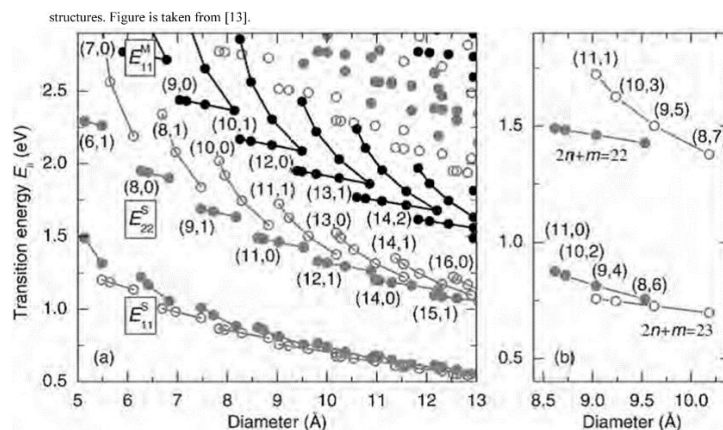


Figure 2.7: An illustration of Kataura plot. The gray symbols indicate mod 1 (closed circles) and mod 2 (open circles) semiconducting tubes. The lines connect $2n + m$ families [55].

Equation (2.1) also fails to account experimentally observed ratio of first two optical transition energies of semiconducting SWCNTs (E_{22}^S/E_{11}^S). Simple linearized tight-binding model predicted this ratio to be 2 from Eqn (2.1). Extended TB model later predicted that this ratio will be lesser than 2 at small diameters but will asymptotically approach 2 for large diameters [46]. In practice, experimentally observed ratio converges to only around 1.8 for large diameters [46, 56-59]. This problem is often referred as ‘ratio problem’ in literatures [46]. Neither the simple TB model nor the extended TB model could account this observation fully.

Bachilo *et al.* [47] and O’Connell *et al.* [60] independently performed fluorescence spectroscopy experiments and observed that absorption (E_{22}) and emission (E_{11}) energies from SWCNTs differ from theoretical predictions of tight binding calculations as shown in Fig. 2.8. Their measured optical transition frequencies (ν_{ii}) significantly deviate from simple diameter dependence. For example, they found ν_{22} value of the (9,2) tube is 26% higher (by 3700 cm^{-1} or 0.46 eV) than that of (9,1), even though its diameter is only 6% larger [47]. In addition, as tube diameter increases, they found the ν_{22}/ν_{11} (or, E_{22}/E_{11}) ratio apparently approaches a value around 1.75, smaller than tight binding prediction, i.e. the ‘ratio problem’. Their excitation vs emission frequency plot also showed a blue shift of these frequencies.

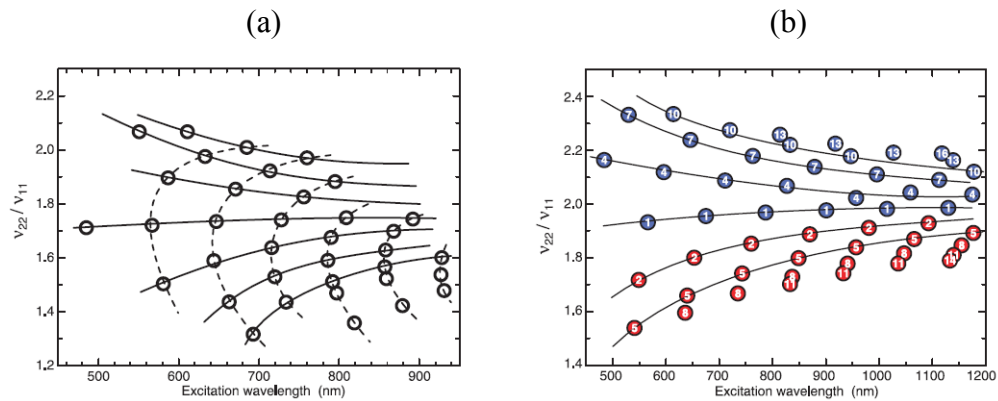


Figure 2.8: Comparison of fluorescence spectroscopy result with TB calculation. (a) Measured ratios of excitation to emission frequencies (b) Computed ratio from an extended TB model for mod 1 type (blue) and mod 2 type (red). Solid lines connect families with equal $n - m$ values and dotted line connects $2n+m$ families [47].

Kane *et al.* [46] and Mele *et al.* [56] reported ‘blue shift’ of transition energies which is also not reflected through Eqn (2.1) They observed this problem after scrutinizing fluorescence spectroscopy results reported by Bachilo *et al.* [47] and O’Connell *et al.* [60]. They plotted observed optical energies of SWCNTs measured in fluorescence spectroscopy as a function of $n/3R$ (Fig. 2.9) and showed that E_{11} and E_{22} deviate from

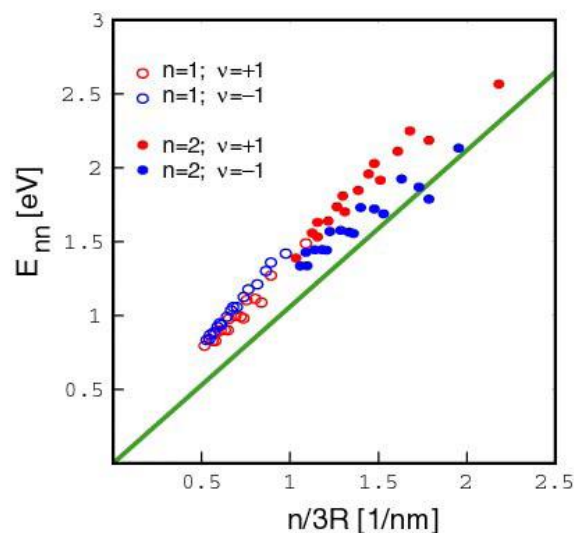


Figure 2.9: Observed ‘blue shift’ of optical transition energies measured from fluorescence spectroscopy, for mod 1 type ($v = +1$) and mod 2 type ($v = -1$) semiconducting SWCNTs. The solid line gives the prediction of linearized TB model theory [56].

simple linearized tight binding model and are blue shifted by a nonlinear $1/R$ scaling. They termed this observation as ‘blue shift problem’ [44, 56, 61]. Zhao *et al.* [59] discussed

both the ‘ratio problem’ and the ‘blue shift problem’. As per their analysis, the ratio problem is a simple consequence of nearly equal blue shifts of the two lowest optical absorptions (E_{11} and E_{22}) from TB frequencies.

2.3.2 Factors contributing variations of optical transitions in SWCNTs

Above experimental observations can be attributed to three main factors. First is nanotube’s ‘curvature’ induced band structure deviation from simple π -orbital graphene picture [8, 9, 49, 61]. Other two factors are ‘trigonal warping effect’ [9, 42, 44] and ‘chirality effect’ [50].

The first factor is the nanotube’s ‘curvature effect’ [8, 9, 48-50, 61] that causes deviations in the electronic properties of nanotubes derived from the simple π -orbital graphene picture. As SWCNTs are not just stripes of graphene but small cylinders, so, tube curvature forces the naturally flat sp^2 bonds to bend.

There are important consequences of this curvature on nanotube structure. Curvature causes hybridization between σ and π orbitals and charge self-consistency become important. The degree of hybridization becomes larger as the diameter of a SWCNT gets smaller. Also, due to curvature, C-C bonds perpendicular and parallel to the axis are slightly different and therefore the graphene basis vectors a_1 and a_2 are not of exactly equal length anymore. The σ - π hybridization effect has been considered and calculated in the literature [48-50, 62]. The main result is that nanotubes satisfying $|n-m| = 3k$ ($k=0, 1, 2, \dots$) develop a small curvature-induced bandgap, and hence become quasi-metallic or small gap semiconductor [62]. Armchair nanotubes are an exception because of their special symmetry, and only they remain truly metallic for all diameters [62]. On the other hand, some lowest diameter tubes with $|n-m| \neq 3I$ are found to be metallic due to high curvature in them. Zeng [8], Popov *et al.* [49], Okada *et al.* [54] and Gulseren *et al.* [61] studied the effects of nanotube curvature on electronic and optical properties of isolated single-walled carbon nanotubes and the calculated transition energies were found to deviate widely from π -band tight-binding model calculation, especially for small radius tubes [8]. Reported first principle calculations of SWCNTs of different chirality also confirmed this [63-67].

The second factor is the ‘trigonal warping effect’ [9, 44, 42, 54]. Reported deviations of TB model derived band structure and transition energies of nanotubes are not only due to the linearity of the graphene bands, but also due to their variation with directions in the Brillouin zone, termed as ‘trigonal warping’ [42]. This causes difference of transitions for mod 1 and mod 2 types. Though zone folding provides an explanation of this trigonal warping and consequent energy difference, but, it cannot fully account it. Zolyomi *et al.* [9] showed on the basis of their LDA calculation that trigonal warping effect found by their DFT calculation, is higher than that predicted by zone folding approach.

Saito *et al.* [42] investigated the ‘trigonal warping effect’ analytically to estimate the corresponding deviation in optical transitions of metallic and semiconducting SWCNTs. They showed that trigonal warping causes splitting of the density of State (DOS) peaks of metallic SWCNTs except for armchair tubes. Okada *et al.* [54] reported the relative difference between optical transition energies of mod 1 and mod 2 type based on their calculation, and attributed it to ‘trigonal warping effect’. Sfeir *et al.* [44] provided a firm experimental basis for ‘trigonal warping effect’ and family behavior as they observed these from their Rayleigh scattering experimental. They also discussed the cause of relative difference between optical transition energies of mod 1 and mod 2 type for even and odd transitions.

The third factor is ‘chirality effect’ [49,68] that originates from individual nanotube chirality and results unique features for each tube. Dependence of band structure and transition energies of nanotubes on their precise chiral structure is discussed theoretically and also observed from many experiments [45, 47, 62, 69-81].

Gulseren *et al.* [62], Ding *et al.* [50], Saito *et al.* [42], Maultzsch *et al.* [53], Yorikawa *et al.* [78, 79], and Jorio *et al.* [77] –all discussed relation of nanotube band gaps to chirality and proposed chirality dependent term to be included with Eqn. (2.1) to account this effect. It is noticed from Kataura plot that the upper and lower bounds of the widths of the optical transitions (E_{ii}) curves alternate with increasing i between the mod 1 and mod 2 zigzag semiconducting SWCNTs. Also, chirality changes from armchair to zigzag along $(2n+m)$ family lines [53]. Another family is observed in experimental E_{22}/E_{11} plot where nanotubes having same $(n-m)$ values fall along same symmetric lines or family branches [47]. These families are directly linked with their chiral index values. All these

clearly establish that band structure and transition energies of nanotubes shows unique features for different chiralities and indicate their dependency on chiral index (n, m) value of each tube.

2.3.3 Improved models for optical transition of SWCNTs

Improved models were proposed by authors within or beyond TB model framework. The model within TB model framework includes TB model for third nearest neighbors [48], symmetry-adapted non-orthogonal TB model [49] and TB sp^3s^* model (where 2s, 2p_x, 2p_y, 2p_z, and s* orbitals of each carbon atom are used as the basis set) [81]. Expanding the basic TB model expression of Eqn 2.1 for calculating optical transitions were also proposed.

Jorio *et al.* [77] presented the experimental Kataura plot where they plotted experimentally obtained optical transition energies for 200 SWCNTs as a function of tube diameter in a broad range of excitation laser energies (1.26–2.7 eV) and nanotube diameters (0.7–2.3 nm). They proposed following expression to interpret their results,

$$E_{ii} = \sum_l \alpha_l \left(\frac{p}{d_t} \right)^l + \beta_p \frac{\cos(3\theta)}{d_t^2}. \quad (2.2)$$

In the polynomial expansion on (p/d_t), *l* is a positive integer and terms up to *l* = 5 are needed for a good description of the observed E_{ii} , where, *p* = 1, 2, 3, 4 and 5 stands for E_{11}^S , E_{22}^S , E_{11}^M , E_{33}^S and E_{44}^S , respectively, α_l is determined by the linear dispersion relation of π -electrons in graphite in tight binding method and β_p measures the chiral angle dependence of optical transitions which is different for each E_{ii} subband, increasing for larger *i* due to the increase of the trigonal warping effect. These two parameters are measured empirically. The deviation of their result from experimental data goes up to 0.2 eV, which is not ignorable.

Weisman *et al.* [45] came up with a set of empirical equations to calculate first and second optical transitions in semiconducting SWCNTs. They fitted their spectrofluorimetric data for a large number of identified single-walled carbon nanotubes to following empirical expressions designed separately for mod 1 and mod 2 types,

$$E_{11}^S(\text{mod1}) = \frac{0.124 \times 10^4}{157.5 + 1066.9d_t} - 0.0956 \frac{\cos(3\theta)^{1.374}}{d_t^{2.272}}. \quad (2.3)$$

$$E_{11}^S(\text{mod2}) = \frac{0.124 \times 10^4}{157.5 + 1066.9d_t} + 0.043 \frac{\cos(3\theta)^{0.886}}{d_t^{2.129}}. \quad (2.4)$$

$$E_{22}^S(\text{mod1}) = \frac{0.124 \times 10^4}{145.6 + 575.7d_t} + 0.1644 \frac{\cos(3\theta)^{0.828}}{d_t^{1.809}}. \quad (2.5)$$

$$E_{22}^S(\text{mod2}) = \frac{0.124 \times 10^4}{145.6 + 575.7d_t} - 0.1762 \frac{\cos(3\theta)^{1.11}}{d_t^{2.497}}. \quad (2.6)$$

Liu *et al.* [39] studied the matter and demonstrated it extensively than anyone before. They carried a series of optical experiments and measured optical transition energies of numerous semiconducting and metallic SWCNTs. They proposed following empirical formula to fit their experimental values of different optical transitions of a number of semiconducting and metallic nanotubes,

$$E_p(k) = 2\hbar v_F(p) \times k + \beta \times k^2 + \eta(p) \times k^2 \cos(3\theta). \quad (2.7)$$

where, p is the transition index, k is the magnitude of wave vector in the graphene Brillouin zone that varies with nanotube chirality (n, m) and transition index p . Magnitude of k is given by $p \times 2/(3d)$, where d is the nanotube diameter. $E_p(k)$ is the effective dispersion for transition p , \hbar is the reduced Planck constant = 6.582×10^{-16} eV.s and $\beta = -0.173$ eV. nm². Rest two parameters v_F and η have different values for different transition index p . Thus, lot of parameters are involved in calculating any optical transition energy from the above equation.

2.3.4 First principle calculation of optical transitions

Failure of TB models or extended TB models leads to first principle (*ab initio*) calculation of electronic bandstructure and corresponding optical transition energies in SWCNTs. It was found that, while tight-binding calculations predict small diameter (4, 0) and (5, 0) zigzag nanotubes to be semiconducting with bandgaps exceeding 1 eV, *ab initio* calculation shows that they are metallic. Similarly, while tight binding calculations predict that the (6, 0) zigzag nanotube is quasi-metallic with a bandgap of approximately 200 meV, *ab initio* calculations indicate that they are truly metallic [63].

Zolyomi *et al.* [9] performed first-principles calculations of the electronic band structure of 40 different small diameter single-wall carbon nanotubes (9 armchairs, 17 zigzags, 14 chirals). They compared (Fig. 2.10) their calculated bandgaps to zone folding (ZF) tight binding (TB) values for all tubes. Significant differences were observed by them from what was expected from ZF-TB. Some of the ZF predicted semiconducting tubes proved to be metallic, due to σ - π mixing caused by high curvature, whereas eight of the ZF predicted metallic tubes (4 zigzags, 4 chirals) showed a small gap in the band structure.

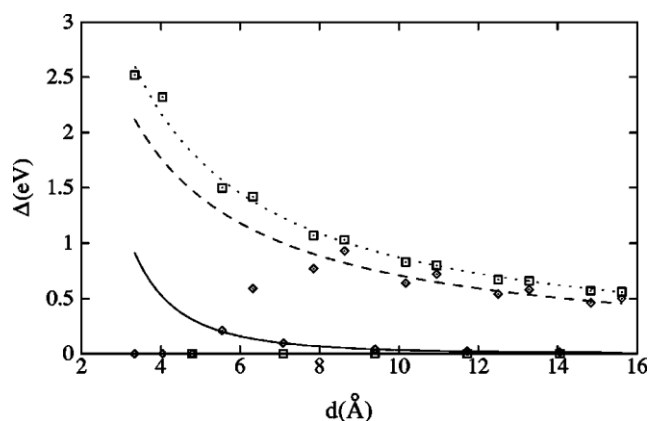


Figure 2.10: Band gaps of (4, 0) to (20, 0) zigzag tubes versus diameter. The squares show TB values, while the diamonds show DFT results [9].

Bertoni *et al.* [64] presented first principles calculations of the electronic structure of small carbon nanotubes with different chiral angles and different diameters ($d < 1$ nm). They compared the band structure and density of states (DOS) of chiral nanotubes with those of zigzag and armchair tubes with similar diameters. They evaluated the degree of hybridization occurs in these small diameters tubes due to higher curvature.

Machon *et al.* [65] and Yang *et al.* [66] performed first principle calculation using local density function approximation (LDA) to study their optical properties of lowest diameter 0.4 nm SWCNT that refers to (4, 2), (3,3) and (5, 0) tubes. Li *et al.* [67] also studied the structure of these tubes using transmission electron microscopy (TEM) and compared their observation with LDA calculations. LDA calculation of band structure of this smallest diameter tube showed that the chiral (4, 2) tube is a semiconductor with a small indirect band gap, armchair (3,3) is a metal, and zigzag (5, 0) is a metal, too, with a finite electronic density of state near the Fermi energy level [50]. Their conclusion that (5, 0) nanotube is metallic is in contrast to the prediction of the zone folding approximation

which considered this tube to be a mod 2 type semiconducting tube. They explained this feature as an effect of the strong curvature of the nanotube walls.

Recently, Niranjana *et al.* [82] performed theoretical study of electronic band gaps of semiconducting single-walled carbon nanotubes (SWNTs) with different sets of chiral indices using semi-empirical tight binding and density functional (DFT) based ab-initio methods. They performed the calculations for (n, m) chiral SWNTs, $(9, 0)$, $(12, 0)$ and $(15, 0)$ ‘metallic’ zigzag SWNTs, $(n, 0)$ zigzag SWNTs for $10 \leq n \leq 30$ and also pairs of SWNTs having same diameters but different chiral angles. From the comparison of bands gaps of tubes with same diameter, the electronic band gaps were found to vary with chiral angles with opposing trend as compared to that reported for experimental optical band gaps.

Tetik *et al.* [83] reported the structural and electronic properties of SWCNTs by using *ab initio* density functional theory. They considered zigzag $(6, 0)$, zigzag $(7, 0)$, chiral $(6, 2)$, chiral $(6, 3)$, and armchair $(7, 7)$ tubes. Zigzag $(6, 0)$ and armchair $(7, 7)$ tubes showed metallic behavior whereas, zigzag $(7, 0)$ and Chiral $(6, 2)$ tubes showed semiconducting behavior with band gap 0.5022 eV and 0.8291 eV, respectively (Fig. 2.11).

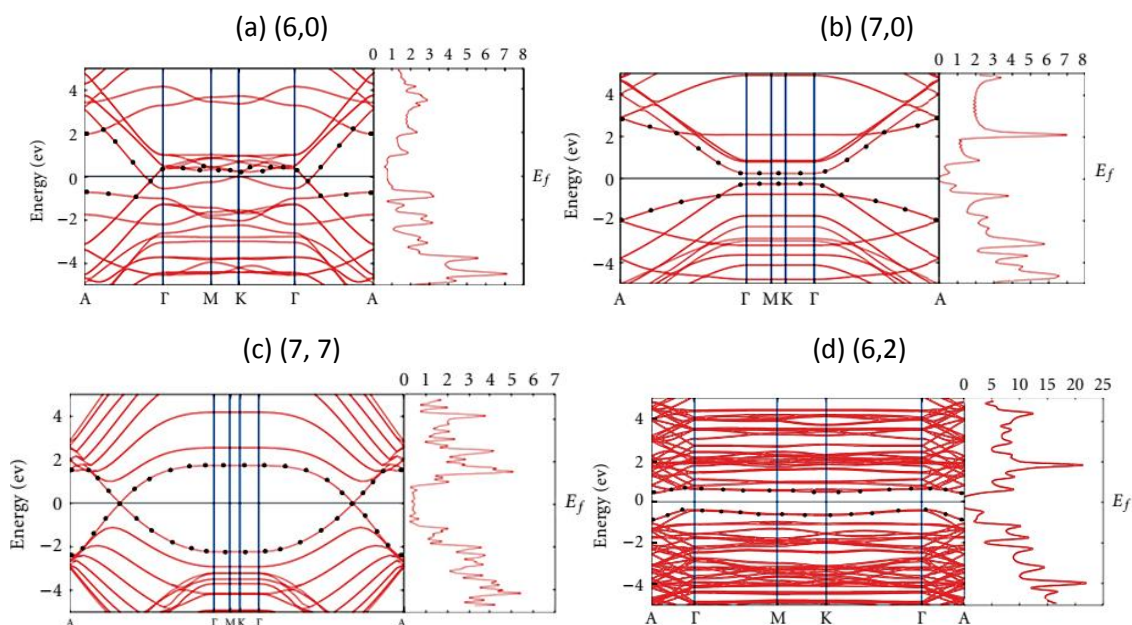


Figure 2.11: Electronic band structure and DOS of the Zigzag (a) $(6,0)$ (b) $(7,0)$, (c) armchair $(7,7)$ and (d) chiral $(6, 2)$ nanotubes [83].

They [83] also investigated the effect of rolling for nanotubes and observed that, for a (6, 3) chiral graphene, the band gap is 0.0516 eV but, when this graphene is transformed to a chiral (6, 3) nanotube, it showed quasimetallic chiral (6, 3) nanotube with band gap 0.0488 eV.

Umari *et al.* [84] found that the most common methods based on density functional theory (DFT) within local approximations for the exchange and correlation functional usually yield a significant underestimation of electronic gaps and cannot provide reliable estimations for CNTs. Within the many-body perturbation theory GW method, they calculated electronic band gaps for optically allowed transitions and investigated the dependence of electronic band gaps on tube diameter for (7,0), (8,0), (10,0), (11,0), (13,0) (14,0) and (16,0) semiconducting single-walled zigzag carbon nanotubes with diameters ranging from 0.56 nm to 1.27 nm (Fig. 2.12). Though their GW results were found to be in good agreement with previous estimates from optical measurements but, not only is

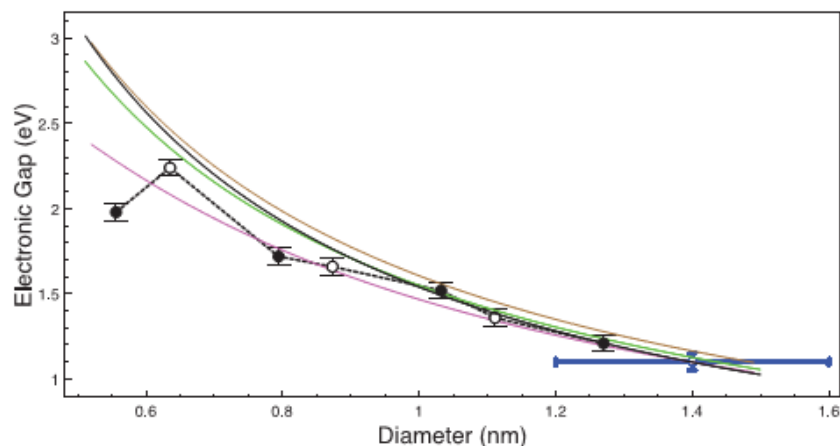


Figure 2.12: Electronic band gaps for semiconducting zigzag SWCNT, corresponding to optical transitions. Black discs and white circles are first-principles GW results for mod 1 and mod 2 zigzag CNTs, respectively, compared with theoretical estimates (green line) for generic tubes, for mod 1 (purple line) and mod 2 (brown line) zigzag tubes along with the experimental STS measurement (blue) [84].

the computational cost of GW approaches significantly higher than that of simpler DFT schemes but also particular care is required for obtaining converged results. Thus, GW method is not a realistic choice to be used in general.

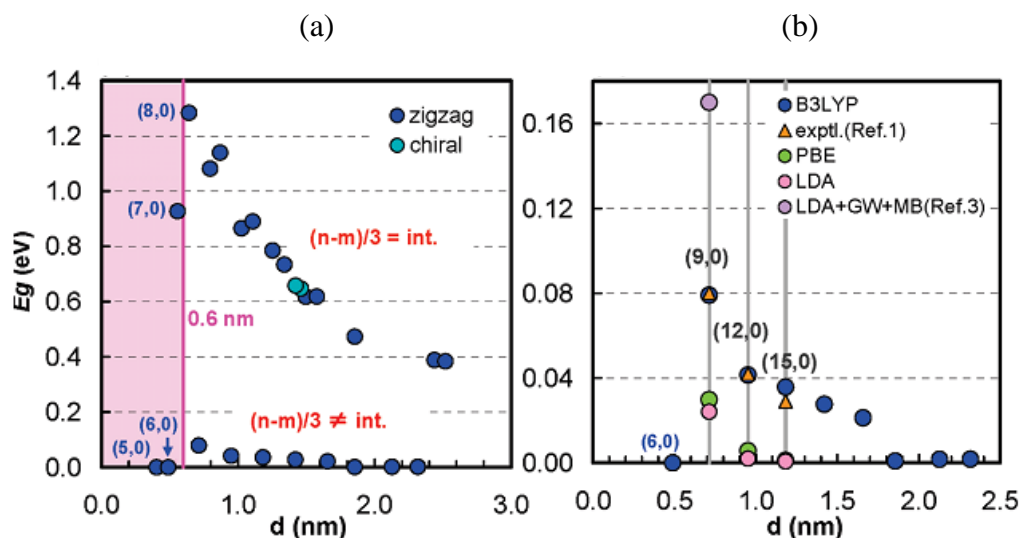


Figure 2.13: (a) Band gaps of zigzag SWNTs and (b) metallic zigzag (3m,0) SWNTs calculated by B3LYP (blue circles) as a function of diameter and compared with experimental, PBE, LDA and LDA+GW approximation + many-body effects [85].

Matsuda *et al.* [85] noticed that previous quantum mechanical (QM) calculations were not able to account for the observed band gaps. They reported ab initio quantum mechanical calculations of band structures of single-walled carbon nanotubes (SWNTs) using the B3LYP (Becke -Lee -Yang Parr) flavor of density functional theory (Fig. 2.13). They found that the (5,0) tube, expected to be a large gap semiconductor, is metallic. They also found that, for (7,0), (6,0), and (5,0) small zigzag CNTs, the π^* and σ^* states mix and repel each other, leading to lower pure π^* states and this $\sigma^* - \pi^*$ hybridization is not included in common tight-binding (TB) calculations so that TB fails to describe asymmetrical charge transfer of the atoms, leading to finite gaps for (5,0) and (6,0). Their results were in contrasts with the results from LDA, which lead to band gaps 70 -100% too small, and with those from the GW correction to LDA, which leads to a gap too large by 213%. They found that B3LYP leads to accurate values of the small band gaps observed in the metallic zigzag (9,0), (12,0), and (15,0) SWNTs, whereas previous calculations using LDA, PBE, PW91, GW, and TB do not.

Thus, in summary, the electronic structures and band gaps computed using TB model deviates significantly, both qualitatively and quantitatively, from the original band structures. Those computed within DFT framework and using local density (LDA) and generalized gradient (GGA) approximations for the exchange-correlation (xc) functional

are generally underestimated significantly. Also, there are few semi-empirical tight binding models with adjustable parameters which are fitted to first-principles calculations or experimental results. Improved estimates of band gaps of few selected SWCNTs have also been reported using GW approximation which usually provides band gap estimates with good accuracy, but, the method is hugely expensive computationally. Furthermore, care in calculations is required in order to obtain converged results. The band gaps of few SWCNTs computed using DFT framework and hybrid xc-functionals have also been reported. Like the GW scheme, the hybrid functional schemes are highly expensive computationally, although they usually provide reasonably accurate predictions of electronic structures.

Hence, it is required to develop an effective empirical model that counts the relations of chirality and structure of each SWCNT with its optical transitions which can be used to estimate optical transition energies of any SWCNT with high accuracy.

2.4 Optical Transitions in Double Wall Carbon Nanotubes

2.4.1 Introduction to the structure and properties of DWCNT

A DWCNT consists of exactly two concentric and weakly van der Waals coupled single-walled carbon nanotubes and an emerging class of carbon nanostructures [2, 10]. DWCNTs are the most ideal and fundamental systems to explore the mechanical and electronic couplings between concentric carbon layers. Although DWCNTs were discovered in 1991 and the first synthesis was reported in 1998, this structure has received relatively little attention until the synthesis [86, 87] and separation [88] of high purity samples. Compared to SWCNT, DWCNTs have higher mechanical strength and thermal stability and they also possess interesting electronic and optical properties [10, 11, 89-91].

A DWNT is uniquely characterized by the chiral indices (n_i, m_i) and (n_o, m_o) of the constituent inner and outer SWCNTs, respectively. Hereafter the structure of a DWCNT is identified as $(n_i, m_i)@(n_o, m_o)$, i.e. inner@outer wall. From the lattice symmetry point of view, the inner-tube and outer-tube can be either incommensurate or commensurate. A DWCNT is commensurate if the ratio between the unit cell lengths of the inner and outer-tubes is a rational number and incommensurate if the ratio is irrational [2, 10]. A

commensurate DWCNT has a periodical lattice structure while for incommensurate DWCNTs the symmetry is broken.

Earlier calculations [92] showed that the interwall distance between inner and outer tubes vary between 0.33 and 0.41 nm, with an ideal separation of 3.39 Å. Endo *et al.* [86] measured diameter distribution of highly purified DWCNTs using high-resolution TEM and found that they fall between 0.4 and 1.3 nm for inner tubes and 1.0 and 2.2 nm for outer tubes.

2.4.2 Electronic structure and optical transitions in DWCNTs

Because the inner and outer SWNTs can be either semiconducting (S) or metallic (M), DWNTs display four different configurations; S@S, S@M, M@S, and M@M —where the notation is inner@outer wall and each of them possess distinct electronic properties [90, 91]. All the properties of DWNTs are related to the individual nature of the layers and their interactions. A DWCNT must be considered as a new and separate nanostructure rather than the combination of two SWCNTs and hence, the electronic properties of DWCNTs are not a simple superposition of the electronic properties of inner and outer layer [10, 11, 90, 91]. Electronic properties of DWCNTs depend on the interwall distance as well as on the chirality and intrinsic properties of the constituent SWCNTs [10, 11, 89-91].

In DWNTs, the inner tube possesses a special status, granted by the outer tube, which acts as a shield and protects effectively the inner tubes from perturbations, thus provides higher mechanical, thermal, and chemical stability even in aggressive environments compared to SWNTs. Several experiments [93-100] performed on individual index-identified DWNTs demonstrated that the optical transitions of inner semiconducting tube (ISCT) of DWNTs can be significantly shifted compared to their SWNT constituent counterparts. Combining electron diffraction (ED) and Raman/optical spectroscopy to examine individual DWNTs appeared to be the most direct and unambiguous method to address the relationship between their structure and physical properties [96].

Shimamoto *et al.* [93] examined the optical features of single wall carbon nanotubes and the inner tubes within double walled carbon nanotubes having the same (n, m) chirality. They observed brighter and more stable photoluminescence signals as well as larger

absorbance and a redshift of both the E_{11} and E_{22} for the semiconducting inner tubes within DWNTs as compared to SWNTs. They opined that outer layers of DWNTs maintain the high structural integrity of the inner tubes during both oxidative purification and strong sonication steps and are responsible in increasing the dielectric screening due to weaker Coulomb interaction ; thus leading to a redshift of the excitonic transitions.

Liu *et al.* [94] showed experimentally that electronic coupling from van der Waals interactions can be surprisingly strong in incommensurate DWNTs. They performed combined electron diffraction and single-tube absorption measurements on 28 individual suspended DWNTs with a total of 99 optical transitions. In all studied DWNTs, they mapped each observed optical transition to that from an isolated constituent SWNT, but the resonance energy was always shifted for all optical transitions in DWNTs, varying from a red shift of 190 meV to a blueshift of 50 meV in different DWNT species. They also observed that the exact energy shift depends sensitively on the DWNT chirality. Even for the same inner tube, the energy shift of an optical transition varies significantly with the outer-wall tube species.

Tran *et al.* [95] reported optical absorption and resonant Raman scattering experiments on two individual free-standing DWNTs index identified by electron diffraction. The observed peaks of (16,12)@(27,10) (SC@SC) DWNT at 1.81, 2.15, and 2.71 eV are associated with optical transitions of the semiconducting inner tube, assigned to the S_{33} , S_{44} and S_{55} transitions, respectively.

Levshov *et al.* [96] reported direct and unambiguous evidence of the existence of inner semiconducting tube (ISCT) photoluminescence (PL) from measurements performed on individual freestanding index-identified double-walled carbon nanotubes (DWNTs). The DWNTs were characterized by high resolution transmission electron microscopy (HRTEM) and ED. On the basis of thorough Rayleigh scattering, Raman scattering, PL, and PL excitation (PLE) experiments, they were able to demonstrate that the PL of the ISCT of DWNTs is observed for both semiconducting and metallic outer tubes. They observed the shifts of the first optical transition energies compared to that of SWNTs. The first optical transition S_{i11} measured by them were found to be redshifted compared to the S_{11} of the corresponding SWNTs by an amplitude varying from -20 to -100 meV. These shifts were mainly attributed to the electronic coupling between the

incommensurate inner and outer tubes and to the effect of the interlayer dielectric screening of Coulomb interactions on the optical transitions in DWNTs. The magnitudes of the energy shifts depend sensitively on the specific optical transition and on the inner- and outer-tube species, which explains the tube-to-tube variations reported in their work.

Zhao *et al.* [97] experimentally combined Rayleigh scattering spectroscopy and electron beam diffraction on the same individual DWCNTs to probe the optical transitions of 30 structure-identified DWCNTs in the visible spectral range. Comparing with the transition energies in isolated single nanotubes in air, all the optical resonances observed in DWCNTs with weak coupling exhibit noticeable energy redshifts by a few tens to 200 meV.

Chalin *et al.* [98] reported that weak van der Waals coupling between the layers leads to a small shift of transition energies in optical spectra of double-walled carbon nanotubes (DWCNTs) with respect to their values in pristine single-walled nanotubes. They calculated the energy shifts for 94 optical transitions, and the maximum deviation lies within the range from -28 to 47 meV.

All structurally identified double-walled carbon nanotubes (DWCNTs) investigated so far are incommensurate. Commensurate DWNTs have never been observed experimentally because it is almost impossible to have two commensurate SWNTs with the radius difference matching the tube-tube separation in a DWNT [94,98]. Electronic structure calculations of incommensurate DWNTs are challenging because a finite unit cell does not exist [94]. Several theoretical attempts studying incommensurate DWNTs suggest that inter-tube electronic coupling is negligible between the incommensurate inner- and outer-wall carbon lattices because couplings at different carbon atom sites oscillate with random phases and cancel each other [94]. However, Liu *et al.* [94] showed experimentally that, contrary to previous theoretical predictions, electronic coupling from van der Waals interactions can be surprisingly strong in incommensurate DWNTs. It has been shown in previous studies of nanotubes in different environments that dielectric screening can lead to a redshift in optical transition energies, and the redshift value is similar for all optical transitions [94]. This dielectric screening effect can account for an average redshift of optical transition energies observed in DWNTs, but it cannot explain the very large and strongly transition-dependent variations in optical transition shifts,

especially the significant blueshifts for certain optical transitions. The residual deviation might be due to a dielectric screening-induced redshift different from the assumed constant shift (-55meV) and the uncertainty in experimental data ($\sim 20\text{meV}$) [94]. So far, there is no reliable theoretical or empirical models to calculate the electronic band structure of DWNTs or the energy shifts in inner semiconducting tube of DWNTs. The reason might be due to the fact that, SWCNTs have been studied extensively for last three decades, both theoretically and experimentally, whereas, serious study on DWCNT has started only in last decade and as a result, there are still ambiguities regarding its exact electronic structure for different combinations of inner and outer tubes. Thus, an empirical model to estimate the experimentally observed blueshifted optical transitions of inner semiconducting tubes in DWNTs would be useful.

2.5 Electronic Structure and Bandgaps in Graphene Nanoribbons (GNRs)

2.5.1 Structure and electronic properties of GNRs

Graphene nanoribbons (GNRs) have recently emerged as attractive organic materials for applications in new generations of electronic devices [3, 101-104]. Their greatly tunable properties as a function of their precise atomic structure are among the most appealing attributes that make GNRs so interesting. There are two types of ideal GNR, namely armchair GNRs (AGNRs) and zigzag GNRs (ZGNRs) depending on their armchair and ZGNR cross-section at the edges, respectively, both illustrated in Fig. 2.14. In addition, the GNRs are also labeled by the number of armchair or zigzag chains present in the width direction of the AGNR and ZGNR, respectively. If N_a be the number of armchair chains and N_z the number of zigzag chains, then the GNR can be conveniently denoted as N_a -AGNR and N_z -ZGNR, respectively [105, 106].

According to conventional notation, a GNR is specified by the number of dimer lines or zigzag chains along the ribbon forming the width, for the AGNR and ZGNR, respectively, as explained in Fig. 2.14. For example, the structure of Fig. 2.14(a) is referred as a 11-AGNR and the structure in Fig. 2.14(b) as a 6-ZGNR. In addition, when referring to the width of a GNR here, the width is defined without including the hydrogen atoms at the edge, as shown in Fig. 2.14.

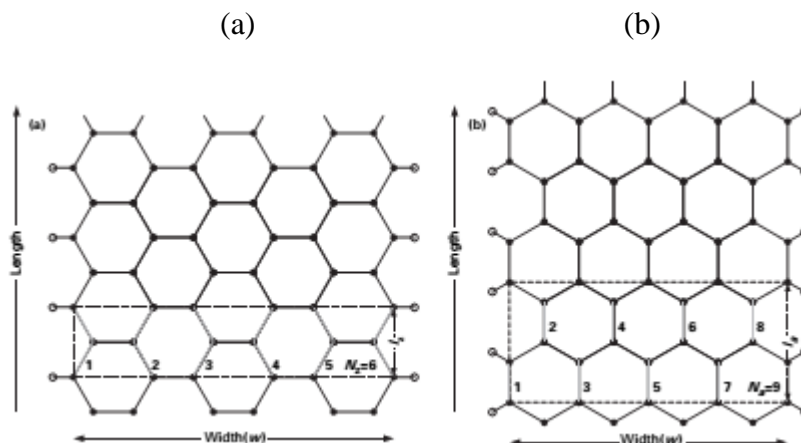


Figure 2.14: The finite-width honeycomb structure of GNRs. The lattice of a (a) 6-ZGNR and (b) 9-AGNR. The dashed box represents the primitive unit cell. The open circles at the edges denote passivation atoms such as hydrogen. The bold gray lines are the zigzag or armchair chains that are used to determine N_z or N_a respectively [3].

Among GNRs, the armchair GNRs are believed to be the most promising candidates towards the design of graphene based circuits due to their highly tunable electronic properties [25, 107], making them an interesting material for room-temperature electronic and optoelectronic switching devices. For example, Tayo *et al.* [107] reported GNR heterojunction of 7-AGNR and 11-AGNR, having individual bandgap of 1.54 eV and 0.16 eV, respectively. They showed that, by increasing the length of the 11-AGNR, band gap of the 7-11 GNR heterojunction can be tuned continuously between the band gap of the 7-AGNR (1.54 eV) and the band gap of the 11-AGNR (0.16 eV).

First principle calculations reveal that AGNRs can be classified into three different subfamilies depending on $N_a = 3p$, $3p + 1$ or $3p+2$, where p is a positive integer, their band gaps being inversely proportional to the ribbon width within each of those families [106]. The reported band gap values of the various AGNRs synthesized to date confirm this picture for each of the GNR families. This result is clearly indicative of width-dependence physics in the armchair GNRs.

Earlier theoretical studies, mainly based on simple tight-binding (TB) approximations, predicted that GNRs can be either metallic or semiconducting depending on GNR types [108]. As per TB calculations, armchair-edged N_a -AGNR is metallic if $N_a = 3p+2$, otherwise, it is semiconducting. However, simple TB model calculation of bandgaps of GNRs was found to be incorrect. Subsequent theoretical models [108–114] and

experimental works [105-107, 115-122] showed that quantum confinement and edge effects introduce a band gap in all narrow GNRs and there are no metallic nanoribbons.

Wang *et al.* [106] measured energy gaps of atomically precise armchair graphene sidewall nanoribbons with widths ranging from $N_a = 6$ to $N_a = 26$. All the armchair GNRs exhibited semiconducting gaps due to quantum confinement and the GNRs were well grouped into three categories according to their electronic structures. The origin of the energy gaps for GNRs with armchair edges is the quantum confinement. Their result indicated that the electronic structures of the armchair GNRs can be tuned dramatically by simply adding or cutting one dimer line along the ribbon width. However, the lack of exact number of carbon dimer lines N_a across the width of these GNRs, owing to the measurement error and the atomic-scale edge irregularities, did not allow a more systematic insight.

2.5.2 Earlier models for calculating bandgaps in armchair GNRs

The studied armchair GNRs with atomically well-defined widths and edge orientation are limited up to now [116, 121, 122]. STM study of armchair GNRs with widths ranging from about 3.5 ± 0.5 nm to 10.5 ± 0.5 nm revealed that these GNRs can be grouped into two families; one displays large gaps, which is attributed to the ribbons belonging to $N_a = 3p$ and $N_a = 3p + 1$ classes; the other exhibits no detectable gap, which is attributed to the ribbons belonging to the $N_a = 3p + 2$ class [106]. An example is the observation of about 100-meV bandgap in a $N_a = 5$ armchair GNR (the length of the studied GNR is about 5 nm), which indicates that the $N_a = 3p + 2$ (here $p = 1$) armchair GNR should exhibit a very small bandgap [106, 121]. Another example is, with $p = 5$, the armchair GNRs with $N_a = 15(N_a = 3p)$ and $N_a = 16(N_a = 3p + 1)$ display energy gaps $E_g = 0.556$ eV and $E_g = 0.657$ eV, respectively, whereas the armchair GNR with $N_a = 17(N_a = 3p + 2)$ is predicted to exhibit a much smaller gap $E_g = 0.118$ eV [106]. Therefore, in subsequent sections, focus will be on calculation of bandgaps of AGNRs for $N_a = 3p$ and $N_a = 3p + 1$ classes only.

Son *et al.* [108] showed that GNRs with hydrogen passivated AGNR always have nonzero and direct band gaps. Their LDA calculations showed that the N_a -AGNRs are semiconductors with energy gaps which decrease as a function of increasing ribbon

widths (w_a). The gaps as a function of ribbon width are well separated into three different subfamilies and the gap size hierarchy is $3_{p+1} > 3_p > 3_{p+2} \neq 0$. They derived following relations by modifying TB model approximation using their ab-initio calculation,

$$E_g (eV) = t[4\text{Cos}\frac{p\pi}{3p+1} - 2] - \frac{8\delta t}{3p+1} \text{Sin}^2 \frac{(p+1)\pi}{3p+2}, \text{ (for } N_a = 3p) \quad (2.8)$$

$$= t[2 - 4\text{Cos}\frac{(p+1)\pi}{3p+2}] - \frac{8\delta t}{3p+2} \text{Sin}^2 \frac{p\pi}{3p+1}. \text{ (for } N_a = 3p+1) \quad (2.9)$$

Where, $t=2.7$ and $\delta=0.12$

Wakabayashi *et al.* [109] presented simple derivations of the energy spectrum and wave functions for GNRs using the nearest-neighbour tight-binding model and a wave mechanics approach that resulted following expressions for bandgaps in AGNRs,

$$E_g (eV) = 2t[1 + \text{Cos}\frac{3p\pi}{3p+1}], \text{ (for } N_a = 3p) \quad (2.10)$$

$$= 2t[1 + \text{Cos}\frac{(3p+1)\pi}{3p+2}]. \text{ (for } N_a = 3p+1) \quad (2.11)$$

After Taylor expansion under the condition of $1/W < 1$, the above expressions can be further simplified as,

$$E_g (eV) = \frac{\pi}{w + 0.866}, \text{ (for } N_a = 3p) \quad (2.12)$$

$$= \frac{\pi}{w}. \text{ (for } N_a = 3p+1) \quad (2.13)$$

Yang *et al.* [110] carried out a first-principles calculation using the GW approximation to determine the quasiparticle energy spectrum and the band gaps of the GNRs. They found that, because of the quasi-one-dimensional nature of a GNR, electron-electron interaction effects due to the enhanced screened Coulomb interaction and confinement geometry greatly influence the quasiparticle band gap. Compared with previous tight-binding and density functional theory studies, their calculated quasi-particle band gaps showed significant self-energy corrections for AGNRs, in the range of 0.5–3.0 eV for

ribbons of width 2.4–0.4 nm. They derived following equation to fit the quasi-particle bandgaps from their GW calculation,

$$E_g (eV) = \frac{3.13}{w + 0.53}, \text{ (for } N_a = 3p) \quad (2.14)$$

$$= \frac{4.44}{w + 0.42}. \text{ (for } N_a = 3p+1) \quad (2.15)$$

Pandya *et al.* [111] deduced a relation to predict band gap of GNRs. They deduced following relation using expression of Fermi velocity to calculate the energy band gap of GNRs,

$$E_g (eV) = \frac{3.036}{w}. \text{ (for any type of a-GNR)} \quad (2.16)$$

Han *et al.* [112] presented electronic transport measurements of lithographically patterned GNR structures where the lateral confinement of charge carriers creates an energy gap. They measured more than two dozen GNRs of different widths and crystallographic orientations. They found that the energy gap depends strongly on the width of the channel for GNRs in the same crystallographic direction. They fitted their band gaps with following relation,

$$E_g (eV) = \frac{\alpha}{w - w^*}, \quad (2.17)$$

where $\alpha = 0.2$ to 1.5 and $w^* = 16$ nm.

H. Raza *et al.* [113] reported electronic structure and electric-field modulation calculations in the width direction for armchair graphene nanoribbons AGNRs using a semiempirical extended Hückel theory. They found that, for each type of AGNR, band gaps are inversely proportional to the width with a different proportionality constant. Their band gap versus width w relations are given as,

$$E_g (eV) = \frac{.86}{w}, \text{ (for } N_a = 3p) \quad (2.18)$$

$$= \frac{1.04}{w}, \text{ (for } N_a = 3p+1) \quad (2.19)$$

2.5.3 Limitations of the earlier models for bandgaps of GNRs

Although the aforementioned models and equations described the low energy properties of graphene very well, a careful consideration of edge effects in nanometer sized ribbons are required to determine their band gaps because, unlike the situation in graphene, the bonding characteristics between atoms change abruptly at the edges. One of the major limitations of each of the above equations for calculating bandgaps of AGNRs is, none of them predicts measured bandgaps of different AGNRs reported from various experiments [105-107, 115-122] with good accuracy. Some of these equations highly underestimates [107, 108, 111, 112] the experimental bandgaps while others overestimates [109, 110, 113] them significantly.

Owing to the challenges involved in the fabrication of atomically precise GNRs, only very limited experimental data on atomically well-defined structures are presently available. Available experimental data of bandgaps of AGNR is summarized below.

It was noted that the GW quasiparticle band gaps calculated for isolated AGNRs [110] are significantly larger compared to the experimentally measured band gaps, where the AGNRs are supported on a Au (111) surface or on a NaCl (001) monolayer which is itself on top of a Au (111) surface [116, 122]. This overestimation is attributed to the lowering of Coulomb interaction in AGNRs by the screening from the underlying substrate [114]. For example, if we consider $N = 7$ AGNR (corresponds to a width of about 0.74 nm), a gap of 3.8 eV has been calculated by the GW method [110] compared to 1.5–1.6 eV obtained by DFT [108, 110] whereas, measured gaps are 2.3–2.8 eV [116]. Thus, calculated bandgaps from above equations need to be treated as estimates rather than accurate predictions, and those obtained by DFT calculations as a lower limit.

Díez *et al.* [105] performed the synthesis of the first 5 members of 3p-AGNR family, namely 3-, 6-, 9-, 12-, and 15-AGNRs on the same Au (111) surface and found the bandgaps by means of STS to be 3.23 eV, 1.69 eV, 1.35 eV, 1.13 eV and 1.04 eV,

respectively. A continuously decreasing band gap was observed as the GNRs structures get wider.

Söde *et al.* [115] found $E_g = 2.37 \pm 0.06$ eV for the 7-AGNR on Au(111) by scanning tunneling spectroscopy. Angle-resolved photoelectron spectroscopy and scanning tunneling spectroscopy data from armchair graphene nanoribbons of width $N = 7$ supported on Au(111) reveal a band gap of 2.3 eV. An electronic band gap of $\Delta = 2.3 \pm 0.1$ eV is derived for the 7-AGNRs supported on a gold substrate [116].

Talirz *et al.* [118] estimated the (fundamental) band gap of the 9-AGNRs while adsorbed on Au(111). They combined the quasiparticle corrections computed for the freestanding 9-AGNR at the G_0W_0 level with a classical image charge (IC) model that takes both the adsorption distance of 9-AGNRs on Au(111) and their intrinsic polarizability into account. This method yields $\Delta_{GW} + \Delta_{IC} = 2.1$ eV $-$ 1.0 eV = 1.1 eV, in acceptable agreement with the experimental value of 1.4 eV considering the approximations involved, (one-shot GW with plasmon pole model, classical image charge model for the substrate).

Deniz *et al.* [119] revealed the electronic structure of substrate supported AGNRs by Scanning Tunneling Spectroscopy and found bandgaps of 2.7 eV, 1.5 eV, 0.2 eV, 0.9 eV, 0.7 eV of 7-, 9-, 14-, 18- and 21-AGNRs, respectively.

Yamaguchi *et al.* [120] made the first demonstration of the synthesis of GNRs having a bandgap smaller than 1 eV in a controlled manner. They revealed that the 17-AGNRs have a bandgap of 0.19 eV on Au(111), which is consistent with a theoretically obtained bandgap of 0.63 eV for a freestanding 17-AGNR. For 13-AGNRs on Au (111), the energy gap is estimated to be $\Delta_{STS} = 1.34 \pm 0.03$ eV from the energy difference between those peaks. This energy gap is also consistent with the previous one (1.4 ± 0.1 eV). With the GW calculations, the quasiparticle gap is predicted to be $\Delta_{GW} = 2.25$ eV for a freestanding 13-AGNR, and the renormalized gap of the 13-AGNR supported by the Au(111) substrate is corrected as $\Delta_{GW}' = 1.29$ eV using the advanced image-charge model. The corrected theoretical gap shows good agreement with their experimental findings.

Chen *et al.* [122] conducted STS to find the band gap for 13-AGNRs featuring atomically smooth hydrogen-terminated armchair edges and 13 carbon dimer lines across their width. STS reveals the An average band gap for 13-AGNRs on Au(111) of 1.4 ± 0.1 eV. Narrower 7-AGNRs, by comparison, have an energy gap of $\Delta \approx 2.6$ eV using similar measurement criteria.

All experimental bandgap values of different AGNRs, as reported above, are different from the predicted or calculated bandgap values from various theoretical models and corresponding equations.

2.5.4 Improved models

Kharche *et al.* [114] developed an integrated *first-principles* approach to calculate the quasiparticle energies of GNRs weakly interacting with the underlying substrate. In their approach, the energy levels of the substrate-supported GNRs are determined by correcting the GW quasiparticle energies of isolated GNRs with the energy shifts arising from screening of quasiparticle excitations by the substrate. The energy shifts were determined using an image-charge model.

Ruffieux *et al.* [116] showed that, when the AGNR is absorbed on a metal surface, its bandgap is reduced as an effect of the substrate polarization, which they estimated by including image charge (IC) corrections on top of GW calculations for the isolated GNR. Earlier, it was shown by state-of-the-art many-body perturbation theory (GW) calculations [110] that electron electron (e-e) interactions play a dominant role in GNRs due to their quasi-1D nature and the weak screening. These effects give rise to an energy gap as large as 3.7 eV for the isolated 7 AGNR, significantly larger than the one predicted by single particle (e.g., tight binding or DFT) approaches [108, 110]. GW correction brings the LDA gap of the isolated AGNR from 1.6 to 3.7 ± 0.1 eV. The IC correction that mimics the presence of the metallic substrate reduces the energy gap by 1.0 to 1.4 eV. Overall, this results in an energy band gap of 2.3 to 2.7 eV for the 7-AGNR on Au(111), which is in very good agreement with the experimental value of 2.3 ± 0.1 eV.

Linden *et al.* [117] derived band gap $E_g = 2.8 \pm 0.4$ and $E_g = 1.6 \pm 0.4$, respectively, for straight 7-AGNRs and 13-AGNRs. Quasiparticle corrections in the GW approximation [110] increase the gap energy significantly to 3.8 eV for 7-AGNR and 2.3 eV for 13-

AGNRs. A subsequent consideration of the electron-hole interaction by solving the Bethe-Salpeter equation leads further to excitonic states with binding energies of 1.8 eV with respect to the lowest unoccupied molecular orbital, thus reducing the optical gap considerably [117].

From the above review of earlier models for bandgaps of GNRs, it is clear that existing models have limitations in estimating experimentally measured bandgaps of GNRs. Proposed improvement by image charge (IC) corrections on top of GW calculations gives reliable prediction but it is computationally intensive and challenging to converge numerically. Therefore, a simple and empirical relation would be useful for estimating the bandgaps of AGNRs with high accuracy.

2.6 Utility of Knowing Optical Transitions in SWCNTs and Bandgaps in GNRs

2.6.1 Characterizing SWCNTs and DWCNTs from higher optical transitions

Characterizing SWCNTs requires accurate information about their optical transitions and in many cases there is no option for characterizing SWCNTs except by using their higher transitions [123-143]. For example, Rayleigh spectra over a photon energy range 1.2–2.7 eV is sensitive to the 2nd transition of metallic tubes and 3rd and 4th transitions of semiconducting tubes. For small diameter nanotubes, the 1st metallic transition may be observed, while the E_{55} transition may appear below 2.7 eV for semiconducting SWCNTs with $d > 2.5$ nm.

Semiconducting and metallic SWCNTs and DWCNTs have been characterized using their higher optical transitions $E_{22}(M)$, $E_{33}(S)$, $E_{44}(S)$ and $E_{55}(S)$. Fig. 2.15 (a) to (e) presents the experimentally measured Rayleigh and Raman spectra of some single wall and double wall CNTs [132, 133, 137]. They assigned the observed emission peaks to higher transitions of possible CNTs.

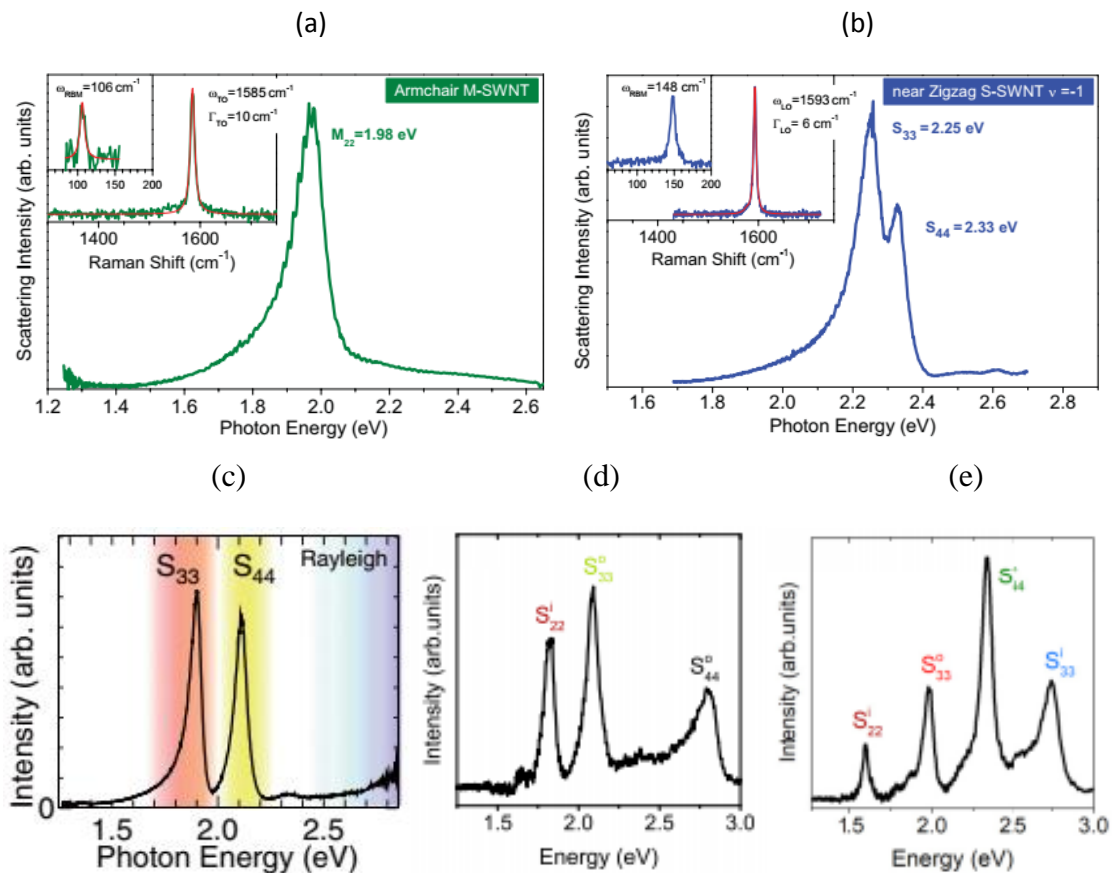


Fig 2.15: Rayleigh and Raman spectra of (a) an armchair M-SWNT assigned to (19,19) or (20,20) (b) a near zigzag semiconducting SWNT assigned to (20,3) or (21,1) [132]. Rayleigh spectra of (c) a single undoped nanotube assigned to (26,0) or (25,2) [133] (d) (7,6)@(16,6) DWCNT and (e) (10, 6)@(14, 13) DWCNT [137].

2.6.2 Describing emission spectra of CNT based LEDs

Information on optical transitions help describing experimental reports on emission spectra measured from SWCNT based LEDs. Wang *et al.* [144] carried out electroluminescence (EL) measurements on a two-terminal carbon nanotube (CNT) based light-emitting diode (LED), composed of a semiconducting SWCNT which is asymmetrically contacted on the one terminal by Sc and on the other terminal by Pd (Fig. 2.16). Earlier studies have shown that Sc can make a perfect Ohmic contact with the

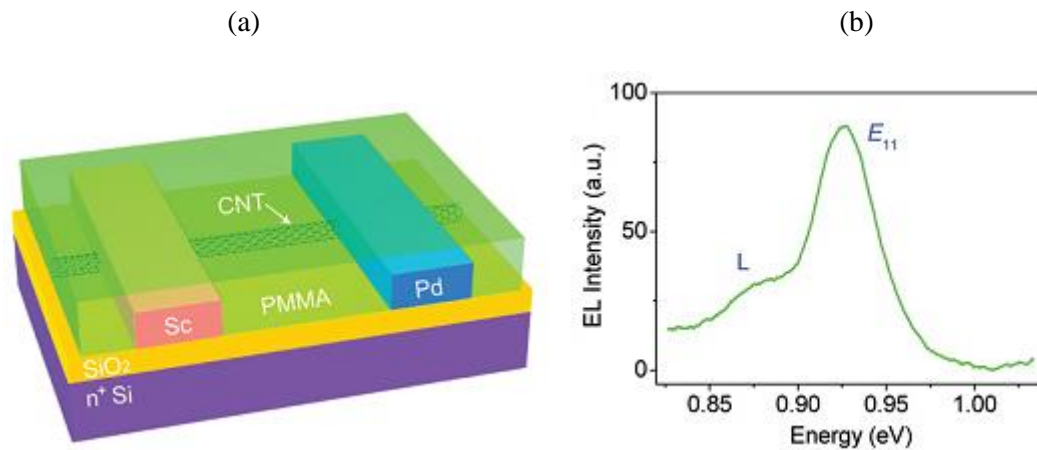


Figure 2.16: Structure and characteristics of a CNT light-emitting diode. (a) Schematic diagram illustrating the structure of an asymmetrically contacted CNT device. (b) EL spectrum of the diode when operated at large forward bias [144].

conduction band of the CNT while Pd makes perfect Ohmic contact with the valence band of the CNT. Thus it was a contact doped p–n junction, and the current-voltage (I - V) characteristic measured from the device behaved as a diode. At large forward bias, with the Sc contact being grounded, the injected electrons and holes recombine radiatively in the SWCNT channel yielding a narrowly peaked emission peak. They determined the diameter of the CNT to be 1.14 nm and observed EL spectrum with clear emission peak at 0.925 eV which was identified as that resulting from the excitonic state of a (12, 4) SWCNT.

Mueller *et al.* [145] used well-characterized CVD growth method that delivers spatially separated single-walled carbon nanotubes and observed a single, semiconducting single-walled carbon nanotube, as confirmed independently by AFM, electrical transport, and electroluminescence measurements. From electroluminescence measurements of their p–n diode in the ambipolar regime, they obtained the maximum of the spectral intensity distribution at $E_{11} \sim 0.635$ eV. They also presented the results obtained from the same device with different SWCNT where the dominant emission was found to be 0.755 eV. From resonance Raman spectroscopy and atomic force microscopy (AFM), the nanotube diameter was determined to be 1.41 nm and 1.24 nm, respectively in devices with two different SWCNTs (Fig. 2.17).

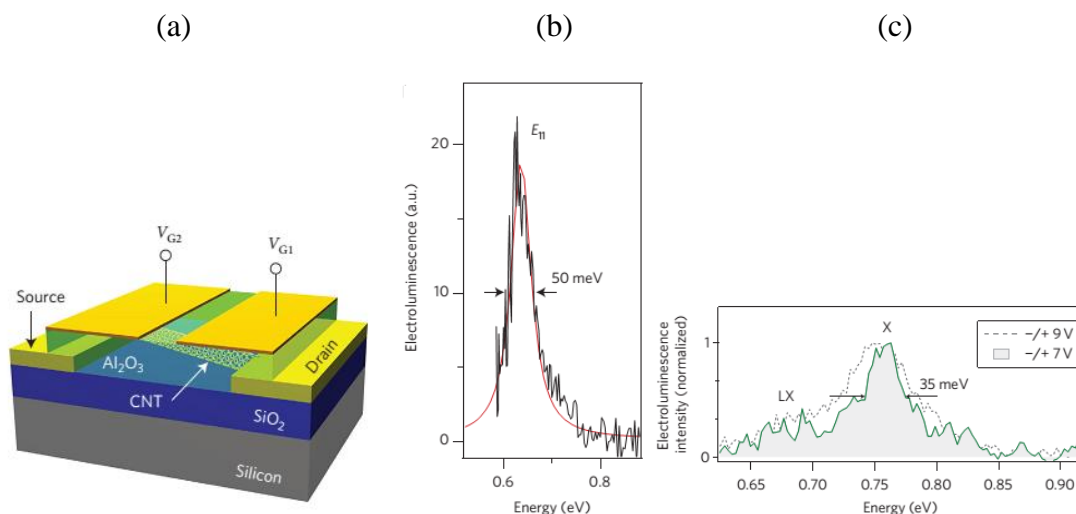


Figure 2.17: Device structure and electronic characteristics. (a) Schematic of the carbon nanotube LED. (b) Electroluminescence spectrum of a nanotube diode at the device. (c) Comparison between electroluminescence spectra at two different gate biases (normalized) for the same device with different SWCNT [145].

Yu *et al.* [146] reported the fabrication and performance characteristics of light-emitting devices that use serpentine CNTs, having multiple parallel CNT channels of identical chirality, grown directly on quartz (Fig. 2.18). This represents the ideal structure for scaling up the power of the CNT LEDs, which are free of the usual negative effects that are due to the complicated interactions between CNTs of different diameters and

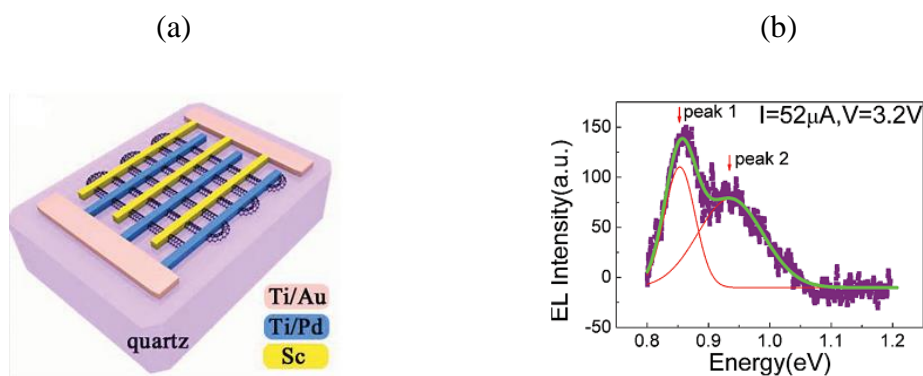


Figure 2.18: Structure and operation principle of CNT LED arrays. (a) SEM image showing serpentine-CNT-based diode arrays on quartz. (b) EL spectrum obtained from the CNT-diode-array device. This spectrum can be fitted by using two Gaussian functions (red lines) that peak at 0.85 and 0.94 eV. The lower peak corresponds to E_{11} of the SWCNT [146].

chiralities. The semiconducting CNTs were asymmetrically contacted by Sc and Pd contacts that acts effectively as a p-n junction with high carrier-injection efficiency and low operating voltage. Two emission peaks were identified from their CNT-based LED

where the lower energy emission peak was at 0.85 eV. From atomic force microscopy (AFM), the diameter of the nanotube was estimated to be 1.1 ± 0.2 nm. The emission peak was identified as the E_{11} excitonic transition of the CNT.

Pfeiffer *et al.* [147] measured the electroluminescence and photoluminescence of (9, 7)-semi-conducting carbon nanotube devices (Fig. 2.19) and demonstrate that the electroluminescence wavelength is determined by the nanotube's chiral index (n, m). The (n,m)-nanotube devices have been prepared by low-frequency dielectrophoresis from single-chirality nanotube dispersions. They have studied in detail the electroluminescence signal from the devices and assigned the 825 nm peaks to the excitonic E_{22} K-point interband transition by comparison of the electroluminescence spectra with corresponding photoluminescence excitation maps.

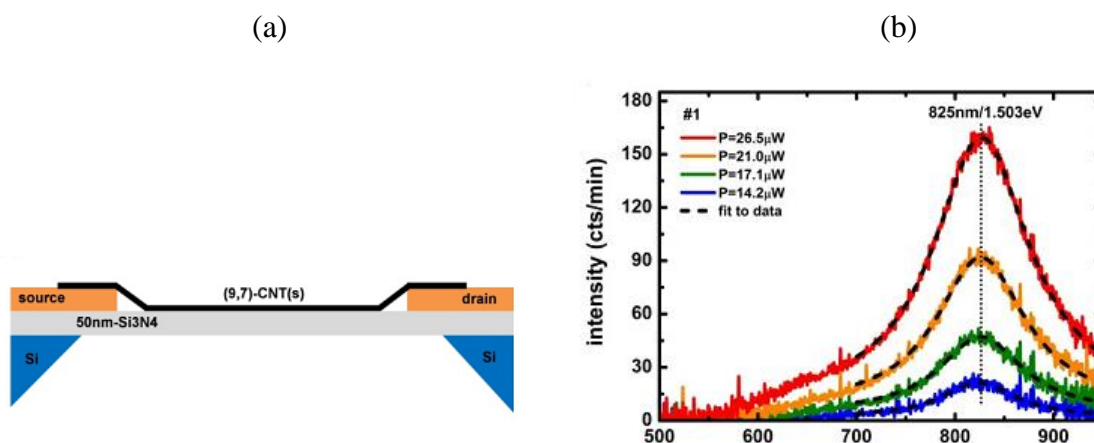


Figure 2.19: (a) Schematic cross section of the (9,7)-nanotube device. (b) Evolution of the electroluminescence spectra with driving power of (9,7)-CNT device [147]

Vijayaraghavan *et al.* [148] adopted a combination of single chirality nanotube suspensions made by chirality-selective polymer wrapping with ultra-large scale directed assembly by dielectrophoresis as the route to fabricating high-density arrays of individual, single chirality nanotube devices (Fig. 2.20). From Raman and photoluminescence (PL) spectroscopy, the single chirality assembly was confirmed. The

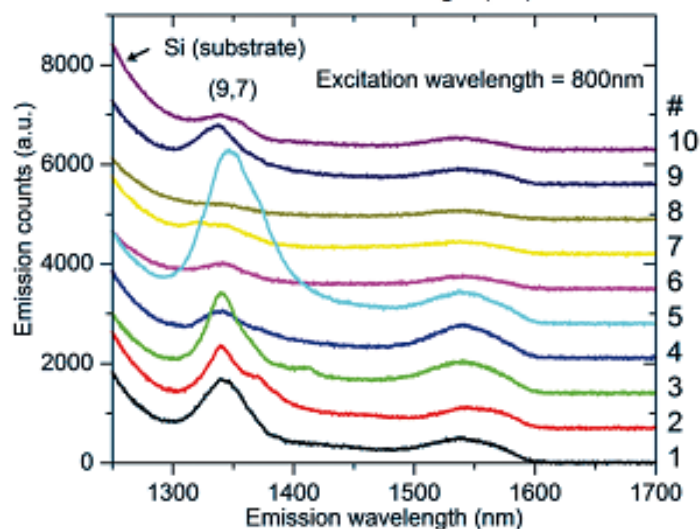


Figure 2.20: Photoluminescence spectra from 10 adjacent devices on a (9,7) SWCNT array, for 800 nm excitation wavelength. Each shows emission at 1345 nm, indicating the presence of a (9, 7) SWCNT [148].

Raman spectra was obtained on adjacent devices on an array deposited from the (9,7) suspension. The characteristic bright-exciton (BE) PL emission of a (9,7) nanotube, at 1345 nm was seen which corresponds to E_{11} . Their devices showed similar characteristics in PL, Raman, and VC-SEM, as expected for single-chirality devices.

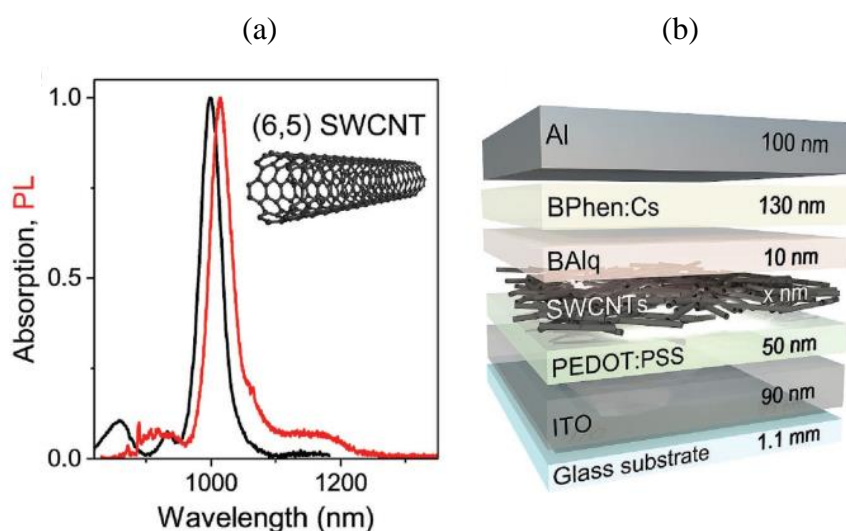


Figure 2.21: (a) Absorption and photoluminescence (PL) spectra of the (6,5) SWCNTs used as emitter material. The inset shows the molecular structure of a (6,5) SWCNT. (b) Schematic illustration for the OLED stack used by Graf *et al.* [134].

Graf *et al.* [134] demonstrated the first near-infrared (nIR) organic LED based on single-walled carbon nanotubes as the emitter (Fig. 2.21). They used (6,5) SWCNTs synthesized and purified by selective polymer-wrapping. A bare film of the purified material shows the characteristic absorption and photoluminescence (PL) spectrum of (6,5) SWCNTs with an emission peak at 1010 nm (corresponds to 1.228 eV), associated with excitonic emission from (6,5) SWCNTs. By using a multilayer stacked architecture with matching charge blocking and charge-transport layers, narrow-band electroluminescence at wavelengths between 1000 and 1200 nm was achieved by them, with spectral features characteristic of excitonic and trionic emission of the employed (6,5) SWCNTs.

Tayo *et al.* [107] reported GNR heterojunction of 7-AGNR and 11-AGNR, having individual bandgap of 1.54 eV and 0.16 eV, respectively. They showed that, by increasing the length of the 11-AGNR, band gap of the 7-11 GNR heterojunction can be tuned continuously between the band gap of the 7-AGNR (1.54 eV) and the band gap of the 11-AGNR (0.16 eV).

2.6.3 Selecting appropriate SWCNTs in CNT based LEDs for visible and NIR spectrum

a) SWCNTs for emitting light in visible spectrum

Retina of human eye consists of various nerve cells that can sense the change of light- its intensity, saturation, and most importantly—color. There are mainly two kinds of optically sensitive cells in retina- Rod cells and Cone cells. While rod cells work at dim light and show colorless contrast images at low-light environment, the cone cells respond at brighter light, and can differentiate among colors. There are three types of cone cells- one is most active at RED region of visible wavelength, another at GREEN region, and the third one at BLUE region.

A monochromatic light (or combination of monochromatic lights, that is a polychromatic or ordinary light) excites only these three kinds of cone cells, regardless of wavelength combination of light, Hence, combination of three, and only three wavelengths of light can give ordinary humans exact perception of color of any wavelength of light (Fig. 2.22).

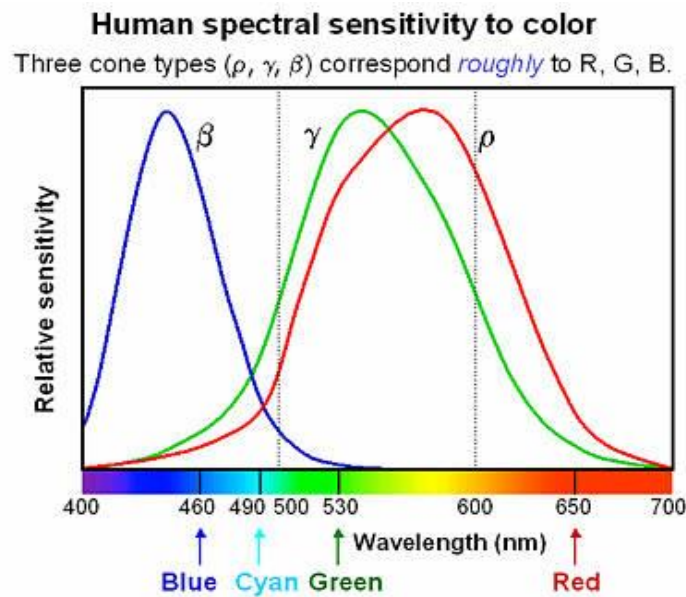


Figure 2.22: Human spectral sensitivity to color [55].

Different SWCNTs exhibit different optical transitions based on their chirality. For visible light emission from a SWCNT based LED, a number of SWCNTs and AGNRs can be identified using the information of their optical transition energies, specially the first optical transitions.

b) SWCNTs and AGNRs for emitting light in CIR (Color Infrared) spectrum

According to USDA Forest Service (2008), CIR imagery is a form of “*multispectral data that includes part of the visible light spectrum as well as the near infrared....*” And “*...is especially useful for vegetation mapping.*”

CIR image is a false color photograph (digital or film) that shows the reflected electromagnetic waves from an object accordingly,

- Near Infrared (NIR), which is invisible to the human eye, as red
- Green light as blue
- Red light as green

Although CIR photography was originally developed for the U.S. military in WWII to detect enemy camouflaged tanks, it is now used by government agencies (county, state, and federal) as well as the private sector and academia in numerous applications, such as the following,

- Crop and timber inventory and analysis in order to estimate yields
- Damage assessment to prioritize recovery efforts as after a forest fire or to verify insurance claims as after a hail storm on a field
- Impervious surface mapping in order to estimate stormwater run-off

The reasons for utilizing the tool of CIR imagery in addition to (or instead of) color imagery is, CIR imagery has better penetration through atmospheric haze than normal color imagery, because the shorter, easily scattered wavelengths (i.e. blue and violet) are filtered out CIR's ability to detect how an object responds to Near infrared (NIR) light (i.e. absorbs, transmits, or reflects) can reveal such land cover conditions, which are undetectable on color imagery, as,

- Stressed vegetation
- Moist areas in fields
- Plant identification (e.g. differentiate between hardwoods and conifers)

CIR uses reflected solar radiation in the 500 to 900 nm range, which encompasses portions of the following electromagnetic spectrum sections (Fig. 2.23),

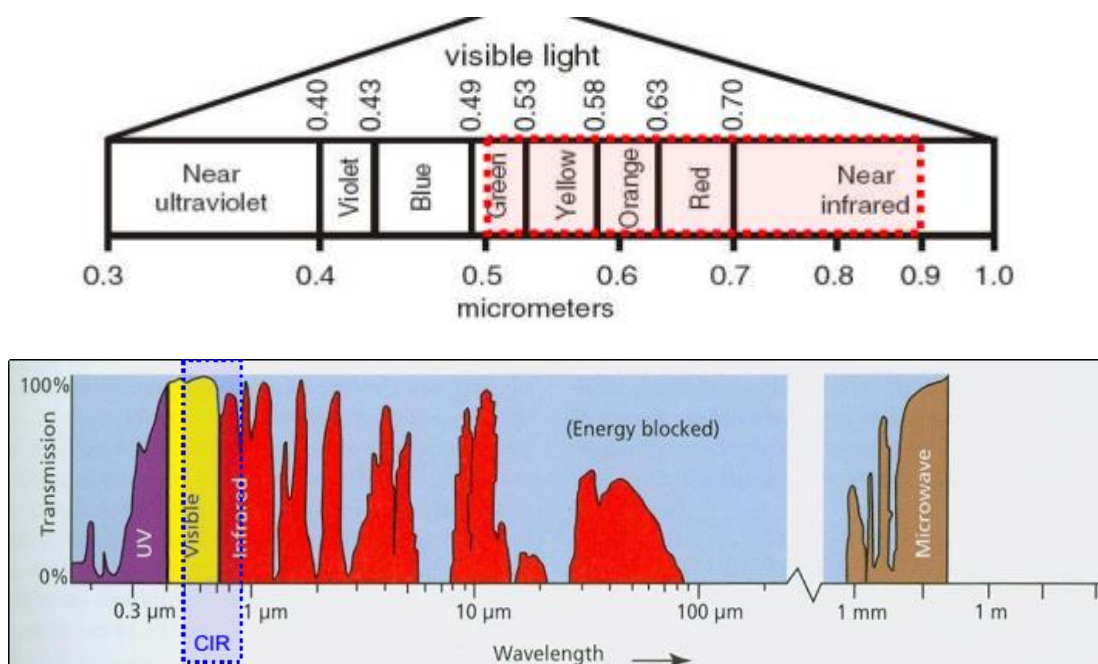


Figure 2.23: Color Infrared (CIR) Spectrum [55]

Visible light- The electromagnetic spectrum section from 0.4 to 0.7 μm (400 to 700 nm), which the human eye can detect as the colors from violet through red. CIR filters out blue wavelengths for a crisper image.

Near Infrared (NIR)- The electromagnetic spectrum section that extends beyond red from 0.7 to 1.0 μm (700 to 1000 nm), which the human eye cannot detect. CIR filters out the longer wavelength range of NIR from 0.9 to 1.0 μm (900 to 1000 nm) due to the decrease in atmospheric transmission or conversely the increase in absorption in this wavelength range.

The frequency equivalent of the wavelength range for CIR, which extends from 500 to 900 nm, would be 6.0×10^8 to 3.3×10^8 MHz. For emission in CIR spectrum using SWCNTs and AGNRs, appropriate SWCNTs and AGNRs can be identified using the information regarding their optical transitions.

CHAPTER 3

EMPIRICAL MODELING OF OPTICAL TRANSITIONS IN SWCNTs

In this chapter, a set of empirical relations between optical transitions and chirality of SWCNTs is devised which can predict parallel polarized optical transitions of any SWCNTs with high accuracy. Such relations between optical transitions and chirality (n, m) and consequent set of empirical equations can be an effective solution for estimating any optical transition energy of any SWCNTs, where required.

3.1 Empirical Modeling of Different Optical Transitions in SWCNTs

3.1.1 Semiconducting SWCNTs

As mentioned earlier, A SWCNT (n, m) is semiconducting if $\text{mod}(n-m, 3) = 1$ or 2 . This gives rise to two types of semiconducting SWCNTs, mod 1 type and mod 2 type. For developing proposed empirical model, focus will be on first seven optical transitions of semiconducting SWCNTs because so far experimental data are available only for these transitions. Also, studying these transitions are enough for almost all theoretical and practical purposes.

A large number of SWCNTs having chiral indices from $(4, 2)$ to $(35, 34)$ are considered. Corresponding diameter starts from 0.42 nm and extends up to 4.75 nm. There are total 654 SWCNTs in between these two chiral indices or diameter range where 426 are semiconducting tubes and 228 are metallic tubes. Out of 426 semiconducting SWCNTs, 218 tubes were found to be mod 1 type and 208 were mod 2 type based on $(n-m, 3) = 1$ or 2 . Values of first seven optical transitions energies of these semiconducting SWCNTs were recorded from multiple reports of relevant optical spectroscopic experiments [39,44,45,47,53, 123-127].

After examining measured optical transitions, it was observed that, for odd transitions ($E_{11}^S, E_{33}^S, \dots$), mod 1 type semiconducting SWCNTs have smaller transition energies than that of mod 2 type whereas, for even transitions ($E_{22}^S, E_{44}^S, \dots$), mod 1 type

semiconducting SWCNTs have larger transition energies than that of mod 2 type with comparable diameters. This is expected as discussed earlier [44]. This observation suggests that it will be convenient to study optical transition energies of mod 1 type and mod 2 type semiconducting SWCNTs separately so as to address their individual trend more precisely. For the same reason, it will be more effective to devise separate empirical relation for optical transitions of mod 1 and mod 2 types with their chiral indices.

First seven optical transitions of semiconducting SWCNTs were plotted against their diameters (d) which results an experimental 'Kataura plot', as shown in Fig. 3.1 (a) and (b), with upper and lower family branches for each transition. It was observed from the 'Kataura plot' that there is a basic symmetry in the nature of variation of each optical transition energy. Due to this observed symmetry, it is possible to express lower branches of all curves (representing mod 1 type for odd transitions and mod 2 type for even transitions) through a general empirical formula. Similarly, it is possible to express upper branches of all curves (representing mod 2 type for odd transitions and mod 1 type for even transitions) through another general empirical formula.

In order to discover the form of this general empirical formula, first seven optical transitions of semiconducting SWCNTs were again plotted against their diameters (d) but, now separately for both mod 1 and mod 2 types of each transition. All those plots were closely studied followed by some important findings. It was observed that, optical transitions decrease in general with increasing diameter (d) for each mod type but, this decreasing way follows abrupt ups and downs for each tube. This abrupt decreasing trend cannot be reflected just by a simple inverse relation of optical transition with diameter and need to incorporate other parameters. It is logical to assume that this abrupt trend is linked with unique chiral index of each tube. So, representation of this abrupt trend requires inclusion of suitable combination of chiral indices (n, m) in empirical relation. We found that all optical transitions maintain specific variation pattern with respect to two specific chiral indices combinations ($n+2m$) and ($2n-m$) for lower and upper branches in Kataura plot, respectively. These suggests family behavior of SWCNTs for ($n+2m$) and ($2n-m$) families in addition to previously reported ($2n+m$) and ($n-m$) families and incorporating these terms can precisely reflect the variation pattern for all optical transitions through an exponential relation. Thus, a $1/d$ term to represent the basic inverse relation of

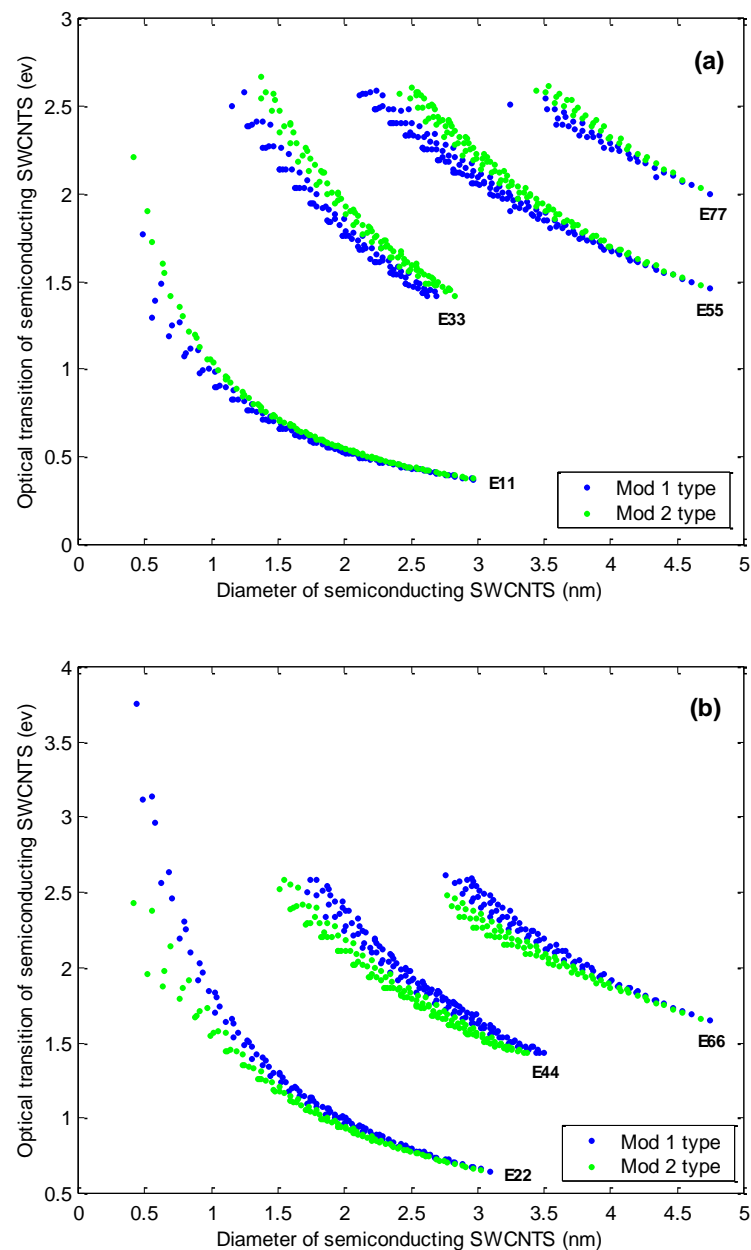


Figure 3.1. First seven optical transition energies of semiconducting SWCNTs, plotted against their diameters (Experimental ‘Kataura plot’) separately in (a) for odd transitions and in (b) for even transitions. Mod 1 type transitions (blue) form lower branches in odd transitions and upper branches in even transitions. Mod 2 type transitions (green) form lower branches in even transitions and upper branches in odd transitions.

optical transitions with diameter and an exponential term including these two specific chiral indices combinations $(n+2m)$ and $(2n-m)$ can give the complete form of proposed empirical relation for lower and upper branches, respectively along with some

numerical fitting parameters. An additional d term is included in the exponential term to incorporate curvature effect. If properly designed with other necessary numerical fitting parameters, it can faithfully reproduce all experimental Kataura plots of Fig. 3.1.

Following are the two resultant general empirical relation of first seven optical transitions with diameter and chiral indices of any semiconducting SWCNTs. For mod 1 type odd transitions ($E_{11}^S, E_{33}^S, E_{55}^S, E_{77}^S$) and mod 2 type even transitions ($E_{22}^S, E_{44}^S, E_{66}^S$) [lower branches of semiconducting curves in Kataura plot,

$$E_{ii} = \frac{A}{d} \exp\left(\frac{d - B}{n + 2m}\right) \quad (3.1)$$

For mod 2 type odd transitions ($E_{11}^S, E_{33}^S, E_{55}^S, E_{77}^S$) and mod 1 type even transitions ($E_{22}^S, E_{44}^S, E_{66}^S$) [upper branches of semiconducting curves in Kataura plot],

$$E_{ii} = \frac{A}{d} \exp\left(\frac{d - B}{2n - m}\right) \quad (3.2)$$

Here, only the values of A and B are different for different transition energies and mod types as given in Table 3.1.

Table 3.1 Parameters A and B for different optical transitions of semiconducting SWCNTs

Optical Transitions	No. of SWCNT Samples	MOD Type	A	B	% Mean Percentage Error
1 st transition (E_{11}^S)	208	1	1.11	3.5	0.84 %
		2	1.094	1.9	0.92 %
2 nd transition (E_{22}^S)	212	1	1.94	2	1.42 %
		2	1.96	4	2.27 %
3 rd transition (E_{33}^S)	187	1	4.12	6.8	1.06 %
		2	4.14	4.3	0.80 %
4 th transition (E_{44}^S)	256	1	4.98	3.6	0.84 %
		2	5.1	7.9	0.98 %
5 th transition (E_{55}^S)	246	1	7.2	10.5	1.07 %
		2	7.0	5.1	0.45 %
6 th transition (E_{66}^S)	159	1	8.06	5.9	0.51 %
		2	8.27	12.3	0.91 %
7 th transition (E_{77}^S)	70	1	10.75	18	0.47 %
		2	9.79	5.9	0.23 %

Using the above two general format of Eqn (3.1) and (3.2) and with the help of Table 3.1, a set of empirical formula will appear to predict the first seven optical transition energies of any semiconducting SWCNTs with high accuracy.

Experimental and empirical values of first seven optical transitions of semiconducting SWCNTs are plotted in Fig. 3.2 (a) and (b) for odd and even transitions, respectively, against their diameters. It can be easily noticed from these plots that empirical estimations matches very closely with experimental data over the full diameter range for all transitions both for mod 1 and mod 2 types. Accuracy is much high at higher diameters. Slight deviation is observed in some lower diameter tubes only but, they are within the

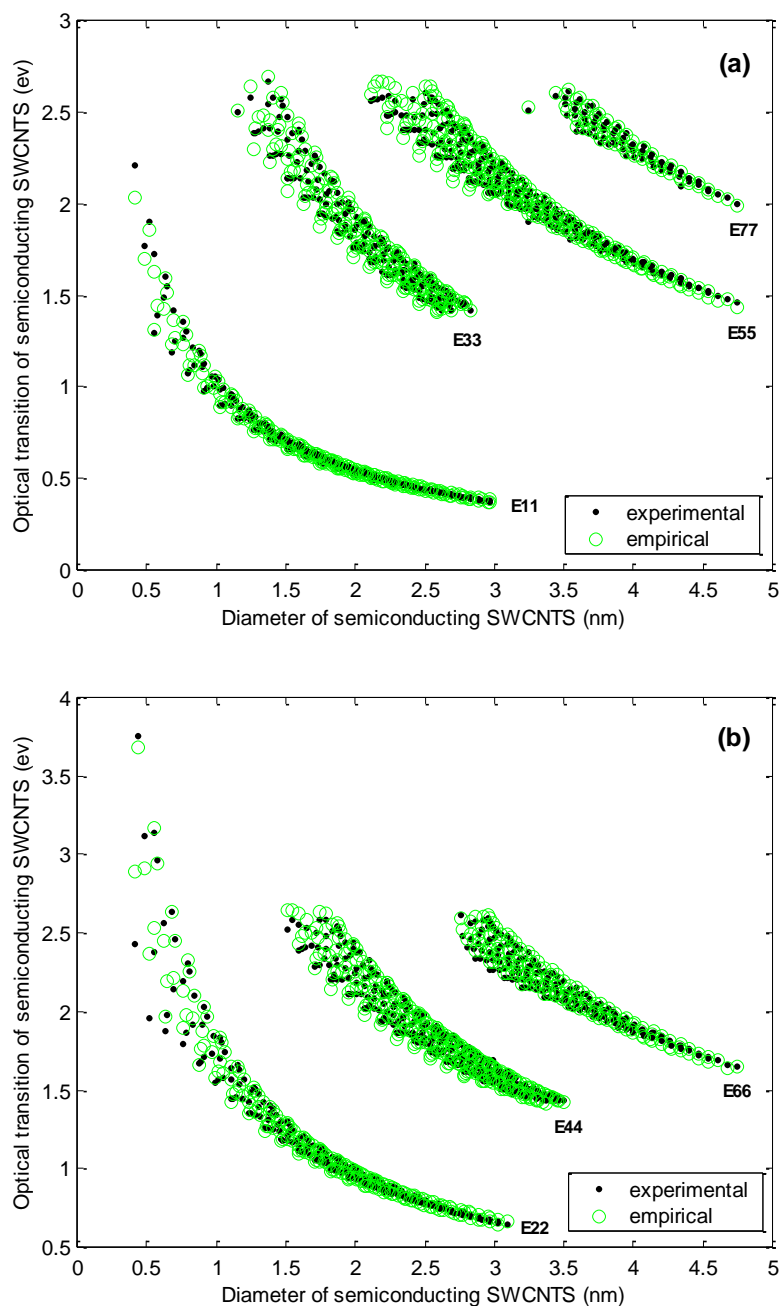


Figure 3.2: Experimental (black dot) and empirical (green circle) values of first seven optical transitions, plotted against diameters of semiconducting SWCNTs in (a) for four odd transitions and in (b) for three even transitions.

tolerance margin. For seven transitions with each mod type, there are total 14 cases listed in Table 3.1. For 10 of these cases, the average absolute error over the full diameter range is below 1%, for another 2 cases it goes slightly over 1% and only for one case it exceeds

2%. Thus, the proposed empirical relation can predict first seven optical transitions for both mod types with very high accuracy.

3.1.2 Metallic SWCNTs

A SWCNT (n, m) will be metallic if its $n-m = 3k$ (k is integer). This relation indicates that theoretically two third of the total SWCNTs are semiconducting and one third are metallic. Metallic nanotubes are a potential choice for nano-scale electrodes and 1-D quantum wires [128], transparent conductors and semi-transparent conductive coating [129, 130] and many similar nano-device applications.

Theoretical model derived from electronic band theory fails quantitatively to predict experimentally observed values of optical transitions for both semiconducting and metallic SWCNTs. Nanotube's 'curvature effect' [8, 9, 40, 49] and 'trigonal warping effect' [42] cause deviations in the electronic properties of nanotubes derived from the simple π -orbital graphene picture. Curvature causes π and σ states of nanotube's chemical bond to mix. This leads to increased hybridization between σ and π orbitals as the diameter of a SWCNT gets smaller [8, 9]. The σ - π hybridization effect has been considered and calculated in the literature [8, 9, 49]. The main result is that nanotubes satisfying $|n-m| = 3k$ ($k=0, 1, 2, \dots$) develop a small curvature-induced bandgap, and hence become quasi-metallic or small gap semiconductor [62]. Armchair nanotubes (n, n) are an exception because of their special symmetry, and only they remain truly metallic for all diameters [62]. Saito *et al.* [42] investigated the 'trigonal warping effect' analytically and derived expressions to estimate the corresponding deviation in optical transitions of metallic and semiconducting SWCNTs. They showed that trigonal warping causes splitting of the DOS peaks of metallic SWCNTs except for armchair tubes. Thus only armchair SWCNTs are unaffected due to curvature and trigonal warping and remain truly metallic.

As armchair nanotubes are the most pure kind of metallic SWCNTs, focus will be on armchair tubes. In many applications, researchers need to find or measure the optical transitions in metallic nanotubes. Authors [16, 39, 53, 127, 131-133] studied the properties of metallic SWCNTs and discussed the first, second and third optical transition energies of metallic SWCNTs. However, there is no easy way to calculate or predict those

transitions and one has to rely solely on experimental reports which are limited in number. Some empirical relations have been proposed [53, 127, 131-133] earlier but they involve too many parameters. Here, in this work, a concise empirical relation is devised to predict the second and third optical transitions in armchair metallic nanotubes which directly relates the optical transition value with any of the chiral index of armchair tubes. The proposed relation can give a quick as well as highly accurate prediction of the second and third optical transitions in armchair metallic SWCNTs.

Optical transition energies for metallic armchair (n, n) SWCNTs with chiral index $(15,15)$ to $(35,35)$ are closely studied here. There are total 21 armchair SWCNTs within these two chiral index range having diameter from 2 nm to 4.8 nm. The main reason for using this chiral indices range is experimental data of the second and third optical transition energies is available only for these diameter range till now. Values of optical transition energies of these tubes are taken from various experimental reports [39, 53, 127, 131-133] which gives the second optical transition energy of 16 armchair tubes ranging from chiral index $(15,15)$ to $(30,30)$ and the third optical transition energy of 13 armchair tubes ranging from chiral index $(23,23)$ to $(35,35)$.

The objective here is to devise a simple empirical relation between the chirality and optical transition of armchair metallic tubes so that the value of the second or third optical transition of these tubes can be predicted directly from its chiral index (n, n) .

From Kataura plot of metallic transitions, it was noticed that armchair tubes lie at the center of each $(2n+m)$ family branch. This observation regarding position of armchair SWCNTs in Kataura plot is important for next steps. After a careful study of the symmetry in the structure of armchair tubes, their optical transitions and their relation with corresponding chiral index, it was observed that an exponential empirical relation that we already discovered for semiconducting tubes can also be used here after necessary modifications and symmetry considerations for armchair SWCNTs. Accordingly, the following empirical formula was devised to predict the optical transitions from corresponding chiral index n of any armchair nanotube (n, n) .

For the second optical transition energy (E_{66}) of armchair SWCNTs,

$$E_{66} = \left(\frac{50}{n}\right) e^{\left(-\frac{4.3}{n}\right)} \quad (3.3)$$

For the third optical transition energy (E_{99}) of armchair SWCNTs,

$$E_{99} = \left(\frac{75}{n}\right) e^{\left(-\frac{6}{n}\right)} \quad (3.4)$$

The empirical values of the second and third optical transition energies of these armchair SWCNTs with chiral index (15,15) to (35,35) have been calculated using the empirical Eqn. (3.3) and (3.4). The results agree well with experimental values of the second and third optical transitions of corresponding metallic armchair SWCNTs.

Eqn. (3.3) and (3.4) can be further analyzed in following way,

The diameter of a SWCNT (n, m) is expressed by, $d = \sqrt{3(n^2 + nm + m^2)} a_{cc} / \pi$, where, a_{cc} = carbon-carbon bond length = 0.142 nm. For armchair SWCNTs, $n=m$, which gives, $d = 0.1356 n$ nm or, $n = 7.375 d$ nm. If the exponential term of Eqn. (3.3) and (3.4) are expanded using this trivial relation between n and d , the expressions for the second and third optical transitions become,

$$E_{66} = \frac{6.78}{d} - \frac{3.95}{d^2} + \frac{1.15}{d^3} - \frac{0.224}{d^4} + \dots \quad (3.5)$$

$$E_{99} = \frac{10.17}{d} - \frac{8.27}{d^2} + \frac{3.36}{d^3} - \frac{0.91}{d^4} + \dots \quad (3.6)$$

For higher diameter tubes, only the first and second term of each equation is significant and subsequent terms can be ignored. This gives a second order relation for armchair tubes.

Experimental [39] and the empirical values of optical transition energies along with chiral index (n, n) and diameter of these armchair tubes are shown in Table 3.2 and 3.3 and plotted in Fig. 3.3 (a) and (b).

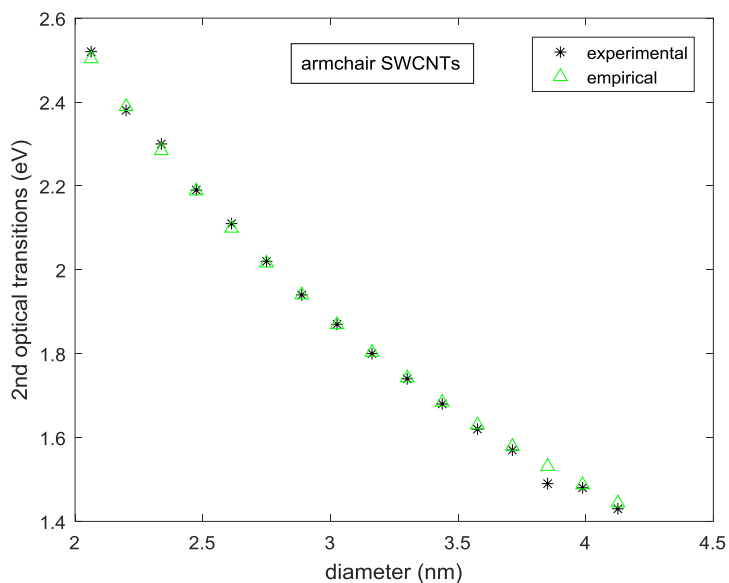
Table 3.2 Experimental [39] and the empirical values of the second optical transition energy (Eqn. 3.3) of 16 armchair SWCNTs

n	m	Diameter (nm)	Exp E_{66} (eV)	Emp E_{66} (eV)
15	15	2.063	2.52	2.503
16	16	2.200	2.38	2.389
17	17	2.338	2.30	2.284
18	18	2.475	2.19	2.188
19	19	2.613	2.11	2.099
20	20	2.750	2.02	2.016
21	21	2.888	1.94	1.940
22	22	3.026	1.87	1.869
23	23	3.163	1.80	1.803
24	24	3.301	1.74	1.742
25	25	3.438	1.68	1.684
26	26	3.576	1.62	1.630
27	27	3.713	1.57	1.579
28	28	3.851	1.49	1.531
29	29	3.988	1.48	1.487
30	30	4.126	1.43	1.444

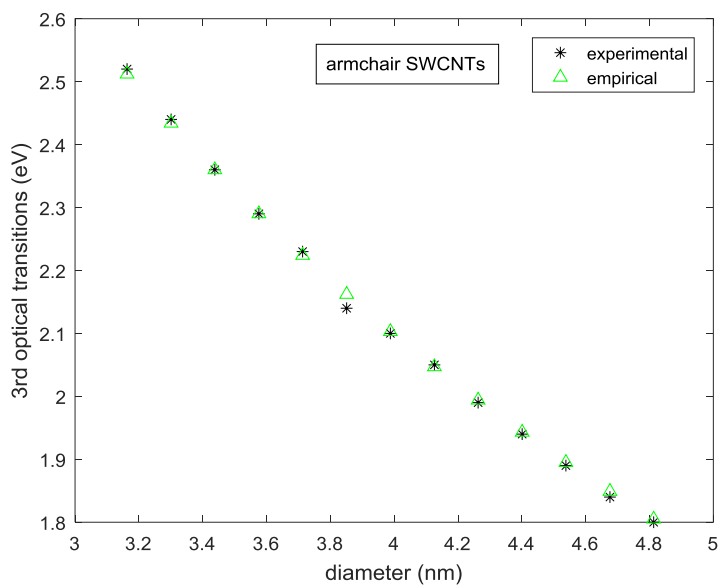
Table 3.3 Experimental [39] and the empirical values of the third optical transition energy (Eqn. 3.4) of 13 armchair SWCNTs

n	m	Diameter (nm)	Exp E₉₉ (eV)	Emp E₉₉ (eV)
23	23	3.163	2.52	2.512
24	24	3.301	2.44	2.434
25	25	3.438	2.36	2.360
26	26	3.576	2.29	2.290
27	27	3.713	2.23	2.224
28	28	3.851	2.14	2.162
29	29	3.988	2.10	2.103
30	30	4.126	2.05	2.047
31	31	4.263	1.99	1.994
32	32	4.401	1.94	1.943
33	33	4.538	1.89	1.895
34	34	4.676	1.84	1.849
35	35	4.813	1.80	1.805

In Table 3.2 and 3.3, the empirical result for the second and third optical transition (E_{66}) from this work using Eqn. (3.3) and Eqn. (3.4), respectively, and the experimentally measured values, both are provided so as to compare them. From these two Tables it can be observed clearly that the predicted values from Eqn. (3.3) and (3.4) are very close to the experimental values. For the second optical transition (E_{66}) the average absolute error



(a)



(b)

Figure 3.3: Experimental value(black), the empirical value from this work(red) and the empirical value from earlier work (blue) of optical transition vs diameter of armchair SWCNTs, (a) the second optical transition, (b) the third optical transition.

in prediction using Eqn. (3.3) was found to be only 0.009 eV and corresponding percent average absolute error is only 0.53%. Similarly, for the third optical transition (E_{99}) the average absolute error in prediction using Eqn. (3.4) was found to be only 0.006 eV and

corresponding percent average absolute error is only 0.27%. Thus, the empirical model proposed here can predict the value of optical transition energies of armchair tubes with higher accuracy.

Figure 3.3 (a) and (b) shows the plot of experimental and the empirical values of the second and third optical transition energies, respectively, of metallic armchair SWCNTs with respect to their diameters. Again it can be observed from these two plots that, for both optical transitions, the empirical values estimated by Eqn. (3.3) and (3.4) closely follow the experimental values over the full diameter range under consideration. This curve can be extrapolated using the two empirical relations from above to predict other armchair tubes beyond this diameter range.

One interesting observation from the second and third optical transition energies of armchair SWCNTs is, the ratio of the third transition to the second transition of same armchair tubes are equal to a constant whose value around 1.4. This observation further facilitate the calculation of higher optical transitions in metallic armchair tubes as one can know the third transition energy value of a tube by knowing the value of the second transition multiplied by that constant. This relation also indicates the built in high symmetry in armchair SWCNTs which causes their higher optical transition energy values to grow in a systematic order. This relation may also help to study the behaviour of metallic armchair tubes in a more systematic manner.

3.1.3 Zigzag SWCNTs

As mentioned earlier, based on the direction of wrapping vector $C_h = na_1 + ma_2$, SWCNTs are divided into three categories; armchair (n, n), zigzag (n, 0), and chiral (n, m) with $n > m > 0$. When the wrapping vector C_h lies purely along one of the two basis vectors, $m=0$, C-C bonds become parallel to the tube axis and the carbon nanotube is said to be of “zigzag” type due to zigzag-like pattern of its atoms around the tube circumference having mirror symmetry. For zigzag case ($m=0$), the expression of diameter reduces to, $d_t = \frac{a_0}{\sqrt{3}}$, where, $a_0 =$ length of graphite basis vector (lattice constant) = $|a_1| = |a_2| = \sqrt{3}a_{cc} = 0.249$ nm with $a_{cc} =$ C–C bond length = 0.144 nm. Also, for zigzag tubes, Chiral angle $\theta = 0^\circ$.

Among three categories of SWCNTs, Zigzag tubes bear special symmetry and can be both metallic and semiconducting depending on the value of n . Zigzag SWCNTs have some other special features for which they are studied extensively by the researchers. It has been reported that curvature effect is more dominant on zigzag $(n, 0)$ than armchair tubes (n, n) [135]. Due to special symmetry in zigzag tubes, many authors [9, 61, 81, 136] preferred this type to carry out first principle (quantum mechanical) calculations of SWCNT band structure [135] as same calculation require a large amount of computational time for chiral tubes. They reported large discrepancies between tight binding and first principles calculations of the band gap values of different zigzag nanotubes. It has been found that, while tight-binding calculations predict small diameter $(4,0)$ and $(5,0)$ zigzag nanotubes to be semiconducting with band gaps exceeding 1 eV, first principle calculation shows that they are metallic. Similarly, while tight binding calculations predict that the $(6,0)$ zigzag nanotube is quasi metallic with a band gap of approximately 200 meV, first principle calculations indicate that they are truly metallic [62].

Also, due to trigonal asymmetry near the six corners of hexagonal grapheme Brillouine zone, difference in transition energies for mod 1 and mod 2 type semiconducting SWCNTs occurs which is known as ‘Trigonal warping effect’[42]. Trigonal warping splits DOS of metallic tubes which is highest for $(3n, 0)$ metallic zigzag tubes, whereas no splitting for Semiconducting tubes [42]. Thus, Both curvature-induced gap and trigonal-warping splitting are maximum for $(3n, 0)$ zigzag species.

Sfeir *et al.* [44] observed that the mod 1 type zigzag or chiral semiconducting SWCNT have smaller transition energies than mod 2 type for odd transitions $(E_{11}^S, E_{33}^S, \dots)$ whereas, mod 2 type semiconducting SWCNT have smaller transition energies than mod 1 type for even transitions $(E_{22}^S, E_{44}^S, \dots)$ with comparable diameters. Also, systematic pattern of optical transition energies is observed in Kataura plot, depending on their mod value. SWCNTs with same $(2n+m)$ values form branches in Kataura plot [41]. SWCNTs associated with each branch are termed as member of that $(2n+m)$ family [135].

The main focus of this work will be semiconducting zigzag SWCNTs due to their unique features discussed so far. It is necessary for the scientist to know the optical transitions in semiconducting zigzag SWCNTs for their suitable application. Authors[9, 61, 81,

135,] studied the properties of semiconducting Zigzag SWCNTs but their studies are limited to mainly first and second optical transition energies of semiconducting SWCNTs. Recently Liu *et al.* [39] studied the matter more extensively and carried a series of optical experiments to measure optical transition energies of numerous SWCNTs. Experimental data from the work of Liu *et al.* [39] is the primary source of optical transitions of semiconducting zigzag SWCNTs used in this work which were cross checked with the earlier report of Weisman *et al.* [45] for first and second optical transition energies. Though it is needed to know the optical transitions in semiconducting zigzag nanotubes for their relevant applications but, at present no simple method exists to calculate their optical transitions due to failure of conventional TB model. Few empirical models exist only for 1st and 2nd optical transition energies, but higher optical transitions are also important for the optics of large diameter semiconducting SWCNTs, since for $d_t > 1.3$ nm, E_{22} is already in the infrared range.

The nature of first five optical transitions in semiconducting SWCNTs was studied and then devised a concise equation that can give highly accurate estimation of these five higher optical transitions i.e. 1st, 2nd, 3rd, 4th and 5th transitions of semiconducting zigzag SWCNTs directly from their chiral index n .

Optical transition energies for semiconducting zigzag (n,0) and nearly zigzag (n, 1) SWCNTs with chiral index (7,0) to (35,0) and nearly zigzag tubes with chiral index (6,1) to (35,1) were closely studied here. There are total 59 SWCNTs within these two chiral index range of which 29 are zigzag having diameter from 0.556 nm to 2.78 nm and 30 are nearly zigzag having diameter from 0.521 nm to 2.82 nm. Values of optical transition energies of these tubes were recorded from various experimental reports [45, 39] with a special focus on the work of Liu *et al.* [39] which is relatively recent and provides wide range of experimental data. From these experimental reports, 1st, 2nd, 3rd, 4th, and 5th optical transition values were available for 26, 28, 25, 19 and 8 samples, respectively, out of 59 zigzag and nearly zigzag tubes.

Now, an attempt will be made here to devise a simple empirical relation between the chiral index and optical transition of semiconducting zigzag SWCNTs so that the value of 1st to 5th optical transition of these tubes can be predicted directly from just one of their first chiral index n . It is noticed from Fig. 3.4 (a) that chirality changes from armchair (or

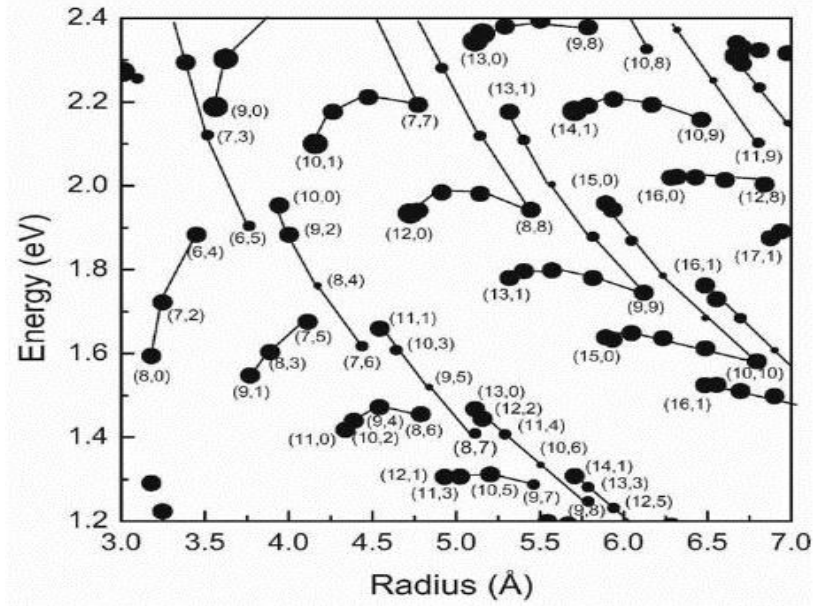


Figure 3.4 Experimental Kataura plot. The lines connect $2n + m$ families of both mod 1 and mod 2 type SWCNTs [71].

nearly armchair) to zigzag (or nearly zigzag) along same $(2n+m)$ family lines. The lines connect $2n + m$ families. Thus, all zigzag and nearly zigzag SWCNTs lie at the tip of each branch. This observation regarding position of zigzag SWCNTs in Kataura plot is important for next steps.

After a careful study of the symmetry in the structure of zigzag and nearly zigzag tubes as well as considering the placement of their optical transitions in Kataura plot, it was found that all zigzag and nearly zigzag tubes can be brought under a single non-linear curve by connecting the tip of each branch in Kataura plot either for mod 1 or for mod 2 type semiconducting SWCNTs. Thus, an exponential empirical relation that was already discovered for semiconducting tubes can also be used here after necessary modifications and symmetry considerations for zigzag SWCNTs. Based on these observation, following empirical formula was devised to predict the 1st, 2nd, 3rd, 4th and 5th optical transition energies of Semi-conducting zigzag $(n, 0)$ and nearly zigzag $(n,1)$ SWCNTs (denoted by E_{11} , E_{22} , E_{33} , E_{44} and E_{55} , respectively) from corresponding chiral index n ,

$$E_{nm} = \frac{A}{n} e^{-\frac{B}{n}} \quad (3.7)$$

Where, values of A and B from 1st to 5th transitions (both mod 1 and mod 2 type) of zigzag and nearly zigzag SWCNTs are given in Table 3.4 and corresponding transitions are plotted from Fig. 3.5 to 3.7.

Table 3.4 Parameters A and B for different optical transitions of semiconducting zigzag SWCNTs

Optical Transitions	No. of SWCNT Samples	MOD Type	A	B	% Mean Percentage Error
1 st transition (E_{11}^S)	26	1	15	3.6	1.09 %
		2	14.1	1	1.95 %
2 nd transition (E_{22}^S)	28	1	25.5	1	2.65 %
		2	27	4.5	2.50 %
3 rd transition (E_{33}^S)	25	1	56.5	6.5	0.80 %
		2	54.5	2.5	0.89 %
4 th transition (E_{44}^S)	19	1	65.4	1.9	0.91 %
		2	69.7	7.5	0.67 %
5 th transition (E_{55}^S)	8	1	99	10	0.57 %
		2	91.5	3	0.86 %

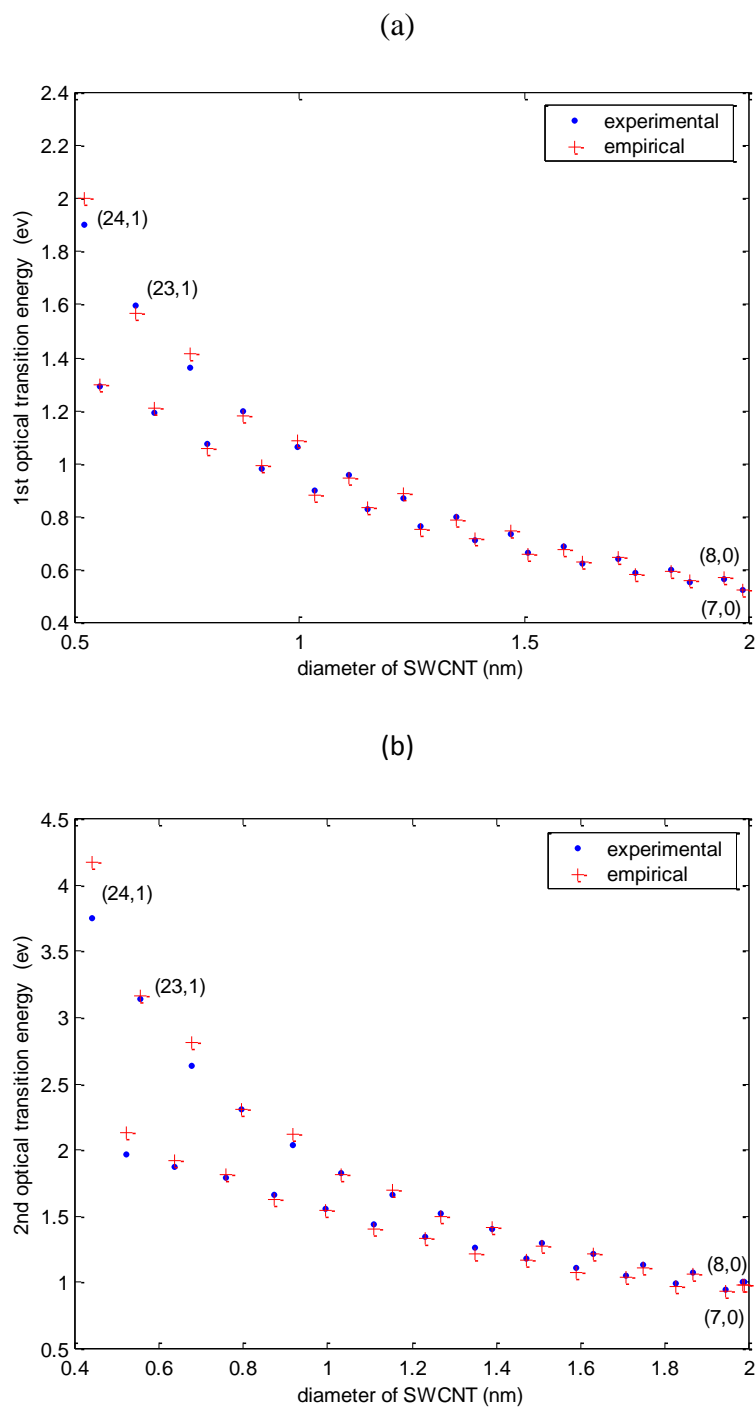


Figure 3.5 Experimental value (blue dot) and empirical value from this work (red cross) for (a) first transition (E_{11}) and (b) second transition (E_{22}) energies of semiconducting zigzag and nearly zigzag SWCNTs.

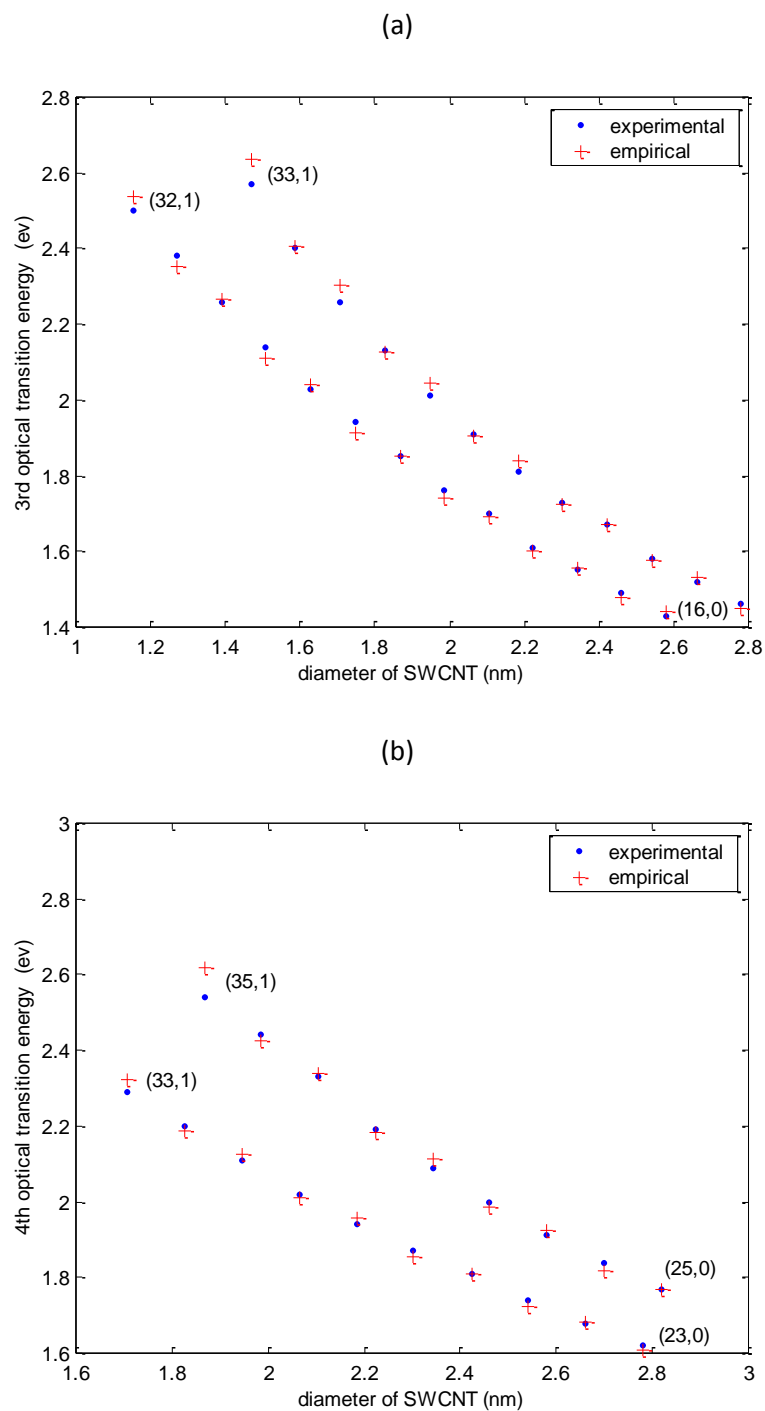


Figure 3.6 Experimental value (blue dot) and empirical value from this work (red cross) for (a) third transition (E_{33}) and (b) fourth transition (E_{44}) energies of semiconducting zigzag and nearly zigzag SWCNTs.

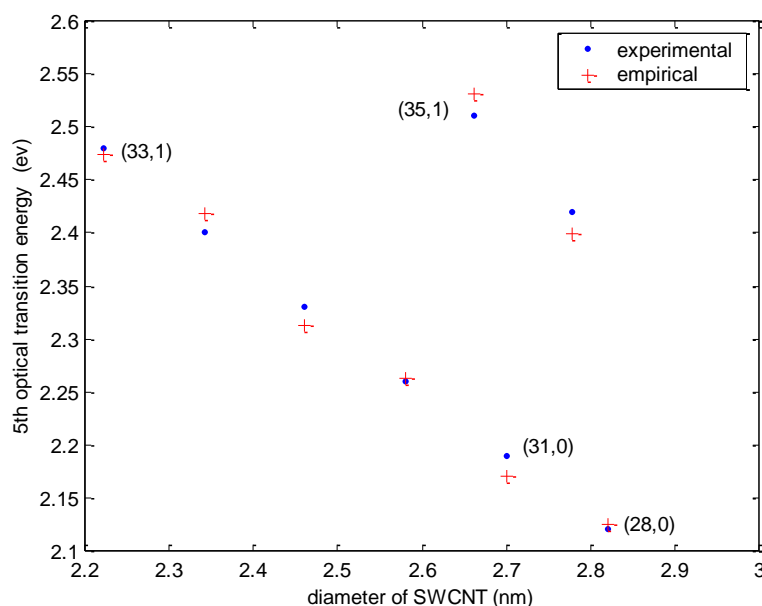


Figure 3.7 Experimental value (blue dot) and empirical value from this work (red cross) for fifth transition (E_{55}) energies of semiconducting zigzag and nearly zigzag SWCNTs.

Empirical values of 1st to 5th transitions (both mod 1 and mod 2 type) of zigzag SWCNTs with chiral index (7,0) to (35,0) and nearly zigzag SWCNTs with chiral index (6,1) to (35,1) were calculated using empirical equations (3.7). Calculated results agree well with experimental values of all five optical transitions of corresponding semiconducting zigzag and nearly zigzag SWCNTs. Thus, Eqn (3.7) gives quite simple expressions to calculate the value of optical transitions directly from their only chiral index n .

Table 3.4 also shows % average absolute error between experimental [39] and empirical values of five optical transition energies of these zigzag tubes. The % average absolute error is within 2% for 1st transition, within 3% for 2nd transition and within 1% for 3rd, 4th and 5th transitions. Thus, the proposed empirical relation can give the value of first optical transition energies of semiconducting zigzag and nearly zigzag SWCNTs with good accuracy.

Figure 3.5 to 3.7 show the plot of experimental and empirical values of 1st to 5th optical transition energies, respectively, of semiconducting zigzag and nearly zigzag SWCNTs with respect to their diameters. It can be once again observed from these plots that, for all five

optical transitions, empirical values predicted by Eqn. (3.7) are very close to the experimental values over the full diameter range under consideration. This curve can be extrapolated using above two empirical relations to predict other zigzag tubes beyond this diameter range.

In general, the proposed empirical equations from Eqn (3.7) give nearly accurate prediction of first five optical transitions of semiconducting zigzag and nearly zigzag SWCNTs. The general form of the equations for all five transitions also shows how optical transitions in any zigzag type SWCNTs are symmetrically linked with its single chiral index n .

The result of this work is significant because though there are good number of works on how to calculate or determine optical transition energies in SWCNTs, but, none of those works made dedicated investigation of zigzag tubes so as to discover the unique characteristics of optical transitions in this type of tubes as depicted in Kataura plot. Also, most of the previous works concentrated mainly on first and second optical transitions only whereas this work covered first to fifth optical transitions. Noticeable symmetry was found in the relative position of optical transitions of semiconducting zigzag and nearly zigzag SWCNTs in Kataura plot for all five transitions which made it possible for us to express them through a single expression of Eqn. (3.7). Thus, this work revealed that optical transitions in semiconducting zigzag and nearly zigzag SWCNTs have symmetrical characteristics with respect to their chirality and can be expressed through a general relation.

3.2 Conclusions

Theoretical model derived from electronic band theory failed to give accurate calculation of optical transitions in SWCNTs. Here, optical transitions energies in semiconducting and metallic SWCNTs are closely studied. New symmetrical behavior of different optical transitions in experimental Kataura plot is observed which is exploited here to find a correlation between optical transitions and chirality of individual tubes. The observations and findings are coined with other relevant observations from earlier theoretical and experimental models. Based on these analysis, a set of empirical relations for calculating different optical transitions in semiconducting and metallic SWCNTs are developed here.

Metallic armchair tubes and semiconducting zigzag and nearly zigzag tubes are studied separately due to their unique geometric symmetry and some exceptional electronic behaviors which made them different from other tubes. It is noticed that, nanotubes satisfying $|n-m| = 3k$ (k is an integer) develop a small curvature-induced bandgap and hence become quasi-metallic or small gap semiconductor except the armchair nanotubes (n, n) which remain truly metallic for all diameters. Similarly, curvature effect and trigonal warping effect on electronic bandstructure are maximum for zigzag types. Based on the position of armchair tubes at the center and that of zigzag tubes at the tip of each $(2n+m)$ family branch in Kataura plot, a nonlinear relation is devised between their optical transitions and chiral index n .

Using the proposed empirical models, first seven optical transitions of 426 semiconducting (n, m) SWCNTs, second and third optical transitions of 21 metallic armchair (n, n) SWCNTs and first five optical transitions of 29 zigzag $(n,0)$ and 30 nearly zigzag $(n,1)$ SWCNTs are calculated. Estimated values were compared with available experimental data and excellent agreement was found with experimentally measured values for all transitions over the full diameter range. Thus, proposed empirical relations provide a quick method to calculate the optical transition energies of these SWCNTs. The empirical model proposed here is much simpler than earlier models and the resultant expressions from the proposed model are concise and compact involving only few parameters. Furthermore, the proposed empirical model has practical implications in developing empirical Kataura plot for determining chiral index (n, m) of unknown semiconducting SWCNTs and predicting the electronic behaviour of a particular SWCNT in CNT based diodes and FETs. Moreover, because of the symmetry in Kataura plot for different transitions, the proposed empirical model can be extended further for higher diameters or higher transitions of semiconducting or metallic SWCNTs in future. Thus, the proposed empirical model provides an insight into electronic structure of SWCNTs as well as helps selecting appropriate SWCNTs for relevant applications.

CHAPTER-4

POTENTIAL APPLICATIONS OF THE PROPOSED EMPIRICAL MODELS FOR SWCNTS

4.1 Potential Applications of the Proposed Model

The proposed empirical models for optical transitions in semiconducting and metallic SWCNTs, as presented in the last chapter, and corresponding empirical relations for estimating different optical transition energies in SWCNTs can be used for a number of purposes. Few potential applications are,

- After the synthesis of SWCNTs, assignment of proper chirality to each produced sample is always a necessity for their sorting and precise applications. So far no single method can be considered as fully dependable to determine the chirality of unknown samples of SWCNTs. Proposed empirical relations of this work can help in determining chiral index (n, m) of unknown SWCNT through back calculation if its diameter and one of the optical transitions is known.
- Using prior information of first optical transitions in semiconducting SWCNTs, the emission spectrum of a chirality specified SWCNT based LED can be predicted.
- Suitable combination of SWCNTs can be identified for emitting different colors of light in the visible and NIR spectrum from SWCNT based LEDs.
- The proposed empirical relation can also provide the insight to find internal symmetry between different optical transitions of semiconducting and metallic SWCNTs and how they are precisely linked with nanotube chirality.

Subsequent sections will demonstrate these applications.

4.2 Improved Technique for Chirality Assignment of SWCNTs

Experimental determination of the chirality (n, m) of SWCNTs has been a requirement ever since their discovery. Identification of spectroscopic features and correlating them with

nanotube's physical structure is always necessary to purify, identify, separate and sort nanotubes after their production [126, 136]. Knowing the chirality is also important for many applications of SWCNTs in device level so as to select the specific SWCNT with required electronic and optical properties.

Resonant Raman Scattering (RRS) is a reliable, straight-forward and hence most widely used technique for nondestructive chiral index assignment [127]. RRS provides two important pieces of information; one of the optical transition energies (E_{ii}) and the RBM frequency (ω_{rbm}). This ω_{rbm} then gives diameter d_t as they two are inversely related through a semi-empirical relation [138, 139]. Earlier approach was to plot all E_{ii} versus d_t (from ω_{rbm}) to form an experimental Kataura plot which is mapped with an existing theoretical plot to give one-to-one correspondence for each chirality by observing the $(2n+m)$ family pattern [127]. Unfortunately, the uniqueness of this transformation may be hampered in this process by possible error involved in experimental E_{ii} value or empirical calculation of d_t from ω_{rbm} . Moreover, pattern recognition is possible only if the Raman spectrum shows a set of different RBMs. This is only the case for samples containing different kinds of nanotubes, i.e. produced as ensembles of nanotubes. When all observed Raman spectra show only one RBM, e.g. for an isolated tube or when the sample contains only one kind of chiral indices (n, m) , there is no scope for pattern recognition. In such case, quality of the assignment fully depends on the chosen theoretical plot and may lead to ambiguity.

The objective of this part is to propose an improved method for chirality assignment of isolated SWCNT using Raman G- mode versus diameter plot in addition to Kataura plot so as to determine the $(2n+m)$ family of an unknown SWCNT more accurately and then using this to determine the chiral index (n,m) of unknown SWCNT by solving basic structural relation between diameter and chiral index (n,m) of SWCNT without any need of existing pattern recognition process.

4.2.1 Chirality assignment using the empirical model

The one-dimensionality of the nanotubes gives rise to 1D subbands and optical transitions can only occur between those mirror subbands. During Resonant Raman Spectroscopy

(RRS) of SWCNT, one of the sub-band comes in resonance with incident laser from which the value of that optical transition energy can be known. Radial Breathing Mode (RBM) [138, 139] and G mode [140, 141] are two main features for SWCNT in Raman spectra. RBM corresponds to the coherent vibration of the carbon atoms in radial direction, usually occurs between frequency 120 and 350 cm^{-1} [126]. G-band comprises two main features, the so-called G- and G+ components, associated, respectively, with vibrations of the carbon atoms along the circumferential direction and along the nanotube axis and usually occur between frequency 1500 and 1600 cm^{-1} [140, 141]. Thus, three important pieces of information can be collected from RRS of SWCNT; one of the optical transition energies (E_{ii}), the RBM frequency (ω_{rbm}) and G (G- and G+) mode frequencies.

In the proposed new technique, two main tools are needed; an experimental or empirical G-frequency vs d_t plot and experimental or empirical optical transition energies vs d_t plot, commonly known as Kataura plot, which is now available from the empirical model presented in previous chapter. Necessary data to construct these two plots can be found from numerous experimental reports on resonant Raman spectroscopy (RRS) of SWCNTs. Here, for demonstration purpose, concise version of two such plots are presented based on values of second optical transition energy (E_{22}), RBM mode and G mode frequencies of 13 SWCNTs. Experimental data of E_{22} and ω_{rbm} are taken from [140] and experimental data of G- mode frequency shift of these SWCNTs are taken from [142, 143] who obtained the G- and G+ peak position from RRS experiments on a number of highly purified single chirality (n, m) samples. The value of d_t of each SWCNT can now be calculated from ω_{rbm} as they two are correlated through following semi empirical relation [139], $\omega_{\text{rbm}} = A/d_t + B$. It is important to note that value of A and B varies due to different experimental environment. So, value of RBM mode frequency and the value of A and B must be taken from same experimental report for correct determination of the diameter of SWCNTs. For present source of RRS data of ω_{rbm} , $A=223$ and $B=10$ [127]. Using the calculated d_t , the sample version of G- frequency vs d_t plot and E_{22} vs d_t plot are found, as shown in Fig. 4.1 and Fig. 4.2, respectively.

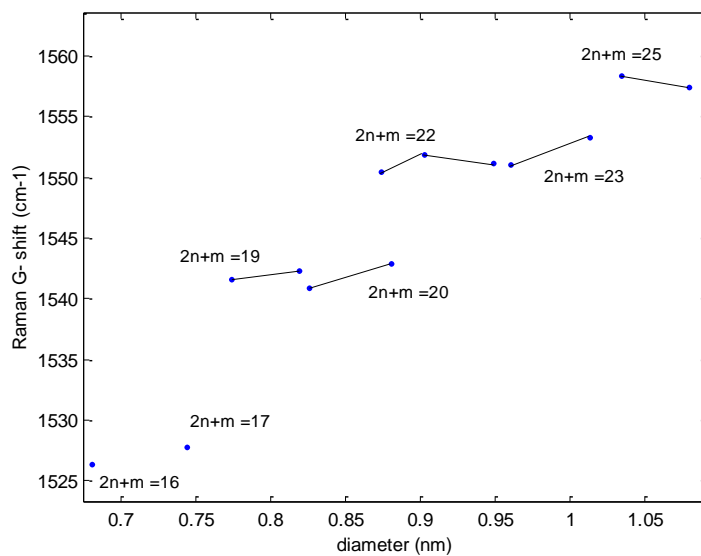


Figure 4.1: Experimental G- shift [141] against calculated d_t from experimental ω_{rbm} [141] for 13 SWCNTs. Dot (blue) shows individual SWCNT and solid lines (black) connect members of same $(2n+m)$ family.

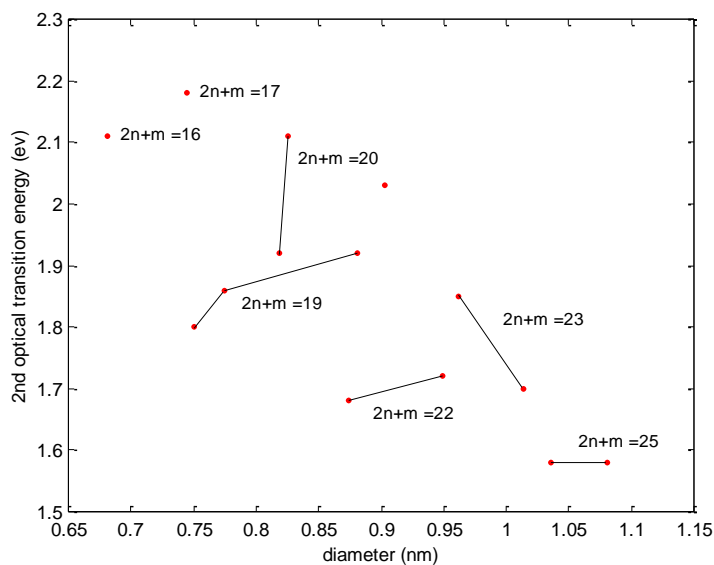


Figure 4.2: Empirical E_{22} from proposed model against calculated d_t from experimental ω_{rbm} [141] for 13 SWCNTs. Dot (red) shows individual SWCNT and solid lines (black) connect members of same $(2n+m)$ family.

The points whose value of $2n+m$ is equal are belongs to the same family. It is reported both theoretically and experimentally [141] that both G- frequency vs d_t plot and E_{22} vs d_t plot shows distinguished $(2n+m)$ family pattern. In both of these Figures, $(2n+m)$ families are shown by solid lines connecting members of a particular family. It must be noted that, here limited number of SWCNTs were used to build these plots and hence all members of each $(2n+m)$ family branch are not present in these two graphs.

To find out the chiral index (n, m) of an unknown SWCNT, three Raman data are needed namely, frequency of RBM mode, frequency of G- mode and one of the optical transition energies (for this case, E_{22}). All these data can be found from resonant Raman spectroscopy (RRS) of the unknown SWCNT. The value of G- shift against its diameter (calculated from its ω_{rbm}) need to put into the G- frequency vs d_t plot of Fig. 4.1 to identify the $(2n+m)$ family with which the data point is closest. Within acceptable experimental error margin in measuring ω_{rbm} and G- Raman shift and similar error margin in calculating d_t from ω_{rbm} due to different experimental environment, it is expected that the point will be near to its own $(2n+m)$ family or its closest neighboring family. It can be seen from both Fig. 4.1 and Fig. 4.2 that two neighboring $(2n+m)$ families have difference 1 and two families with difference more than 1 are relatively distant. Thus, within tolerable error margin, the choice is only limited to two neighboring families with whom the unknown SWCNT is closest. From these two options the precise $(2n+m)$ family belongs to the unknown SWCNT need to be confirmed. To confirm the family of unknown SWCNT, one needs to move to Fig. 4.2 and to put value of E_{22} against its diameter (calculated from its ω_{rbm}) to identify the $(2n+m)$ family in this plot with which this data point is closest now. Using the same previous argument, it can be said that within acceptable experimental error margin in measuring E_{22} , the point will be near to its own $(2n+m)$ family or its closest neighboring family. Now, the precise $(2n+m)$ family of the unknown SWCNT is determined as the one with which it is closest in both the plots.

Once the exact $(2n+m)$ family of the unknown SWCNT is confirmed, the next job is to use some calculation based on structural relation between diameter and Chiral index (n, m) of SWCNTs so as to find the value of n and m .

Let the true family of unknown SWCNT is, $2n+m = k$, i.e. $m=k-2n$, and it is known that, $d_t = \sqrt{3(n^2 + nm + m^2)} a_{cc} / \pi$, where, a_{cc} = C-C bond length = 0.142 nm. So, with $m=k-2n$, it can be written as, $3n^2 - 3kn + k^2 = 163.166d_t^2$

4.2.2 Assignment of chiral index (n, m) using the proposed method

If an specific case is taken, where experimental values are $\omega_{\text{rbm}}=216.4$ for which $d_t = 1.080426$, $E_{22}=1.58$ eV, and G- shift is 1557.4 cm^{-1} , then, after comparing two plots in Fig. 4.1 and Fig. 4.2, the precise family of the unknown SWCNT is found to be, $k=25$, then, $3n^2 - 75n + 434.6 = 0$; From this equation, one gets two values of n , where, $n_1=15.87$ and $n_2= 9.13$, and corresponding, $m_1=-6.75$ and $m_2= 6.75$. As n and m are always positive integer, So, taking the nearest positive integer, the valid chirality is (9,7). Using same process, the chirality of 12 more SWCNTs can be found unambiguously and the result is summarized in Table 4.1.

These results were compared with the results of H. Telg et al. [141] and it was found that all the chiral assignments are correct. This proves the strength and accuracy of proposed method. Thus, using this technique chiral index (n,m) of any unknown SWCNT can be found from Raman data. One fundamental advantages of proposed method over all previous methods is, this technique works well for both isolated and bundled SWCNTs whereas other techniques are applicable only for bundled SWCNTs using pattern regenerating from Kataura plot.

4.2.3 Characterizing SWCNTs and DWCNTs from higher optical transitions using the proposed empirical model

Section 4.2.1 and 4.2.2 demonstrated a new technique for assignment of chirality to unknown SWCNTs using E_{11} and E_{22} from the empirical model. The proposed empirical model can also estimate higher optical transitions (E_{33} to E_{77}) in semiconducting and metallic SWCNTs and hence can be used to validate characterization of SWCNTs and DWCNTs using their higher transitions. In fact, in many cases there is no option for characterizing SWCNTs except by using their higher transitions. For example, Rayleigh spectra over a photon energy range 1.2–2.7 eV is sensitive to the 2nd transition of metallic tubes and 3rd and 4th transitions

Table 4.1 Assignment of chiral index (n, m)

Calculated d_t (nm)	Predicted (2n+m) Family	n_1	n_2	m_1	m_2	Assigned (n, m)
1.0804264	25	15.87	9.13	- 6.75	6.75	(9,7)
1.0352832	25	14.99	10.01	- 4.98	4.98	(10,5)
1.0136364	23	14.93	8.07	- 6.86	6.86	(8,7)
0.9612069	23	13.98	9.02	- 4.96	4.96	(9,5)
0.9489362	22	13.94	8.06	- 5.87	5.87	(8,6)
0.902834	22	12.99	9.00	- 3.99	3.99	(9,4)
0.8814229	20	12.98	7.01	- 5.97	5.97	(7,6)
0.8745098	22	12.12	9.88	- 2.23	2.23	(10,2)
0.8259259	20	11.94	8.06	- 3.87	3.88	(8,4)
0.8189497	19	12.03	6.97	- 5.05	5.05	(7,5)
0.7745745	19	11.09	7.90	- 3.18	3.19	(8,3)
0.7443258	17	10.96	6.04	- 4.91	4.91	(6,5)
0.680916	16	9.97	6.03	- 3.93	3.94	(6,4)

of semiconducting tubes. For small diameter nanotubes, the 1st metallic transition may be observed, while the E_{55} transition may appear below 2.7 eV for semiconducting SWCNTs with $d > 2.5$ nm.

Table 4.2 Reported chirality assignment of CNTs [132, 133, 137]
and validation from proposed empirical model

Measured [132, 133, 137] /Empirical	E_{11}	E_{22}	E_{33}	E_{44}	Assigned Chiral index
Rayleigh/ Raman [132]		1.98			(19,19) or (20,20)
Empirical		2.1			(19,19)
Empirical		2.02			(20,20)
Rayleigh/ Raman [132]			2.25	2.33	(20,3) or (21,1)
Empirical			2.25	2.34	(20,3)
Empirical			2.275	2.28	(21,1)
Rayleigh [133]			1.9	2.1	(26,0) or (25,2)
Empirical			1.921	1.974	(26,0)
Empirical			1.91	2.016	(25,2)
PL [137]	1.128	2.21			(8,4)
Empirical	1.12	2.1	2.14		(8,4)@(18,2) DWCNT
PL [137]	0.828	1.6			(10,6)
Empirical	0.9	1.64			(10,6)
PL [137]	0.793	1.54			(14,1)
Empirical	0.83	1.63	2.5		(14,1)

Semiconducting and metallic SWCNTs and DWCNTs have been characterized using their higher optical transitions $E_{22}(M)$, $E_{33}(S)$, $E_{44}(S)$ and $E_{55}(S)$. Here, some of those reports [132,

133, 137] are used to validate the estimated higher transitions from proposed empirical model. Table 4.2 gives their assignment along with the estimation from the proposed empirical model for those CNTs. It can be noted from Table 4.2 that in all observed cases, proposed empirical model can faithfully made the same chirality assignment made by the authors from their observations. These results confirm the validity of chirality assignments made by the authors and at the same time validates the accuracy of the empirical model.

4.3 Using Proposed Empirical Model for Describing Emission Spectra of CNT Based LEDs

In this section, few experimental reports on emission spectra measured from SWCNT based LEDs are presented and the observations are compared and explained with the help of proposed empirical model.

Wang *et al.* [144] carried out electroluminescence (EL) measurements on a two-terminal carbon nanotube (CNT) based light-emitting diode (LED). They determined the diameter of the CNT to be 1.14 nm and observed EL spectrum with clear emission peak at 0.925 eV which was identified as that resulting from the excitonic state of a (12, 4) SWCNT. From proposed empirical equation, the estimated value of E_{11} for (12, 4) SWCNT with diameter 1.14 nm is 0.92 eV which is strikingly close with the observed emission peak. Thus, the experimental observation by Wang *et al.* [144] from SWCNT based LED validates proposed estimation. Also, by correlating the E_{11} with the chiral index (12, 4), this result clearly proves that proposed equation can precisely identify the SWCNT used in single chirality nanotube device.

Mueller *et al.* [145] obtained the maximum of the spectral intensity distribution at $E_{11} \sim 0.635$ eV from electroluminescence measurements of their p-n diode in the ambipolar regime. They also presented the results obtained from the same device with different SWCNT where the dominant emission was found to be 0.755 eV. From resonance Raman spectroscopy and atomic force microscopy (AFM), the nanotube diameter was determined to be 1.41 nm and 1.24 nm, respectively in devices with two different SWCNTs. The empirical calculation gives an E_{11} -energy of around 0.7 eV for a ~ 1.41 nm diameter which corresponds to (16, 3)

SWCNT and around 0.8 eV for a 1.24 nm diameter which corresponds to (10, 8) SWCNT. Thus, the empirical result suggests that they used (16, 3) and (10, 8) SWCNTs, respectively, in their two devices though they did not characterize the chirality of those SWCNTs. This finding not only validates the empirical prediction but also helps to reproduce such experimental results by using (16, 3) and (10, 8) tubes, respectively.

Yu *et al.* [146] reported the fabrication and performance characteristics of light-emitting devices that use serpentine CNTs, having multiple parallel CNT channels of identical chirality, grown directly on quartz. Two emission peaks were identified from their CNT-based LED where the lower energy emission peak was at 0.85 eV. From atomic force microscopy (AFM), the diameter of the nanotube was estimated to be 1.1 ± 0.2 nm. The emission peak was identified as the E_{11} excitonic transition of the CNT. The empirical calculation gives an E_{11} -energy around 0.84 eV for a 1.17 nm diameter tube which corresponds to (13, 3) SWCNT and around 0.88 eV for a 1.18 nm diameter tube which corresponds to (11, 6) SWCNT. Thus, empirical result suggests that they used either (13, 3) or (11,6) SWCNT in their devices though they did not characterize the chirality of those SWCNTs.

Pfeiffer *et al.* [147] measured the electroluminescence and photoluminescence of (9, 7)-semi-conducting carbon nanotube devices and demonstrate that the electroluminescence wavelength is determined by the nanotube's chiral index (n, m). They assigned the 825 nm peaks to the excitonic E_{22} K-point interband transition by comparison of the electroluminescence spectra with corresponding photoluminescence excitation maps. From proposed empirical equation, the estimated value of E_{22} for (9, 7) SWCNT with diameter 1.1 nm is 1.566 eV which is very close to the observed emission peak at 1.5 eV (825 nm). Thus, the experimental observation by Pfeiffer *et al.* validates proposed estimation. Also, this result clearly proves, by correlating the E_{22} with the chiral index (9, 7), the proposed equation can precisely identify the SWCNT used in that experiment.

Vijayaraghavan *et al.* [148] adopted a combination of single chirality nanotube suspensions made by chirality-selective polymer wrapping with ultra-large scale directed assembly by

dielectrophoresis as the route to fabricating high-density arrays of individual, single chirality nanotube devices. The characteristic bright-exciton (BE) PL emission of a (9,7) nanotube, at 1345 nm was seen which corresponds to E_{11} . From proposed empirical equation, the estimated value of E_{11} for (9, 7) SWCNT with diameter 1.1 nm is 0.922 eV which is exactly equal to the observed emission peak at 0.922eV (1345 nm). Thus, the experimental observation by Vijayaraghavan *et al.* [148] in their device validates the estimation. Also, this result clearly proves, by correlating the E_{11} with the chiral index (9, 7), the proposed equation can precisely identify the SWCNT used in single chirality nanotube device.

Graf *et al.* [134] demonstrated the first near-infrared (nIR) organic LED based on single-walled carbon nanotubes as the emitter. A bare film of the purified material shows the characteristic absorption and photoluminescence (PL) spectrum of (6,5) SWCNTs with an emission peak at 1010 nm (corresponds to 1.228 eV), associated with excitonic emission from (6,5) SWCNTs. From the empirical equation, the estimated value of E_{11} for (6, 5) SWCNT is 1.235 eV which is very close to the observed emission peak at 1010 nm (1.228 eV). Thus, the experimental observation by Graf *et al.* [134] validates the estimation.

4.4 Empirical Calculation of Optical Transitions for Perpendicular Polarization of Light

The polarization of light absorbed, emitted, or scattered by an object can reveal information not otherwise available optically, e.g., the axis of symmetry of an unresolved emitter. Thus, polarization provides a handle on understanding the structures key for manipulating and controlling electromagnetic fields at the nanoscale. SWCNTs are extremely anisotropic which leads to significantly differing polarizabilities for external fields applied parallel and perpendicular to the tube axis. Therefore, light polarization can be used as an external parameter for tuning the optical properties of nanotube-based optoelectronic devices. This is of importance since, in this case, internal changes to the device will not be needed, and the orientation of the device with respect to the incident light can modify the wavelength of absorption or emission.

This is already discussed under section 2.1 that interband optical transitions between the massless, linear bands are not allowed for any light polarization due to symmetry. The perpendicular-polarized absorption has been considered to be strongly suppressed due to the induced self-consistent local field depolarization effect. However, weak but distinct peaks have been observed in some photoluminescence experiments of individual single-walled nanotubes (SWNTs) under the perpendicular polarization and its peak position is shifted to the higher energy side [31, 32].

K. Liu *et al.* [34] demonstrated high-sensitivity absorption spectroscopy for 57 individual chirality-defined SWCNTs over broad spectral range and showed that although transitions between adjacent cutting lines are symmetry allowed, their matrix elements are always zero close to the band gap, except for the E_{12} and E_{21} transitions. This matrix element effect strongly suppresses exciton transition (as well as van Hove singularity at the band edge), resulting in no spectral resonances for higher-order transitions under perpendicularly polarized light. Thus, when considering optical transitions due to perpendicular polarization,

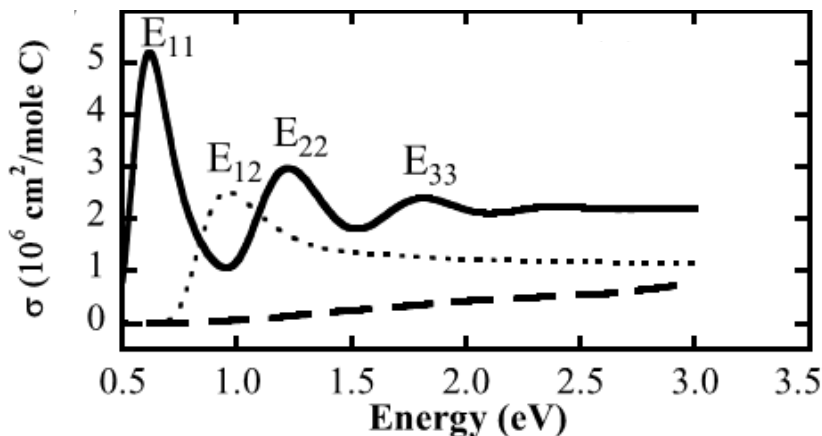


Figure 4.3: Calculated nanotube absorption cross sections for parallel (solid line) and perpendicular with (dashed line) and without (dotted line) a depolarization correction [30].

only the E_{12} and E_{21} transitions are worth to be discussed and not E_{13} and E_{24} etc, as they are forbidden. Indeed, prominent absorption peak corresponding to E_{12} and E_{21} transitions in semiconducting SWCNTs have been observed before by other research groups with perpendicular polarization excitation [31, 32]. Grüneis *et al.* [21] neglected both the trigonal

warping effect and the electron–hole asymmetry in their calculation and used the following simplification, $E_{12}^S = 0.5(E_{22}^S + E_{11}^S)$. However, several analytical and experimental works [25, 27, 30-32] reported the obvious depolarization effect, such as the lower intensity compared with the longitudinal situations and the blue shift of excitation peaks for E_{12} . Uryu *et al.* [22, 23] calculated it to be closer to that associated with that of the second gap for light polarized parallel to the axis. Islam *et al.* [30] and H. Liu *et al.* [27] calculated E_{12} peak for incident light polarized perpendicular to the tube axis and found it very close to the longitudinal excitonic peak E_{22} , as shown in Fig. 4.3, which is in good agreement with the experimental data [30-32]. Miyauchi *et al.* [31] performed anisotropic photoluminescence excitation (PLE) measurements on SWNTs in aqueous suspension for the UV-VIS-NIR range and observed distinct absorption peaks of several isolated SWNTs for the polarization perpendicular to the SWNT axis and the measured transition energies E_{12}^S were blueshifted from $(E_{22}^S + E_{11}^S)/2$ which was the qualitative values predicted within a single-particle theory without considering excitonic effects. Lefebvre *et al.* [32] reported polarized photoluminescence excitation spectra of twenty-five single-walled carbon nanotube species and identified several transverse excitations (polarization perpendicular to the SWNT axis) with greatly reduced absorption intensity. Their experimental E_{12} values deviate from the simpler predictions $E_{12} = 0.5(E_{22} + E_{11})$ and are closer to $0.8E_{22} + 0.2E_{11}$. Using $E_{12} = (1-x)E_{22} + xE_{11}$, they found that x ranges from 0 and 0.25.

Thus, all these indicate that E_{12} and E_{21} optical transitions due to perpendicular polarization can be calculated from E_{11} and E_{22} using the relation derived in earlier reports [25, 27, 31, 32]. As the empirical relations developed in chapter-3 can estimate E_{11} and E_{22} with good accuracy, thus it can also estimate the empirical value of optical transitions E_{12} and E_{21} for perpendicular polarization using the theoretically calculated as well as experimentally measured relation of E_{12} and E_{21} with E_{11} and E_{22} . Therefore, the empirical relations are not only capable for estimating optical transitions for polarization of incident light parallel to nanotube axis but also can be easily extended for estimating optical transitions for polarization of incident light perpendicular to nanotube axis.

4.5 Selection of SWCNTs in CNT Based LEDs for Visible and NIR Spectrum Using the Empirical Model

4.5.1 SWCNTs for emitting light in visible spectrum

Different SWCNTs exhibit different optical transitions based on their chirality. Chirality specific optical transitions can be estimated from the empirical models. For visible light emission from a SWCNT based LED, a number of SWCNTs can be identified from the empirical estimation. For LED emission, mainly the information on first optical transition energy is required. Table 4.3 shows the wavelength, frequency and photon energy of

Table 4.3 SWCNTs for emitting light in visible spectrum

Color	Wavelength (nm)	Frequency (THz)	Photon energy (eV)	Potential SWCNT with E_{11} (eV)
violet	380–450	670–790	2.75–3.26	
blue	450–485	620–670	2.56–2.75	
cyan	485–500	600–620	2.48–2.56	
green	500–565	530–600	2.19–2.48	(5,0) → 2.44 eV
yellow	565–590	510–530	2.10–2.19	
orange	590–625	480–510	1.98–2.10	(4,2) → 2.03 eV
Red	625–750	400–480	1.65–1.98	(5,3) → 1.72 eV (4,3) → 1.70 eV (6,1) → 1.85 eV

different lights in visible spectrum and corresponding SWCNTs that can be used in LED for emission of a particular color of light. It needs to mention here that, according to experimental reports, small radius SWCNTs having diameter below that of a (4, 2) tube tend to be metallic (instead of showing higher bandgap for smaller diameter) due to very high curvature effect in those tubes. As a result, no SWCNTs can be offered for emitting the blue color. Thus, white light emission directly from SWCNT-only LEDs won't be possible.

4.5.2 SWCNTs for Emitting Light in CIR (Color Infrared) Spectrum

For emission in CIR spectrum (section 2.6.3) using SWCNTs, a number of SWCNTs can be identified from the empirical estimation. Table 4.3 shows the wavelength, frequency and photon energy of different lights in CIR spectrum and corresponding SWCNTs that can be used in the emission process.

Table 4.4 SWCNTs for emitting light in CIR spectrum

Color	Wavelength (nm)	Photon energy (eV)	Potential SWCNT with E_{II} (eV)
Green to Red (visible light)	500-700	1.77-2.48	(6,1) →1.85 eV (4,2) →2.03 eV (5,0)→2.44 eV
NIR (Near Infrared)	700-900	1.38-1.77	(5,4) →1.43 eV (6,2) →1.45 eV (7,2) →1.51 eV (8,0) →1.59 eV (5,3) →1.62 eV (4,3) →1.70 eV

It can be observed from the table that SWCNT-alone CIR emission device is possible as the full CIR spectrum can be covered by using optical transitions from different SWCNTs.

4.6 Conclusions

In this chapter, few promising applications of the proposed empirical models are presented. An improved technique for chirality assignment of SWCNTs is demonstrated which work for both isolated and bundles SWCNTs. Using three Raman data namely, frequency of RBM mode, frequency of G- mode and one of the optical transition energies of an unknown SWCNT, its chiral index (n, m) can be determined even for an isolated SWCNT. The technique exploits the $(2n+m)$ family pattern both in optical transitions vs diameter plot (which can be found from the empirical model) and Raman G- mode frequency vs diameter plot of SWCNTs. Using two different plots can give accurate value of the $(2n+m)$ family which can be used to determine the chiral index (n,m) of unknown SWCNT unambiguously in most of the cases by solving basic structural relation between diameter and chiral index (n,m). Unlike existing methods, graphical comparison or pattern recognition with an existing Kataura plot is not required here. Validity of assigned chirality is cross checked from previous experimental reports. The technique is especially useful for determining chirality of isolated SWCNT.

Furthermore, the proposed empirical model can be used to estimate the E_{12} and E_{21} optical transitions in SWCNTs for perpendicular polarization of light, which comes from corresponding first and second optical transitions (E_{11} and E_{22}) for parallel polarization. The proposed empirical model also helps explaining the emission spectra observed from different SWCNT based LEDs. When the estimated optical transition matches with experimentally measured spectra, this also independently validates the accuracy of the prediction from the empirical models. Finally, the proposed empirical model also helps identifying suitable SWCNTs to be used in CNT devices for emitting light in visible (400-700 nm) or CIR (500-900 nm) spectrum.

CHAPTER-5

MANY BODY CORRECTIONS FOR HIGHER OPTICAL TRANSITIONS IN SEMICONDUCTING SWCNT

5.1 Excitons in SWCNTs

The optical properties of semiconducting carbon nanotubes are intrinsically important for potential applications in photonics and also provide insight into their structural and electrical properties [149]. As discussed in previous chapters, early optical spectra in SWCNTs had been interpreted in terms of free electron–hole carriers. Indeed, the electronic structure of SWCNTs, predicted by tight-binding Hamiltonian models, provides equally spaced subbands of valence and conduction bands with diverging density of states at the edges, known as van Hove singularities, which result from one-dimensional (1D) confinement conditions [150]. Most of the experimental results have been discussed and analyzed in terms of these inter-band transitions and associates the observed optical transitions with van Hove resonances.

However, a number of theoretical calculations of the optical spectra [151-165] and recent experiments [166-177] suggest that the observed transitions correspond to exciton energies, not interband transitions. In chapter two, this reality was skipped by developing an empirical model that incorporated suitable arrangement of chiral and empirical parameters for directly estimating the final optical transition energies in SWCNTs without considering the components that contributed to make such optical transitions. In this chapter, a semi-empirical approach will be taken to treat this reality separately in order to consider excitonic effects in optical transitions of SWCNTs.

The exciton binding energies in nanotubes have been predicted and are found to be large, as great as several hundred meVs, and reported to depend inversely on nanotube diameter [178, 179]. In bulk three-dimensional semiconductors the exciton binding energy is small, whereas in confined structures it is much bigger. The optical properties of semiconducting single-

walled CNTs (SWCNTs) are governed by excitons because of the large exciton binding energy. Experimentally it has been shown that for a (6,5) SWCNT with a diameter of 0.76 nm the exciton binding energy is roughly 0.42 eV, which is a significant fraction of the band gap of the CNT. The exciton binding energy (E_b) for a CNT with $d = 1.1$ nm and embedded in SiO₂/PMMA dielectric is about 0.2–0.3 eV. Indeed, when band gaps are optically probed the recorded energies account not only for the electronic band gaps but also for the exciton binding energies. The electronic band gaps could in principle be obtained just by subtracting the exciton energies but these cannot be easily measured [178, 179].

Due to this excitonic effect, the band gaps computed by authors are generally underestimated significantly. The exciton binding energies can be significant for the nanotubes with smaller diameters. Improved estimates of band gaps of few selected SWNTs have also been reported using GW approximation wherein many-body self-energy operator is expressed as the product between electronic Green's function (G) and the screened Coulomb interaction (W). Though GW scheme usually provides band gap estimates with good accuracy, the method is hugely expensive computationally. Furthermore, care in calculations is required in order to obtain converged results [178].

The experimental measurement of the electronic band gaps of CNTs are generally nontrivial and challenging as the observed optical band gap energies include contributions of exciton binding energies. Thus, theoretical models are required to estimate exciton energies since direct measurements of these energies are generally difficult.

5.2 Effect of Excitons on Optical Transitions in SWCNTs

An exciton is a bound pair of a photoexcited electron (e) and a hole (h). In conventional semiconductors, an exciton exists only at low temperature, below 10⁰ K. Since the exciton binding energy for a SWCNT is very large (up to 1 eV) due to their quasi-one-dimensional nature, an exciton can exist even at room temperature [151, 152, 157, 160]. Recent transient spectroscopy and nonlinear absorption have unambiguously revealed that the photophysics of SWCNTs is dominated by strongly bound excitons rather than free particles [150].

In particular, the optical transition energies of semiconducting nanotubes, along with their dependence on the nanotube diameter and chiral angle, have been studied in a number of fluorescence and Raman spectroscopy experiments [157]. Several observations from those experiments have attracted attention. First, optical gaps in SWCNTs are greater than those predicted from the tight binding (TB) model. Second, the ratio of the threshold energy corresponding to the second optical transition polarized along the SWCNT axis to that of the first such transition is less than the value 2 predicted within the TB model for wide SWCNTs [153]. Kane and Mele [153-155] pointed out that this ‘‘ratio problem’’ is a signature of electron-electron interactions [160]. More elaborate tight-binding calculation including orbital overlap and interactions beyond nearest neighbours partly account for the observed dependence of optical spectra on chirality. Though some aspects of the experiments can be interpreted within the context of a simple, noninteracting electron model, it is now established [157] from both theoretical calculations [151-165] and experimental measurements [166-177] that a simple band-structure calculation is insufficient for an accurate description of optical transition energies in SWCNTs. This is due to the omission of two highly important effects in low-dimensional semiconductors; (i) quasi-particle corrections to the simple band-structure and (ii) exciton effects. Both quasi-particle and exciton shifts are due to screened Coulomb interactions. The former describes the repulsive energy needed to add an additional electron to the system and, hence, raises the energy of the conduction band or, equivalently, increases the band gap. In contrast, the exciton shift describes the attractive Coulomb interaction between electrons and holes, which lowers the excitation energy. The experimental results [167, 168] demonstrate that, in fact, the overall effect is a blue-shift so that the positive quasi-particle correction actually dominates over the negative exciton binding energy [157].

Starting from the pioneering study by Ando [151] a large amount of theoretical and experimental works has confirmed strong excitonic effects in SWCNTs. Ando [151] originally predicted that the many-body interactions would shift the band gaps of semiconducting SWCNTs to higher energies and create excitons with significant electron-hole binding energy in the excited electronic state. Such strong many-body interactions are

supported by further theoretical work [152-165] and several recent experiments [166-177, 180, 181]. Dukovic *et al.* [172] has shown experimentally that for a (6,5) SWCNT with a diameter of 0.76 nm, the exciton binding energy is roughly 0.42 eV, which is a significant fraction (around 33%) of the band gap. This is about one hundred times larger than that for bulk semiconductors, but comparable to other 1D materials. Thus, excitonic effects cannot be largely neglected or treated as a small perturbation to the bandgap of SWCNTs as it was assumed in earlier studies [150]. Such result also suggests that excitonic effects dominate absorption and emission spectra and hence, all aspects of the optical properties of carbon nanotubes; optical absorption, fluorescence, Raman, and Rayleigh scattering of SWCNTs [172].

Current understanding of the photophysical properties of semiconducting carbon nanotubes are based mostly on experimental results for the first (E_{11}) and second (E_{22}) optical transitions in a small diameter range. Recently, third and fourth optical transitions (E_{33} and E_{44}) of semiconducting SWCNTs also gained some theoretical and experimental attention [174-177, 180, 181]. The results of Araujo *et al.* [176] have produced new physical insight into the behavior of the higher lying transitions in carbon nanotubes, with these results ultimately demonstrating that the E_{33} and E_{44} transitions cannot be described by simple extensions of E_{11} and E_{22} patterns. In fact, higher optical transitions are important for the optics of large diameter semiconducting SWCNTs, since for $d_t > 1.3$ nm, E_{22} is already in the infrared range. From a fundamental standpoint, expanded studies of the higher energy regions are necessary for developing a more complete understanding of the underlying electronic structure at higher energies.

The objective of this chapter is to review the nature of many body effect in first four optical transitions and then to devise a semi-empirical equation that can give complete description of experimentally observed values of next three higher optical transitions i.e. 5th, 6th and 7th transitions of semiconducting SWCNTs under the many body electronic picture. The many body effect on these three transitions will be revealed partially through this approach.

5.3 Developing Semi-empirical Model for Many Body Correction in SWCNTs

The transition energies for parallel polarization to a semiconducting SWCNT are denoted by E_{ii} ($i= 1, 2, 3, 4, \dots$) for a transition between i -th conduction (an electron) and i -th valence (a hole) energy bands [42]. Originally E_{ii} denoted a van Hove singular energy for the joint density of states for the one-particle energy bands of a SWCNT. Here same notation will be used for the transition energies of the exciton [159].

For a better description of the electronic structure within the tight binding method one has to consider an extended tight-binding model that considers the effects of chirality and curvature, plus the blue-shift correction due to many-body effects. The transition energy of a SWCNT can be considered as the sum of a one-particle energy and a many-body energy which is further decomposed into an exciton binding energy and a self-energy. The one particle energy is calculated by the energy difference between the i -th conduction and the i -th valence energy bands. The exciton binding energy and self energy are the Coulomb interaction for a photo-excited electron with a hole and with other electrons in the valence energy bands, respectively [159]. The latter interaction increases the energy of the electron (decreases the energy of a hole), and this interaction thus contributes to the increase in the energy gap compared with the single-particle energy difference between an electron and a hole. This energy difference is called the self-energy. The exciton excitation energy is thus given by (single-particle energy) + (self-energy) – (exciton binding energy) \equiv (quasi-particle energy) – (exciton binding energy). Here, (self-energy) – (exciton binding energy) is the many-body effect.

Earlier pioneering work by Kane and Mele [154] predicted that both electron–electron and electron–hole long range one-dimensional coulomb interactions (with length scales larger than tube circumference) strongly depend on the inverse tube diameter, competing and nearly cancelling each other [153, 154, 158, 159]. As a result of this cancellation, the observed optical transitions in carbon nanotubes are dominated by short range two-dimensional graphene self-energy effects, leading to a logarithmic correction to the electronic self-energy

of the first (E_{11}) and second (E_{22}) related levels [154, 177], commonly known as KM correction in literatures [158, 165, 175, 180] as given by,

$$\Delta E = 0.55 \frac{2p}{3d} \log\left(\frac{3}{2p/3d}\right) \quad (5.1)$$

Where, $p=1, 2, 4, 5, 7, 8$ with $i=1, 2, 3, 4, 5, 6$, respectively, for 1st, 2nd, 3rd, 4th, 5th and 6th optical transitions (E_{ii}) of semi-conducting SWCNTs.

The ability of KM correction, given by Eqn. (5.1), to fit first and second optical transitions (E_{11} and E_{22}) of semiconducting SWCNTs is already proven [165, 175]. The many-body correction to E_{11} and E_{22} energies is reported to be around 0.2 eV, while the correction to E_{33} and E_{44} energies can be 0.6 eV [158, 159, 165]. These results have shown that the nonlinear scaling laws can be used as an accurate basis for calculating Kataura plots useful for identifying spectral features at these higher energies [180]. Moreover, the many-body correction does not contribute to the family spread in E_{11} and E_{22} in the Kataura plot, while it contributes significantly to the family spread in E_{33} and E_{44} [158, 159, 180]. Experimental values of third and fourth optical transitions (E_{33} and E_{44}) of semiconducting SWCNTs are found to deviate from same scaling law and the deviation from the extended tight binding method can be successfully fit by summing a $\Delta E \approx 0.3/d_t$ dependence to the above many-body logarithmic corrections [174-177]. The E_{33} and E_{44} are, therefore, blue-shifted from the excitonic scaling law, and the blueshift goes with inverse diameter, like the exciton binding energy whose value is found to be similar like earlier experiment [172]. Authors [174-177, 180, 181] interpreted this result as weaker (or even null) exciton binding energy for E_{33} and E_{44} transitions when compared to the lower lying levels.

However, so far there is no significant report that revealed the nature of many body corrections for fifth, sixth or higher optical transitions in semiconducting SWCNTs. Here, KM correction term will be used to fit experimentally reported higher optical transitions, E_{55} , E_{66} and E_{77} of semiconducting SWCNTs to reveal the excitonic picture in these transitions.

As a first approximation, considering the linear dispersion of the graphene and wave vector quantization, the optical transition energies in carbon nanotubes are given by, $E_{ii} = (4p/3d_i)$

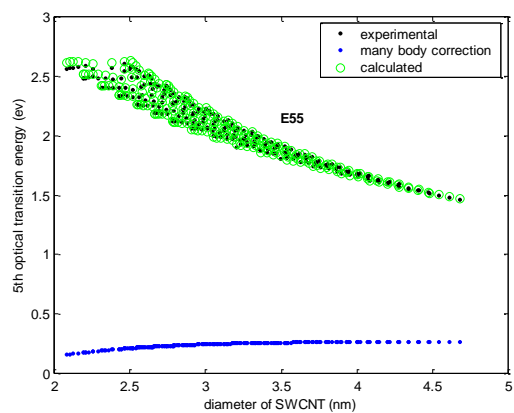
$\times \hbar v_F$, where, \hbar is plank's constant ($=6.582 \times 10^{-16} \text{eV.s}$) and $v_F = 9.3 \times 10^5 \text{ m/s}$, is the Fermi velocity in semiconducting SWCNT [182] and $p = 1, 2, 4, 5, 7, 8$ for E_{ii} with $i=1, 2, 3, 4, 5, 6$, respectively [39, 42, 176, 177, 180, 182, 183]. The resultant approximation is $E_{ii} \approx p(0.8/d_i)$ [182,183]. The E_{ii} values also exhibit a dependence on the nanotube's curvature and chirality which can be expressed by a term $\text{Cos}(3\theta)/d^2$ comprising diameter and chiral angle to account for curvature effect and chirality effect, respectively [16, 39, 180, 184-191]. Finally, to complete the picture, many body correction to optical transitions needs to be added as derived by Kane and Mele [153, 154, 158, 159, 165]. The complete equation is represented by Eqn (2) along with two fitting parameters A and B.

$$E_{ii} = \frac{A(\approx 0.8p)}{d} + B \frac{\text{Cos}3\theta}{d^2} + 0.55 \frac{2p}{3d} \log\left(\frac{9d}{2p}\right) \quad (5.2)$$

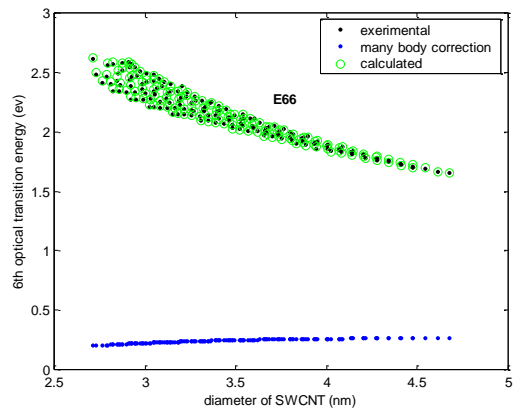
Equation (2) describes three higher optical transitions E_{55} , E_{66} and E_{77} , for $p = 7, 8$ and 10 , respectively, where, first term of the equation carries the linear dependence of E_{ii} on p/d_i expected from quantum confinement of the 2D electronic structure of graphene, second term accounts for curvature and chirality dependence of optical transitions and the third term stands for many-body logarithmic corrections. The number of samples for each mod type and best fit of the fitting parameters A and B to the reported experimental data for E_{55} , E_{66} and E_{77} are given in Table 5.1. In fact, the value of A is expected to be close to $0.8p$ as shown earlier which is reflected from the values of A for three transitions given in Table 4.1. Hence, mainly B is the only fitting parameter and it can be observed that it takes opposite sign for mod 1 and mod 2 type semiconducting SWCNTs and this alters with odd and even transitions. It was observed that, with these fitting parameters, the calculated values for 5th, 6th and 7th optical transitions in semiconducting SWCNTs excellently match with experimentally reported values over the full diameter range. The average absolute error for all three transitions is below 10 meV and the corresponding %average absolute error was found to be less than 0.5%. The error in each transition rapidly decreases further for higher diameter SWCNTs, as expected from the theory.

Table 5.1 Fitting parameters in Eqn (5.2) for 5th, 6th and 7th optical transitions of semiconducting SWCNTs

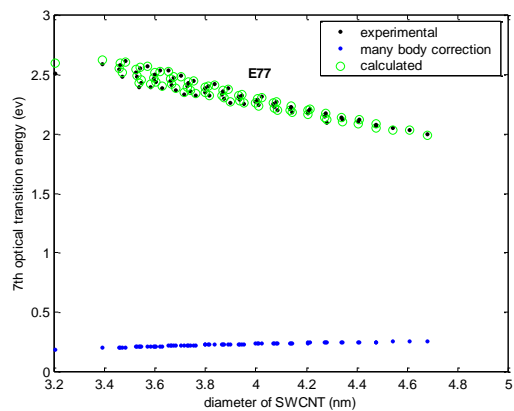
E_{ii}	p	Mod	Total Samples	A $\approx 0.8p$	B	Average Error	% Error
E_{55}	7	1	137	5.63	-1.1	0.01	0.47%
		2	109	5.63	1.1	.008	0.35%
E_{66}	8	1	82	6.5	1.2	.008	0.36%
		2	77	6.45	-1.4	.008	0.39%
E_{77}	10	1	37	8.12	-1.6	.012	0.54%
		2	33	8.2	1.6	.007	0.29%



(a)



(b)



(c)

Figure 5.1: Experimental value (black dot), calculated value from this work (green triangle) and many-body correction (blue dot) of 5th, 6th and 7th optical transitions in (a), (b) and (c), respectively, plotted vs diameter of semiconducting SWCNTs.

Figure 5.5 (a), (b) and (c) show the plot of experimental data as well as values calculated in this work for 5th, 6th and 7th optical transitions, respectively, along with their many body corrections against their diameters. It can be observed from these three plots that, for all three optical transitions, calculated values predicted by Eqn. (5.2) are almost inseparably too close to the experimental values over the full diameter range under consideration.

As many body correction in the single particle electronic picture of semiconducting SWCNT almost accurately reproduce experimental result of these three optical transitions, it indicates that, unlike 3rd and 4th optical transitions [174-177, 180, 181], Coulomb effect is significant in 5th, 6th and 7th transitions and must be considered for calculating these transitions. This also means, exciton binding energy is not negligible for these three transitions. Future experiments may reveal the validity of this conclusion by measuring the exciton binding energies of these three transitions. Nevertheless, this work can be taken as a guide to understand the optical process involved in these higher transitions of semiconducting SWCNTs. Future experiments are needed to through more light on this matter.

5.4 Conclusions

Due to their quasi-one-dimensional structure, electron-electron and electron-hole interaction and corresponding self-energy and exciton binding energy are important in SWCNTs. In this chapter, a brief review of Coulomb effect on determining optical transition energies of semiconducting single wall carbon nanotubes is presented. The difference between electron-electron and electron-hole energies gives many body effect and corresponding correction is called many body correction. Proposed correction by authors in the conventional single particle electronic picture of SWCNT to include many body effect in first four optical transitions has been discussed. Here, next three higher optical transitions of semiconducting SWCNTs namely, i.e. 5th, 6th and 7th transitions are investigated. Experimental values of these higher transitions are collected from recent experimental reports. A semi-empirical model is developed to explain those data by extending single-particle picture corrected for nanotube curvature and chirality effect along with many body corrections. The result shows

that these three transitions excellently follow the proposed corrected picture with less than 0.5% average absolute error. This result is an indirect proof that excitonic behavior is strong in 5th, 6th and 7th optical transitions of semiconducting SWCNTs unlike 3rd and 4th transitions as reported by earlier authors. This also suggests a significant value of exciton binding energies in these higher transitions. Future experimental measurements are expected to reveal such excitonic behaviour and their values in higher optical transitions of SWCNTs.

CHAPTER 6

EMPIRICAL MODELING OF INNER TUBE OPTICAL TRANSITIONS IN DOUBLE WALL CARBON NANOTUBES

As discussed in chapter-2, section 2.4, Double wall carbon nanotubes (DWCNTs) display four different configurations; S@S, S@M, M@S, and M@M, depending on the semiconducting (S) or metallic (M) type of the inner and outer SWNTs —where the notation is inner@outer wall [90, 91]. The chirality, average diameter and inter-wall distance of the DWCNT are important parameters when determining the electronic band structure. The most important parameter is the chirality of the constituent tubes, because the chiral index (n, m) determines to a greater degree the optical transitions of the constituent SWCNTs and overall DWCNT.

6.1 Zigzag@zigzag DWCNTs

For theoretical calculations or first principle based simulations, DWNTs made of two concentric zigzag type SWCNTs are preferred because of their structural symmetry and consequent computational advantages.

Using the general relation given in Chapter 1 (section 1.1.2), the average diameter and inter-wall distance of a DWCNT made of two concentric zigzag SWCNTs can be calculated as follows,

If d is nanotube diameter in nanometer, then, $d = a_0 \sqrt{(n^2 + nm + m^2)} / \pi$, where, $a_0 = \sqrt{3}a_{cc}$ ($a_{cc} = 1.42 \text{ \AA}$ is c-c bond length)

For, zigzag (n, 0) SWCNTs,

$$d = \frac{\sqrt{3}a_{cc}}{\pi} n$$

Now, for a DWNT with outer tube $(n_o, 0)$ and inner tube $(n_i, 0)$, having diameter d_o and d_i , respectively, average diameter of DWNT,

$$D = \frac{1}{2}(d_o + d_i) = \frac{\sqrt{3}a_{cc}}{2\pi}(n_o + n_i) = 0.03915(n_o + n_i), \text{ and inter-wall separation of}$$

$$\text{DWNT, } w = r_o - r_i = \frac{1}{2}(d_o - d_i) = \frac{\sqrt{3}a_{cc}}{2\pi}(n_o - n_i) = 0.03915(n_o - n_i).$$

Earlier calculations [92, 93] showed that the inter-wall distance between inner and outer tubes vary between 0.33 and 0.41 nm, with an ideal separation of 3.39 Å. Endo *et al.* [86] measured diameter distribution of highly purified DWCNTs using high-resolution TEM and found that they fall between 0.4 and 1.3 nm for inner tubes and 1.0 and 2.2 nm for outer tubes.

To keep w in between theoretically calculated and experimentally reported inter-wall separation, value of $(n_o - n_i)$ is limited to, $n_o - n_i = 8, 9, 10, 11$, that corresponds to inter-wall distance 0.313 nm, 0.352 nm, 0.392 nm and 0.431 nm, respectively. Based on this, following selection criteria have been derived for the constituent zigzag SWCNTs of possible zigzag@zigzag DWCNTs,

Table 6.1 Possible combinations of inner and outer tubes of zigzag@zigzag Double Wall Carbon Nanotubes

DWNT Type	Inner tube (n_i) and Outer tube (n_o)	Explanation	Constituent SWCNTs	
			n_i	n_o
m@s (metallic inner tube and semiconducting outer tube)	$n_i = 3k$ $n_o = 3k+8, 10, 11$ where, $n_o = 3k+10 \pmod{1}$ $= 3k+8, 11 \pmod{2}$	$n_o = 3k+9$ $= 3(k+3)$ is metallic	6	14, 16, 17
			9	17, 19, 20
			12	20, 22, 23
			15	23, 25, 26
s@s (Both inner and outer tubes are semiconducting)	$n_i = 3k+1 \pmod{1}$ $n_o = n_i + 9, 10$ where, $n_o = 3k+10 \pmod{1}$ $= 3k+11 \pmod{2}$	$n_o = n_i + 8, 11$ $= 3k+9, 3k+12$ are metallic	7	16, 17
			10	19, 20
			13	22, 23
			16	25, 26
	$n_i = 3k+2 \pmod{2}$ $n_o = n_i + 8, 9, 11$ where, $n_o = 3k+10, 13 \pmod{1}$ $= 3k+11 \pmod{2}$	$n_o = n_i + 10$ $= 3k+12$ is metallic	5	13, 14, 16
			8	16, 17, 19
			11	19, 20, 22
			14	22, 23, 25
			17	25, 26, 28

DWNT Type	Inner tube (n_i) and Outer tube (n_o)	Explanation	Constituent SWCNTs	
			n_i	n_o
s@m (semiconducting inner tube and metallic outer tube)	$n_i = 3k+1 \pmod{1}$ $n_o = n_i + 8, 11$	no= $n_i+9, 10$ $=3k+10, 3k+11$ are semiconducting	7	15, 18
			10	18, 21
			13	21, 24
			16	24, 27
	$n_i = 3k+2 \pmod{2}$ $n_o = n_i + 10$ only	no= $n_i + 8, 9, 11$ $=3k+10, 3k+11,$ $3k+13$ are semiconducting	5	15
			8	18
			11	21
			14	24
			17	27

6.2 Empirical Model for Optical Transitions of Inner Semiconducting tubes of DWCNTs

The selection criteria given in Table 6.1 is only for the DWNTs having two concentric zigzag type SWCNTs. But, in practice the constituent SWCNTs of a DWNT are not necessarily of zigzag types. In fact, most of the recent experiments [93-100] probed DWNTs that constitutes chiral type of SWCNTs. Combining electron diffraction (ED) and Raman/optical spectroscopy to examine individual DWNTs appeared to be the most direct and unambiguous method to address the relationship between their structure and physical properties [96].

In DWNTs, the inner tube possesses a special status, granted by the outer tube, which acts as a shield and protects effectively the inner tubes from perturbations, thus provides higher

mechanical, thermal, and chemical stability even in aggressive environments compared to SWNTs. Several experiments [93-100] performed on individual index-identified DWNTs demonstrated that the optical transitions of inner semiconducting tube (ISCT) of DWNTs can be significantly shifted compared to their SWNT constituent counterparts. It has been shown in previous studies of nanotubes in different environments that dielectric screening can lead to a redshift in optical transition energies [94]. This dielectric screening effect can account for an average redshift of optical transition energies observed in DWNTs, but it cannot explain the very large and strongly transition-dependent variations in optical transition shifts. So far, there is no reliable theoretical or empirical models to calculate the electronic band structure of DWNTs or the energy shifts in inner semiconducting tube of DWNTs. The reason might be due to the fact that, SWCNTs have been studied extensively for last three decades, both theoretically and experimentally, whereas, serious study on DWCNT has started only in last decade and as a result, there are still ambiguities regarding its exact electronic structure for different combinations of inner and outer tubes. Thus, an empirical model to estimate the experimentally observed shifts in optical transitions of inner semiconducting tubes in DWNTs would be useful.

For inner semiconducting tubes, only S@S and S@M DWCNTs are considered as the remaining two species of DWCNTs denoted by M@S and M@M contain metallic inner tubes. Now, for developing the empirical model, reported [93-100] trend of the red shifts of optical transition energies of inner semiconducting tubes of S@S and S@M DWCNTs were studied. Their optical transitions were found to be dependent on the average diameter, inter-wall distance as well as on the chirality and intrinsic properties of the constituent SWCNTs. In section 3.1.1 of chapter-3, the empirical model for the first seven optical transitions in semiconducting SWCNTs was already developed. Now, when these same SWCNTs become the inner tube of DWNTs, their optical transitions energy are significantly red shifted, as found from experiments [93-100], and the amount of shift varies with chirality. Following Table shows the reported experimental values of first five optical transitions of inner semiconducting tubes of DWNT with corresponding value in as isolated SWCNT of same chirality,

Table 6.2 Optical transitions in Inner Semiconducting Tubes (ISCT) of DWNTs and corresponding isolated SWCNTs of same chirality

ISCT Optical Transitions	DWNTs inner@outer	Optical transition energy (eV)	
		SWCNT (exp ^[39])	ISCT of DWNT (exp ^[94-98])
E_{11}^S (mod 1)	(8,4)@(18,2)	1.15	1.128 ^[96]
	(7,6)@(16,6)	1.13	1.058 ^[96]
	(10,6)@(14,13)	0.926	0.828 ^[96]
	(14,1)@(15,12)	0.869	0.792 ^[96]
E_{22}^S (mod 1)	(7,6)@(16,6)	1.926	1.82 ^[96]
	(10,6)@(14,13)	1.649	1.6 ^[96]
	(10,6)@(16,11)	1.649	1.6 ^[96]
	(14,1)@(15,12)	1.671	1.55 ^[96]
	(12,5)@(16,12)	1.57	1.5 ^[94]
E_{22}^S (mod 2)	(13,2)@(21,3)	1.46	1.39 ^[94]
	(12,4)@(16,11)	1.46	1.38 ^[94]
	(13,5)@(23,3)	1.35	1.28 ^[94]
E_{33}^S (mod 1)	(12,5)@(16,12)	2.26	2.44 ^[94]
	(12,8)@(25,2)	2.03	2.3 ^[94]
	(17,1)@(16,14)	2.55	2.13 ^[94]
	(18,5)@(20,14)	2.41	1.94 ^[94]
	(18,5)@(27,5)	2.02	1.905 ^[94]
	(16,9)@(24,10)	1.76	1.92 ^[94]
	(16,12)@(27,10)	2.03	1.81 ^[95,98]
	(23,4)@(22,18)	1.76	1.68 ^[97]
	(16,15)@(23,18)	1.88	1.66 ^[94]

ISCT Optical Transitions	DWNTs inner@outer	Optical transition energy (eV)	
		SWCNT (exp ^[39])	ISCT of DWNT (exp ^[94-98])
E_{33}^S (mod 2)	(13,8)@(16,15)	2.29	2.28 ^[94]
	(15,7)@(20,12)	2.67	2.24 ^[94]
	(14,9)@(17,16)	2.38	2.11 ^[94]
	(15,10)@(27,6)	2.13	2.02 ^[94]
	(19,8)@(21,18)	2.01	1.96 ^[94]
	(15,13)@(21,17)	1.94	1.9 ^[97]
E_{44}^S (mod 1)	(16,9)@(24,10)	2.58	2.39 ^[94]
	(16,12)@(27,10)	2.34	2.15 ^[95,98]
	(16,15)@(23,18)	2.13	2.09 ^[94]
E_{44}^S (mod 2)	(15,7)@(20,12)	2.58	2.42 ^[94]
	(15,10)@(27,6)	2.41	2.28 ^[94]
	(19,8)@(21,18)	2.2	2.15 ^[94]
	(15,13)@(21,17)	2.28	2.21 ^[97]
E_{55}^S (mod 1)	(16,12)@(27,10)	2.9	2.75 ^[95,98]

In Table 6.2, optical transitions are grouped according to the mod value of inner semiconducting tubes and it was already showed in Chapter-3 that optical transitions in semiconducting SWCNTs vary with mod values for comparable diameters. As first seven optical transitions in semiconducting SWCNTs has already been modeled in chapter-3, so we can use the same model for representing the optical transitions in ISCTs of DWNTs with necessary modification of relevant parameters.

The proposed model for isolated SWCNT used a $1/d$ term to represent the basic inverse relation of optical transitions with diameter and then an exponential term with two specific

chiral indices combinations $(n+2m)$ and $(2n-m)$ along with an additional d term to incorporate curvature effect. In case of optical transitions of ISCTs of DWNTs, similar decreasing trend of the optical transitions was observed with respect to D , average diameter of DWNTs. This suggests us to replace $1/d$ term of SWCNT model by $1/D$ for DWNTs. In the proposed model of optical transitions of ISCTs of DWNTs, inner tube diameter (d_i), chiral indices combinations (n_i+2m_i) and $(2n_i-m_i)$ are kept same as before to include the curvature effect and chirality specific behavior of inner semiconducting tube. The effect of outer tube is now included by the inclusion of D term which comes from the chirality of both inner and outer tubes. Thus, if $1/d$ of SWCNT model is replaced by $1/D$ (average diameter of DWNT) and the numerical fitting parameters are readjusted then it can faithfully reproduce all experimentally observed red shifted optical transitions of ISCTs of S@M and S@S DWNTs.

Following are the two resultant general empirical relation that relates first five optical transitions of ISCTs of DWNTs with diameter and chiral indices of inner tubes and average diameter of DWNTs. For mod 1 type odd transitions ($E_{11}^S, E_{33}^S, E_{55}^S$) and mod 2 type even transitions ($E_{22}^S, E_{44}^S, E_{66}^S$),

$$E_{ii} = \frac{A}{D} \exp\left(\frac{d - B}{n + 2m}\right) \quad (6.1)$$

For mod 2 type odd transitions ($E_{11}^S, E_{33}^S, E_{55}^S, E_{77}^S$) and mod 1 type even transitions ($E_{22}^S, E_{44}^S, E_{66}^S$),

$$E_{ii} = \frac{A}{D} \exp\left(\frac{d - B}{2n - m}\right) \quad (6.2)$$

Here, only the values of A and B are different for different transition energies and mod types as given in Table 6.3

Using the above two general format of Eqn (6.1) and (6.2) and with the help of Table 6.3, a set of empirical formula would appear to predict the first five optical transition energies of inner semiconducting tubes of S@M and S@S DWNTs with good accuracy. For five transitions with each mod type, there are total 8 cases listed in Table 6.3. For 7 of these cases,

the average absolute error over the full diameter range is below 2% and only for the first optical transitions it exceeds 2%. Calculated optical transitions are given in Table 6.4 along with the experimental values for the convenience of comparison.

Table 6.3 Parameters A and B for different optical transitions of ISCTs of DWNTs

Optical Transitions	MOD Type	A	B	Mean Percentage Error
1 st transition (E_{11}^S)	1	1.45	3.2	5.61 %
2 nd transition (E_{22}^S)	1	2.4	1.6	1.33 %
	2	2.3	3.6	0.99 %
3 rd transition (E_{33}^S)	1	4.4	4.7	1.34 %
	2	4.9	4.7	1.42 %
4 th transition (E_{44}^S)	1	5.1	2.7	1.79 %
	2	5.4	6.6	1.83 %
5 th transition (E_{55}^S)	1	7.5	9.7	0.097 %

Table 6.4 Optical transitions in Inner Semiconducting Tubes (ISCT) of DWNTs calculated from the proposed empirical model

ISCT Optical Transitions	Chirality of DWNTs inner@outer	Inner tube diameter di (nm)	Average diameter D (nm)	Optical transitions energy (eV)	
				ISCT of DWNT (exp)	ISCT of DWNT (Emp)
E_{11}^S (mod 1)	(8,4)@(18,2)	0.83	1.16	1.128	1.081
	(7,6)@(16,6)	0.88	1.21	1.058	1.063
	(10,6)@(14,13)	1.09	1.46	0.828	0.904
	(14,1)@(15,12)	1.13	1.48	0.792	0.861
E_{22}^S (mod 1)	(7,6)@(16,6)	0.88	1.21	1.82	1.816
	(10,6)@(14,13)	1.09	1.46	1.6	1.587
	(10,6)@(16,11)	1.09	1.46	1.6	1.582
	(14,1)@(15,12)	1.13	1.48	1.55	1.593
	(12,5)@(16,12)	1.18	1.54	1.5	1.525
E_{22}^S (mod 2)	(13,2)@(21,3)	1.10	1.43	1.39	1.385
	(12,4)@(16,11)	1.12	1.48	1.38	1.374
	(13,5)@(23,3)	1.26	1.59	1.28	1.308
E_{33}^S (mod 1)	(12,5)@(16,12)	1.20	1.57	2.44	2.396
	(12,8)@(25,2)	1.38	1.73	2.3	2.264
	(17,1)@(16,14)	1.39	1.73	2.13	2.140
	(18,5)@(20,14)	1.66	2.01	1.94	1.967
	(18,5)@(27,5)	1.66	2.02	1.905	1.959
	(16,9)@(24,10)	1.74	2.07	1.92	1.946
	(16,12)@(27,10)	1.93	2.28	1.81	1.799
	(23,4)@(22,18)	2.00	2.38	1.68	1.695
	(16,15)@(23,18)	2.13	2.48	1.66	1.678

ISCT Optical Transitions	Chirality of DWNTs inner@outer	Inner tube diameter di (nm)	Average diameter D (nm)	Optical transitions energy (eV)	
				ISCT of DWNT (exp)	ISCT of DWNT (Emp)
E_{33}^S (mod 2)	(13,8)@(16,15)	1.46	1.79	2.28	2.280
	(15,7)@(20,12)	1.55	1.88	2.24	2.267
	(14,9)@(17,16)	1.59	1.93	2.11	2.154
	(15,10)@(27,6)	1.73	2.07	2.02	2.037
	(19,8)@(21,18)	1.91	2.30	1.96	1.945
	(15,13)@(21,17)	1.93	2.27	1.9	1.832
E_{44}^S (mod 1)	(16,9)@(24,10)	1.71	2.04	2.39	2.400
	(16,12)@(27,10)	1.90	2.24	2.15	2.186
	(16,15)@(23,18)	2.09	2.44	2.09	2.021
E_{44}^S (mod 2)	(15,7)@(20,12)	1.52	1.85	2.42	2.448
	(15,10)@(27,6)	1.70	2.04	2.28	2.304
	(19,8)@(21,18)	1.87	2.26	2.15	2.092
	(15,13)@(21,17)	1.89	2.23	2.21	2.157
E_{55}^S (mod 1)	(16,12)@(27,10)	1.90	2.24	2.75	2.753

It can be noted from Table 6.4 that estimated values of different optical transitions from proposed model are very close to the experimentally reported values. Incorporation of average diameter of DWNT in proposed model also enabled it to reflect some specific and precise experimental observations. One such reported observation is, even for the same inner tube, the energy shift of an optical transition varies significantly with the outer-wall tube species. For example, (18,5)@(20,14) and (18,5)@(27,5) DWNTs, both have same inner semiconducting tube (18,5) but the optical transitions of (18,5) is different in two DWNTs due to the different chirality of outer tubes. As the model includes average diameter D, which

is different for two DWNTs having same inner tube but different outer tubes, so, the model can estimate the experimentally observed difference in optical transitions of the inner tube.

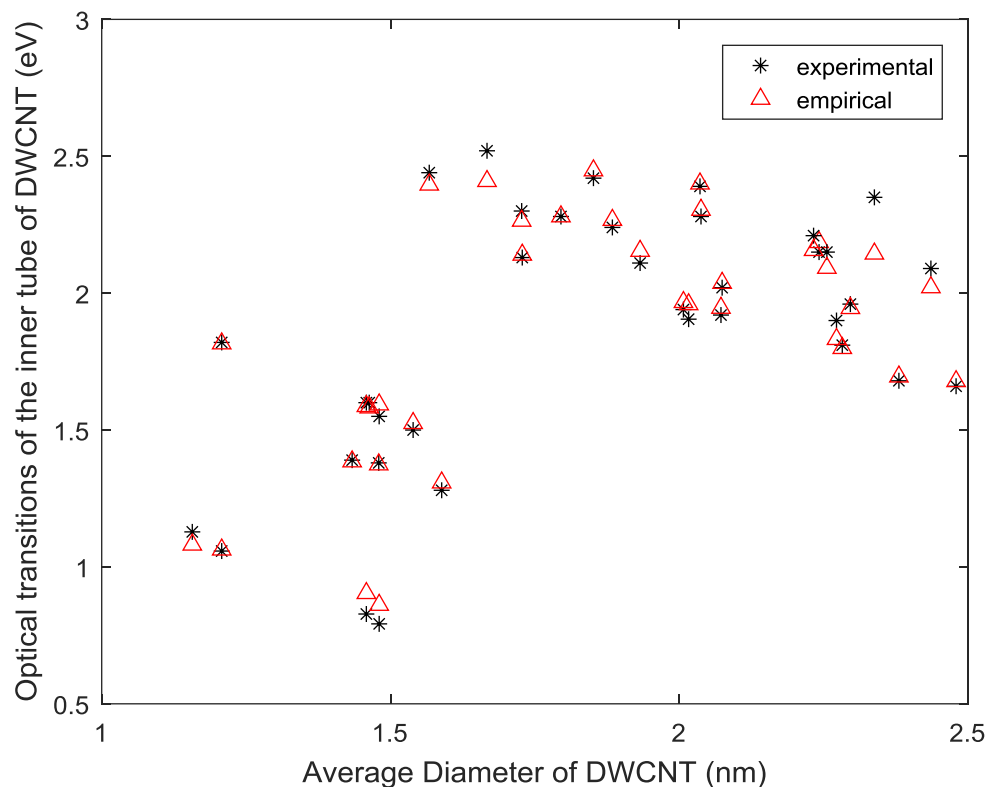


Figure 6.1: Empirical values of five optical transitions of inner semiconducting tubes of S@M and S@S DWNTs compared with experimental data with respect to average diameter of the DWNTs.

Experimental and empirical values of first five optical transitions of ISCTs of DWNTs are plotted in Fig. 6.1 against the average diameters of corresponding DWNTs. It can be easily noticed from this plot that empirical estimations matches very closely with experimental data for all transitions. Accuracy is relatively higher at higher diameters DWNTs as observed from both Fig. 6.1 and Table 6.3. Slight deviation is observed in some lower diameter tubes only but, they are within the tolerance margin. Thus, the proposed empirical relation can predict the experimentally reported red shift in optical transitions of inner semiconducting tubes of S@M and S@S DWNTs for both mod types with reasonable accuracy.

6.3 Conclusions

Different experimental work reported significant red shift of optical transitions of inner semiconducting tubes (ISCT) of S@M and S@S DWNTs. Here, an empirical model for estimating different optical transitions of ISCTs of S@M and S@S DWNTs from the chirality of inner SWCNTs and average diameter of DWNTs are proposed. The proposed model is used to calculate optical transitions of ISCTs of a number of DWCNTs and the result was found in good agreement with experimentally reported values. The proposed relation can help to understand the electronic behavior of DWNTs in terms of its structural parameters and can help identifying the chirality of unknown DWCNTs from their electronic properties.

CHAPTER 7

EMPIRICAL MODEL FOR BAND GAPS IN GRAPHENE NANORIBBONS

In second chapter, it was discussed that the armchair GNRs are believed to be the most promising candidates towards the design of graphene based circuits due to their highly tunable electronic properties [105, 106], making them an interesting material for room-temperature electronic and optoelectronic switching devices. Various models proposed by earlier authors along with their limitations in estimating the bandgaps in GNRs were also reviewed. Although first-principles approach combining density functional theory (DFT), the many-body perturbation theory with GW (single particle Green's function G and screened coulomb interaction W) approximation, and a semi-classical image-charge model to compute the electronic band gaps in GNRs weakly interacting with the underlying substrate gives bandgaps values close to experimental values, but, the GW method is computationally intensive and challenging to converge numerically. Besides, image charge (IC) corrections on top of GW calculations makes the computation more intensive. That's why a simple and model independent empirical relation is required to predict the bandgaps of AGNRs with high accuracy.

7.1 Experimental Observations Regarding Armchair GNRs

As a first step to develop the proposed empirical model for estimating the bandgaps of AGNRs with their width and number of armchair chains N , following facts can be recalled from earlier theoretical calculation [108, 110, 113, 114] and experimental observations [106, 119],

- i) All AGNRs are semiconductors with some energy gaps.
- ii) Their bandgaps as a function of ribbon width are well separated into three different subfamilies for $N = 3p$, $3p + 1$ or $3p+2$, where p is a positive integer.

iii) Their bandgaps decreases with increasing ribbon width (w) within each of those families and the gap size hierarchy is $3_{p+1} > 3_p > 3_{p+2} \neq 0$.

iv) $N = 3p + 2$ AGNRs display a much smaller gap comparing to that of the other two categories.

Recently, Wang *et al.* [106] studied electronic structures of the armchair GNRs with atomically well-defined widths (0.6 to 3.1 nm) ranging from $N=6$ to $N=26$ by using a scanning tunneling microscope. Their result demonstrated explicitly that all the studied armchair GNRs exhibit semiconducting gaps and, more importantly, the observed gaps as a function of N are well grouped into the three categories. For each category, the energy gaps of the GNRs decrease with increasing N , as expected to be observed due to the quantum confinement. A notable feature of the spectra is that the $N = 3p + 2$ armchair GNRs display a much smaller gap comparing to that of the other two categories. Thus, in formulating proposed empirical relations, the focus will be on $N=3p$ and $3p+1$ subfamilies, ignoring $N=3p+2$ AGNRs.

7.2 Proposed Empirical Model for Bandgaps of Armchair GNRs

Proposed empirical equation is composed of two terms. First term is to reflect the decreasing trend of bandgaps with increasing ribbon width (w) and is expressed by the form $a/(w+b)$ where, a and b are fitting constant. The second term is to incorporate the difference in bandgaps due to two different categories $N=3p$ and $N=3p+1$. After careful observation, it was found that a term $\text{Cos}(p\pi/(N+1))$ can reflect this difference precisely. Based on these findings, here two simple empirical relations for bandgaps of AGNRs are proposed separately for $N=3p$ and $3p+1$ subfamilies,

$$E_g (eV) = \frac{0.8}{w+0.07} + \text{Cos} \frac{p\pi}{N+1}, \text{ (for } N = 3p) \quad (7.1)$$

$$= \frac{1.6}{w+0.25} + \text{Cos} \frac{p\pi}{N+1}. \text{ (for } N = 3p+1) \quad (7.2)$$

These equations reflect well established dependence of AGNRs bandgap on ribbon width w and number of armchair chains N and predicts experimental bandgaps of AGNRs reported till date with very good accuracy.

Table 7.1 and 7.2 presents the comparison of the predicted bandgaps from the proposed empirical Eqn (7.1) and (7.2) with the calculated results from Eqn (2.8) through Eqn (2.19) along with the measured bandgaps of AGNRs from different experiments.

Table 7.1 and 7.2 clearly show that earlier models [108-111, 113] either underestimate or overestimate the bandgaps of different AGNRs whereas the empirical relation predicts the experimental results very well with a high degree of accuracy.

Table 7.1 For AGNRs with $N=3p$

Arm-chair chains $N(=3p)$	GNR width (w) nm	$E_g^{[108]}$ eV	$E_g^{[109]}$ eV	$E_g^{[110]}$ eV	$E_g^{[111]}$ eV	$E_g^{[113]}$ eV	Exp eV	Emp eV
3	0.246	1.913	2.825	4.034	12.341	3.496	3.23 ± 0.08	3.239
6	0.615	1.107	2.121	2.734	4.937	1.398	1.69 ± 0.10	1.791
9	0.984	0.778	1.698	2.067	3.085	0.874	1.35 ± 0.07	1.347
12	1.353	0.600	1.416	1.662	2.244	0.636	1.13 ± 0.05	1.130
15	1.722	0.488	1.214	1.390	1.763	0.499	1.03 ± 0.04	1.002
18	2.091	0.411	1.062	1.194	1.452	0.411	0.90	0.917

Table 7.2 For AGNRs with $N=3p+1$

Arm- chair chains $N(=3p+1)$	GNR width (w) nm	$E_g^{[108]}$ eV	$E_g^{[109]}$ eV	$E_g^{[110]}$ eV	$E_g^{[111]}$ eV	$E_g^{[113]}$ eV	Exp eV	Emp eV
7	0.738	1.544	4.257	3.834	4.114	1.409	2.37 ± 0.06	2.327
13	1.476	0.864	2.128	2.342	2.057	0.705	1.4 ± 0.1	1.550
16	1.845	0.708	1.703	1.960	1.646	0.564	-	1.366

Measured and calculated bandgaps of AGNRs are plotted in Fig. 7.1 (a) and (b) against the ribbon width. It shows the calculations by Son *et al.* [108], Wakabayashi *et al.* [109], Yang *et al.* [110], Pandya *et al.* [111] and Raza *et al.* [113] along with the result from proposed empirical equations and the experimental values of bandgaps [105, 115, 119, 122]. From this Figure, the overestimation or underestimation of experimental bandgaps calculated by previous models and the relative high accuracy of the prediction by the empirical model can be observed very clearly.

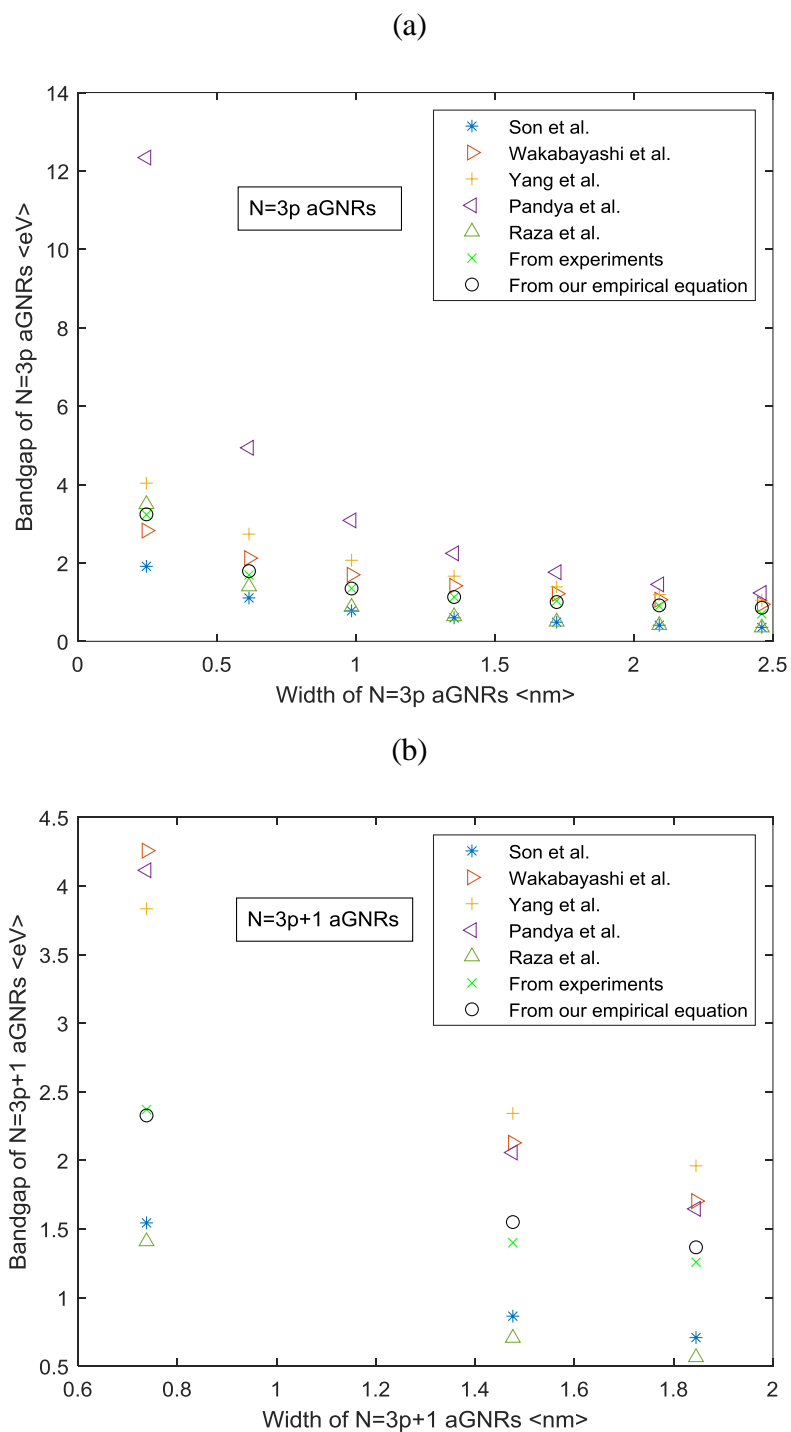


Figure 7.1: Measured and calculated bandgaps of AGNRs vs ribbon width including the result from empirical equations for (a) $N=3p$ and (b) $N=3p+1$. The experimental bandgaps for AGNRs are taken from ref. [105-107, 115-122]. Bandgaps calculated by different authors are taken from ref [108-111, 113].

Proposed empirical equation can be taken as a guide to predict the bandgaps of unknown AGNRs before considering them or selecting them for relevant optoelectronic applications. One such application is emission of light in visible and CIR spectrum as discussed in section 4.5. Table 4.3 and 4.4 of chapter-4 are updated here as Table 7.3 and 7.4, respectively, by including AGNRs.

Table 7.3 SWCNTs and AGNRs for emitting light in visible Spectrum

Color	Wavelength (nm)	Frequency (THz)	Photon energy (eV)	Potential SWCNT or AGNR with E_{II} (eV)
violet	380–450	670–790	2.75–3.26	3-AGNR→3.24 eV 7-AGNR→2.86 eV [114, 117]
blue	450–485	620–670	2.56–2.75	7-AGNR→2.7 eV [119]
cyan	485–500	600–620	2.48–2.56	7-AGNR→2.5 eV [122]
green	500–565	530–600	2.19–2.48	(5,0)→2.44 eV 7-AGNR→2.33 eV
yellow	565–590	510–530	2.10–2.19	7-AGNR→2.1 eV [194]
orange	590–625	480–510	1.98–2.10	(4,2) →2.03 eV
Red	625–750	400–480	1.65–1.98	(5,3) →1.72 eV (4,3) →1.70 eV (6,1) →1.85 eV 6-AGNR→1.79 eV

Table 7.4 SWCNTs and AGNRs for emitting light in CIR Spectrum

Color	Wavelength (nm)	Photon energy (eV)	Potential SWCNT or AGNR with E_{II} (eV)
Green to Red (visible light)	500-700	1.77-2.48	6-AGNR→1.79 eV (6,1) →1.85 eV (4,2) →2.03 eV 7-AGNR→2.1 eV [194] 7-AGNR→2.33 eV (5,0)→2.44 eV
NIR (Near Infrared)	700-900	1.38-1.77	(5,4) →1.43 eV (6,2) →1.45 eV (7,2) →1.51 eV 13-AGNR→1.55 eV (8,0) →1.59 eV (5,3) →1.62 eV (4,3) →1.70 eV

It can be noted that 7-AGNR is placed in multiple spectrum. According to the multiple STM/STS studies and also voltage dependent conductance studies [110, 114-117, 119, 122, 192-196], the 7-AGNR has a quasiparticle band gap of 2.3 –2.8 eV [192], the lowest values were registered for the Au-supported nanoribbons (with a bandgap~2.3 eV) [116], while the highest values were reported for the nanoribbons supported on an insulator NaCl layer (with a bandgap~2.8 eV) [114]. Reported experimental values of bandgap in 7-AGNRs are 2.3

[116], 2.4 [115], 2.5 [122], 2.7 [119], 2.8 [117] and 2.86 eV [114]. Controlling the substrate interaction is thus considered a prerequisite for studying the on-surface synthesis process and accessing the intrinsic electronic structure of GNRs [193]. One can expect even higher values of the band gap up to 3.7 eV for the freestanding 7-AGNRs, as found from GW quasiparticle band gap calculations for isolated AGNRs [110, 114, 192, 193]. Besides, reported experimental excitonic optical transition E_{11} (which slightly differs from bandgap due to binding energy) of 7-AGNR gives different values as 2.05 [192], 2.1 [194, 195] and 2.2 eV [196].

CHAPTER 8

CONCLUSIONS

Single wall carbon nanotubes, double wall carbon nanotubes and grapheme nanoribbons are highly sensitive to their chirality. Slight change in chirality drastically changes their overall behavior. Conventional models do not fully include chirality dependent behaviours of CNTs and GNRs. As a result, estimated result from conventional models deviate significantly from experimental values. Here, Chirality dependent empirical modeling of optical transition energies in different types of single and double wall carbon nanotubes and GNRs have been developed. Empirical models for bandgaps of GNRs are also developed. Proposed empirical model can estimate different optical transition energies in semiconducting and metallic SWCNTs and Double wall carbon nanotubes (DWCNTs) and also bandgaps of armchair GNRs with great accuracy. Based on the empirical model, a new technique for chirality assignment is demonstrated. Experimental reports and emission from SWCNT based LEDs were used to check the validity of the estimated results from the proposed models. Striking similarity was observed between the estimated and experimentally observed emission. The model was found to predict the absorption and emission in CNT-based devices reliably. Based on the empirical model, combination of different SWCNTs and armchair GNRs are identified to be used in Light emitting devices in visible and CIR spectrum.

Furthermore, a semi-empirical model is developed to estimate the higher optical transitions in SWCNTs after many body correction. Proposed empirical relations and overall findings on Chirality dependence of different properties of SWCNTs and GNRs have great impact on selection and applications of these materials in nanoelectronics.

8.1 Novelty of the Work

Systematic variation and new family behavior of optical transition with chirality of the nanotubes and GNRs were found. An empirical model have been devised for SWCNTs, DWCNTs and GNRs based on the findings which delivers a number of empirical relations. The model was extended for estimating optical transitions for perpendicular polarization of

light too. A semi-empirical model is developed to include the excitonic effect in CNTs for many body corrections in higher optical transitions of semiconducting SWCNTs. Estimated values show excellent agreement with experimental values for different transitions over the full diameter range and matches with the emissions observed from CNT based LEDs. Moreover, proposed empirical model gives a new technique for determining chiral index (n , m) of unknown semiconducting SWCNTs.

8.2 Limitations

This work proposes empirical models for estimating inter-band optical transitions of semiconducting and metallic SWCNTs and DWCNTs and bandgaps in armchair GNRs. Though the estimated optical transitions are validated by experimental results but, this is an empirical model, not analytical. Hence, it is not the substitute of, and does not eliminate the necessity of a complete theoretical model that could analytically explain experimentally reported various electronic behaviors of CNTs and GNRs till date. Also, though there are sufficient experimental data on different optical transitions in SWCNTs, there are not still sufficient experimental data for bandgaps of armchair GNRs. Besides, there are still ambiguities regarding the bandgaps of some AGNRs of specific chirality. So, compared to CNTs, enough data for validating the proposed empirical model for bandgaps of armchair GNRs could not be used.

8.3 Future Scopes

A complete analytical model can be developed in future that can remove the limitations of the proposed empirical model. Though it was demonstrated how the proposed model can be extended for estimating optical transitions for perpendicular polarization of light, but in future a separate model of optical transitions for perpendicular polarization of light can be developed. Besides, advanced first-principles simulation methods can be used to validate and readjust the parameters used in the proposed empirical model. Finally, with the availability of more unambiguous experimental reports on bandgaps of AGNRs, the proposed model for estimating bandgaps can be fine-tuned further.

References

- [1] R. Shoukat, M. I. Khan, “Carbon nanotubes: a review on properties, synthesis methods and applications in micro and nanotechnology”, *Microsyst Technol* 27, pp.4183–4192, 2021.
- [2] K. Fujisawa, H. J. Kim, S. H. Go, H. Muramatsu, T. Hayashi, M. Endo, T. C. Hirschmann, M. S. Dresselhaus, Y. A. Kim, P. T. Araujo, “A Review of Double-Walled and Triple-Walled Carbon Nanotube Synthesis and Applications”, *Applied Sciences*. 6(4):109, 2016.
- [3] H. Wang, H. S. Wang, C. Ma, *et al.* “Graphene nanoribbons for quantum electronics”, *Nat Rev Phys* 3, pp.791–802, 2021.
- [4] L. Qian, Y. Xie, S. Zhang and J. Zhang, “Band Engineering of Carbon Nanotubes for Device Applications”, *Matter* 3, pp.664–695, 2020.
- [5] V. N. Popov, “Carbon nanotubes: properties and application”, *Materials Science and Engineering R*, 43, pp.61–102, 2004.
- [6] T. W. Odom, J. L. Huang, P. Kim, and C. M. Lieber, “Structure and Electronic Properties of Carbon Nanotubes”, *J. Phys. Chem. B*, 104, pp.2794-2809, 2000.
- [7] N. Hamada, S. Sawada, and A. Oshiyama, “New one-dimensional conductors: graphitic microtubules,” *Phys. Rev. Lett.*, Vol.68, No.10, pp.1579-1581, 1992.
- [8] H. Zeng, H. F. Hu, J. W. Wei, Z. Y. Wang, L. Wang, and P. Peng, “Curvature effects on electronic properties of small radius nanotube”, *Appl. Phys. Lett.* 91, 033102, 2007.
- [9] V. Zólyomi and J. Kúrti, “First-principles calculations for the electronic band structures of small diameter single-wall carbon nanotubes”, *Phys. Rev. B* 70, 085403, 2004.
- [10] Y. A. Kim, K. S. Yang, H. Muramatsu, M. Endo, M. Terrones, M. S. Dresselhaus, ‘Double-walled carbon nanotubes: synthesis, structural characterization, and application’, *Carbon letters*, 15 (2), pp. 77–88. 2014.
- [11] T. Grace, L. Yu, C. Gibson, D. Tune, H. Alturaif, Z. Al Othman, J. Shapter, ‘Investigating the Effect of Carbon Nanotube Diameter and Wall Number in Carbon Nanotube/Silicon Heterojunction Solar Cells’, *Nanomaterials*, 6(3), 52, 2016.
- [12] A. K. Geim and K. S. Novoselov, “The Rise of Graphene”, *Nat. Mater.*, 6, pp.183–9, 2007.

- [13] K. Nakada, M. Fujita, G. Dresselhaus, M. S. Dresselhaus, “Edge state in graphene ribbons: Nanometer size effect and edge shape dependence”, *Phys. Rev. B* 54, 17954, 1996.
- [14] L. Brey *et al.* “Electronic states of graphene nanoribbons studied with the Dirac equation”. *Phys. Rev. B*, 73, 235411, 2006.
- [15] V. Barone, O. Hod, and G. E. Scuseria, “Electronic Structure and Stability of Semiconducting Graphene Nanoribbons”, *Nano Lett.* 6, pp.2748-2754, 2006.
- [16] E. H. Hároz, J. G. Duque, X. Tu, M. Zheng, A. R. H. Walker, R. H. Hauge, S. K. Doorn and J. Kono, ‘Fundamental optical processes in armchair carbon nanotubes’, *Nanoscale*, 5, pp.1411-1439, 2013.
- [17] Jean-Christophe Blancon, “Optical absorption and electronic properties of individual carbon nanotubes”, Physics [physics]. Université Claude Bernard - Lyon I, 2013. English. NNT: 2013LYO10164. tel-01171001.
- [18] H. Ajiki, T. Ando, “Aharonov-Bohm effect in carbon nanotubes”, *Physica B: Condensed Matter*, Vol. 201, pp. 349-352, 1994.
- [19] I. Milošević, T. Vuković, S. Dmitrović, and M. Damnjanović, “Polarized optical absorption in carbon nanotubes: A symmetry-based approach”, *Phys. Rev. B* 67, 165418, 2003.
- [20] J. Jiang, R. Saito, A. Grüneis, G. Dresselhaus, M. S. Dresselhaus, “Optical absorption matrix elements in single-wall carbon nanotubes”, *Carbon*, Vol. 42, Issue 15, pp. 3169-3176, 2004.
- [21] A. Grüneis, R. Saito, J. Jiang, Ge. G. Samsonidze, M. A. Pimenta, A. Jorio, A. G. Souza Filho, G. Dresselhaus, M.S. Dresselhaus,, “Resonant Raman spectra of carbon nanotube bundles observed by perpendicularly polarized light”, *Chemical Physics Letters*, Vol. 387, Issues 4–6, Pages 301-306, 2004.
- [22] S. Uryu and T. Ando, “Exciton absorption of perpendicularly polarized light in carbon nanotubes”, *Phys. Rev. B* 74, 155411, 2006.
- [23] S. Uryu and T. Ando, “Cross-polarized exciton absorption in carbon nanotubes with Aharonov-Bohm flux”, *Phys. Rev. B* 76, 115420, 2007.
- [24] S. Uryu and T. Ando, “Environment effect on cross-polarized excitons in carbon nanotubes”, *Phys. Rev. B*, 86(12):125412, 2012.

- [25] S. Kilina, S. Tretiak, S. K. Doorn, Z. Luo, F. Papadimitrakopoulos, A. Piryatinski, Avadh Saxena, and A. R. Bishop, “Cross-polarized excitons in carbon nanotubes”, *PNAS*, 105(19), pp.6797–6802, 2008.
- [26] S. Motavas, A. Ivanov, A. Nojeh,, “The effect of light polarization on the interband transition spectra of zigzag carbon nanotubes and its diameter dependence”, *Physica E:Low-dimensional Systems and Nanostructures*, Vol. 56, pp.79-84, 2014.
- [27] H. Liu, “Influence of strong screening effect on the perpendicular- polarized linear excitonic absorption spectra of semiconducting carbon nanotubes”, *Eur. Phys. J. B* 89, 230, 2016.
- [28] Z. Yu and L. Brus, “Rayleigh and Raman Scattering from Individual Carbon Nanotube Bundles”, *The Journal of Physical Chemistry B* 105 (6), pp. 1123-1134, 2001.
- [29] A. Jorio, A. G. Souza Filho, V. W. Brar, A. K. Swan, M. S. Ünlü, B. B. Goldberg, A. Righi, J. H. Hafner, C. M. Lieber, R. Saito, G. Dresselhaus, and M. S. Dresselhaus, “Polarized resonant Raman study of isolated single-wall carbon nanotubes: Symmetry selection rules, dipolar and multipolar antenna effects”, *Phys. Rev. B* 65, 121402(R), 2002.
- [30] M. F. Islam, D. E. Milkie, C. L. Kane, A. G. Yodh, and J. M. Kikkawa, “Direct Measurement of the Polarized Optical Absorption Cross Section of Single-Wall Carbon Nanotubes”, *Phys. Rev. Lett.* 93, 037404, 2004.
- [31] Y. Miyauchi, M. Oba, and S. Maruyama, “Cross-polarized optical absorption of single-walled nanotubes by polarized photoluminescence excitation spectroscopy”, *Phys. Rev. B* 74, 205440, 2006.
- [32] J. Lefebvre and P. Finnie, “Polarized Photoluminescence Excitation Spectroscopy of Single-Walled Carbon Nanotubes”, *Phys. Rev. Lett.* 98, 167406, 2007.
- [33] J. C. Blancon, , M. Paillet, H. Tran *et al.*, “Direct measurement of the absolute absorption spectrum of individual semiconducting single-wall carbon nanotubes”, *Nat Commun* 4, 2542, 2013.
- [34] K. Liu, X. Hong, S. Choi, C. Jin, R. Capaz, J. Kim, *et al.*, “Systematic determination of absolute absorption cross-section of individual carbon nanotubes”, *Proc. Natl. Acad. Sci. USA.*, 111, pp.7564-7569, 2014.

- [35] K. Yanagi, R. Okada, Y. Ichinose, “Intersubband plasmons in the quantum limit in gated and aligned carbon nanotubes”, *Nat Commun* 9, 1121, 2018.
- [36] Green *et al.*, “Bright and Ultrafast Photoelectron Emission from Aligned Single-Wall Carbon Nanotubes through Multiphoton Exciton Resonance”, *Nano Lett.* 19, 1, pp.158–164, 2019.
- [37] M. Barkelid, G. A. Steele, and V. Zwiller, “Probing optical transitions in individual carbon nanotubes using polarized photocurrent spectroscopy”, *Nano Lett.*, 12(11), pp.5649–5653, 2012.
- [38] Y. Hirana, G. Juhasz, Y. Miyauchi, S. Mouri, K. Matsuda, N. Nakashima, “Empirical Prediction of Electronic Potentials of Single-Walled Carbon Nanotubes With a Specific Chirality (n,m)”, *Scientific Reports* 3, 2959, 2013.
- [39] K. Liu, J. Deslippe, F. Xiao, R. B. Capaz, X. Hong, S. Aloni, F. Wang, “An atlas of carbon nanotube optical transitions”, *Nature Nanotechnology* 7, 325–329, 2012.
- [40] A. Jorio, C. Fantini, M. A. Pimenta, R. B. Capaz, Ge. G. Samsonidze, G. Dresselhaus, M. S. Dresselhaus, J. Jiang, N. Kobayashi, A. Grüneis, R. Saito, “Resonance Raman spectroscopy (n, m)-dependent effects in small-diameter single-wall carbon nanotubes”, *Phys. Rev B*, 71, 075401, 2005.
- [41] Ge. G. Samsonidze, R. Saito, N. Kobayashi, A. Grüneis, J. Jiang, A. Jorio, S. G. Chou, G. Dresselhaus, M. S. Dresselhaus, “Family behavior of the optical transition energies in single-wall carbon nanotubes of smaller diameters”, *Appl. Phys. Lett.* 85(23), 5703-5705, 2004.
- [42] R. Saito, G. Dresselhaus, M. S. Dresselhaus, “Trigonal warping effect of carbon nanotubes”, *Phys. Rev. B* 61(4), 2981-2990, 2000.
- [43] H. Kataura, Y. Kumazawa, Y. Maniwa, I. Umezue, S. Suzuki, Y. Ohtsuka, Y. Achiba, “Optical properties of single-wall carbon nanotubes”, *Synthetic Met.* 103, 2555, 1999
- [44] M. Y. Sfeir, T. Beetz, F. Wang, L. Huang, X. M. H. Huang, M. Huang, J. Hone, S. O’Brien, J. A. Misewich, T. F. Heinz, L. Wu, Y. Zhu, L. E. Brus, “Optical Spectroscopy of Individual Single-Walled Carbon Nanotubes of Defined Chiral Structure”, *Science* 312(5773), 554-556, 2006.
- [45] R. B. Weisman, S. M. Bachilo, “Dependence of optical transition energies on structure for single-walled carbon nanotubes in aqueous suspension: an empirical kataura plot”, *Nano Lett.* 3(9), 1235-1238, 2003.

- [46] C. L. Kane, E. J. Mele, “The Ratio Problem in Single Carbon Nanotube Fluorescence Spectroscopy”, *Phys. Rev. Lett.* 90, 207401, 2003.
- [47] S. M. Bachilo, M. S. Strano, C. Kittrell, R. H. Hauge, R. E. Smalley, R. B. Weisman, “Structure-Assigned Optical Spectra of Single-Walled Carbon Nanotubes” *Science* 298(5602), 2361, 2002.
- [48] J. D. Correa, A. J. R. da Silva, M. Pacheco, “Tight-binding model for carbon nanotubes from ab initio calculations”. *J. Phys.: Condens. Matter* 22(7), 275503, 2010.
- [49] V. N. Popov “Curvature effects on the structural, electronic and optical properties of isolated single-walled carbon nanotubes within a symmetry-adapted non-orthogonal tight-binding model”. *New Journal of Physics* 6(1), 17, 2004.
- [50] J. W. Ding, X. H. Yan, J. X. Cao, “Analytical relation of band gaps to both chirality and diameter of single-wall carbon nanotubes”, *Phys. Rev. B* 66(7), 073401, 2002.
- [51] H. Yorikawa, S. Muramatsu, “Chirality-dependence of energy gaps of semiconducting nanotubules”. *Solid State Communications* 94(6), 435-437, 1995.
- [52] P. T. Araujo, S. K. Doorn, S. Kilina, S. Tretiak, E. Einarsson, S. Maruyama, H. Chacham, M. A. Pimenta, A. Jorio, “Third and Fourth Optical Transitions in Semiconducting Carbon Nanotubes”. *Phys. Rev. Lett.* 98, 067401, 2007.
- [53] J. Maultzsch, H. Telg, S. Reich, C. Thomsen, “Radial breathing mode of single-walled carbon nanotubes Optical transition energies and chiral-index assignment”, *Phys. Rev. B* 72, 205438, 2005.
- [54] S. Okada, S. Ogawa, and S. Maruyama, “Curvature Effects on Electron States of Semiconducting Nanotubes”, *Appl. Phys. Lett.* 91, 033102, 2007.
- [55] J. Maultzsch , C. Thomsen , “Characterization of Carbon Nanotubes by Optical Spectroscopy, Advanced Micro and Nanosystems”, *Carbon Nanotube Devices*, Vol. 8., Edited by Christofer Hierold, Verlag GmbH and Co. KGaA, Weinheim, Berlin, Germany, 2008.
- [56] E. J. Mele, C.L. Kane, “Many body effects in carbon nanotube fluorescence spectroscopy”, *Solid State Communications* 135, pp. 527–531, 2005.
- [57] H. Lin, J. Lagoute, V. Repain, C. Chacon, Y. Girard, J.-S. Lauret, F. Ducastelle, A. Loiseau S. Rousset , “Many-body effects in electronic bandgaps of carbon nanotubes measured by scanning tunnelling spectroscopy”, *Nature Materials* 9, 235–238, 2010.

- [58] C. D. Spataru, S. I. Beigi, L. X. Benedict and S. G. Louie, “Excitonic Effects and Optical Spectra of Single-Walled Carbon Nanotubes”, *Phys. Rev. Lett.* 92, 077402, 2004.
- [59] H. Zhao, S. Mazumdar, “Excitons in semiconducting single-walled carbon nanotubes”, *Synthetic Metals*, 155, p.250–253, 2005.
- [60] G. Dukovic, F. Wang, D. Song, M. Y. Sfeir, T. F. Heinz and L. E. Brus, “Structural dependence of excitonic optical transitions and band-gap energies in carbon nanotubes”, *Nano Lett.* 5, pp. 2314-2318, 2005.
- [61] O. G`ulseren, T. Yildirim and S. Ciraci, “A systematic ab-initio study of curvature effects in carbon nanotubes”, *Phys. Rev. B* 65, 153405, 2002.
- [62] Francois Leonard, “The physics of carbon nanotube devices”, Ed: Jeremy Ramsden, *William Andrew Inc.* Norwich, New York. 2009.
- [63] C. L. Kane and E. J. Mele, “Size, shape, and low energy electronic structure of carbon nanotubes,” *Phys. Rev. Lett.*, vol. 78, pp. 1932–1935, 1997.
- [64] G. Bertoni, L. Calmels, “First-principles calculation of the electronic structure and energy loss near edge spectra of chiral carbon nanotubes”, *Micron* 37, pp.486–491, 2006.
- [65] M. Machón, S. Reich, C. Thomsen, D. S. Portal and P. Ordejón, “*Ab initio* calculations of the optical properties of 4-Å-diameter single-walled nanotubes”, *Phys. Rev. B* 66, 155410, 2002.
- [66] X. P. Yang, H. M. Weng and J. Dong, “Optical properties of 4 Å single-walled carbon nanotubes inside the zeolite channels studied from first principles calculations”, *The European Physical Journal B - Condensed Matter and Complex Systems*, Vol. 32, No. 3, pp.345-350, 2003.
- [67] G. D. Li, Z.K. Tang, N. Wang, J. S. Chen, “Structural study of the 0.4-nm single-walled carbon nanotubes aligned in channels of AlPO₄-5 crystal”, *Carbon*, 40, pp.917–921, 2002.
- [68] W. Z. Liang, G. Chen, Z. Li, Z. K. Tang, “Absorption spectra and chirality of single-walled 4 Å carbon nanotubes”, *Applied Physics Letters*, vol. 80 no. 18, pp. 3415-3417, 2002.

- [69] P. Lambin, F. Troizon and V. Meunier, “Electronic Transport in Nanotubes and Through Junctions of Nanotubes”, *Carbon Nanotubes:NATO Science Series*, Volume 222, III, pp. 123-142, 2006.
- [70] A. Javey, J. Kong, Editors: “Carbon Nanotube Electronics”, pp. 16, 35, *Springer Science and Business Media*, LLC, 2009.
- [71] R. Saito and H. Kataura, “Optical Properties and Raman Spectroscopy of Carbon Nanotubes”, *Carbon Nanotubes*, Edited by M. S. Dresselhaus, G. Dresselhaus, Ph. Avouris, Topics in Applied Physics, Vol. 80, pp.213-247, Springer-Verlag Berlin Heidelberg, 2001.
- [72] J. Maultzsch, H. Telg, S. Reich, C. Thomsen, “Radial breathing mode of single-walled carbon nanotubes Optical transition energies and chiral-index assignment”, *Phys. Rev. B* 72, 205438, 2005.
- [73] H. Yorikawa, S. Muramatsu, “Electronic structure characteristic of carbon nanotubules”, *Z. Phys. B, Condensed Matt.*, vol. 104, pp. 71–76, 1997.
- [74] A. Jorio, C. Fantini, M. A. Pimenta, R. B. Capaz, Ge. G. Samsonidze, G. Dresselhaus, M. S. Dresselhaus, J. Jiang, N. Kobayashi, A. Grüneis and R. Saito, “Resonance Raman spectroscopy (n,m)-dependent effects in small-diameter single-wall carbon nanotubes”, *Phys. Rev. B* 71, 075401, 2005.
- [75] J. Lefebvre, S. Maruyama and P. Finnie, “Photoluminescence: science and applications”, *Topics in Applied Physics*, Vol. 111, pp.287-319, 2008.
- [76] P. K. Valavala, D. Banyai, M. Seel, and R. Pati, “Self-consistent calculations of strain-induced band gap changes in semiconducting ($n,0$) carbon nanotubes,” *Phys. Rev. B*, Vol.78, No.23, pp.235430, 2008.
- [77] A. Jorio, P. Araujo, S. K. Doorn, S. Maruyama, H. Chacham, and M. A. Pimenta, “The Kataura plot over broad energy and diameter ranges,” *Phys. Stat. Sol. (b)*, Vol.243, No.13, pp.3117-3121, 2006.
- [78] H. Yorikawa and S. Muramatsu, “Energy gaps of semiconducting nanotubules,” *Phys. Rev. B*, Vol.52, No.4, pp.2723-2727, 1995.
- [79] H. Yorikawa and S. Muramatsu , “Chirality-dependence of energy gaps of semiconducting nanotubules” , *Solid State Communications*, Vol. 94, Issue 6, Pages 435-437, 1995.

- [80] G. Lanzani, L. Luer, “Carbon Nanotubes: Electronic Structure and Spectroscopy”, *Comprehensive Nanoscience and Technology*, Vol. 1, pp. 23–39, 2011.
- [81] J. X. Cao, X. H. Yan, J. W. Ding and D. L. Wang, “Band structures of carbon nanotubes: the sp^3s^* -tight-binding model”, *J. Phys.: Condens. Matter* 13, L271–L275, 2001.
- [82] M. K. Niranjana, “Theoretical investigation of electronic bandgaps of semiconducting single-walled carbon nanotubes using semi-empirical selfconsistent tight binding and ab-initio density functional methods”, *J. Phys. Commun.* 4, 015004, 2020.
- [83] E. Tetik, F. Karadağ, M. Karaaslan, İ. Çömez, "The Electronic Properties of the Graphene and Carbon Nanotubes: *Ab Initio* Density Functional Theory Investigation", *International Scholarly Research Notices*, Vol. 2012, 416417, p7, 2012.
- [84] P. Umari, O. Petrenko, S. Taioli, *et al.*, “Electronic band gaps of semiconducting zig-zag carbon nanotubes from many-body perturbation theory calculations”, *J. Chem. Phys.* 136, 181101, 2012.
- [85] Y. Matsuda, J. Tahir-Kheli, and W. A. Goddard, III, “Definitive Band Gaps for Single-Wall Carbon Nanotubes”, *J. Phys. Chem. Lett.*, 1, pp.2946–2950, 2010.
- [86] M. Endo, H. Muramatsu, T. Hayashi, Y. A. Kim, M. Terrones and N. S. Dresselhaus, “‘Buckypaper’ from coaxial nanotubes”, *Nature*, 433, 476, 2005.
- [87] L. Dong, J. Park, G. Leonhardt, S. Zhang, R. Liang, ‘Continuous Synthesis of Double-Walled Carbon Nanotubes with Water-Assisted Floating Catalyst Chemical Vapor Deposition’, *Nanomaterials*, 10(2), 365, 2020.
- [88] J. K. Streit, S. Lam, Y. Piao, A. R. Hight Walker, J. A. Fagan, M. Zheng, ‘Separation of Double-Wall Carbon Nanotubes by Electronic Type and Diameter’, *Nanoscale*, 9, pp. 2531-2540, 2017.
- [89] A. Ghedjatti, Y. Magnin, F. Fossard, G. Wang, H. Amara, E. Flahaut, J. S. Lauret, A. Loiseau, ‘Structural Properties of Double-Walled Carbon Nanotubes Driven by Mechanical Interlayer Coupling’, *ACS Nano*, 11 (5), pp. 4840-4847, 2017.
- [90] M. Soto, T. A. Boyer, S. Biradar, L. Ge, R. Vajtai, A. E. Zúñiga, P. M. Ajayan and Barrera, “Effect of interwall interaction on the electronic structure of double-walled carbon nanotubes”, *Nanotechnology*, 26(16), 165201, 2015.

- [91] M. Soto, R. Vajtai, P. M. Ajayan and E V Barrera, ‘Carbon nanotube conditioning part 1— effect of interwall interaction on the electronic band gap of double-walled carbon nanotubes’, *Nanotechnology* 29, 045701, 2018.
- [92] J. -C. Charlier, J. -P. Michenaud, “Energetics of multilayered carbon tubules”, *Phys. Rev. Lett.*, 70, pp. 1858-1861, 1993.
- [93] D. Shimamoto, H. Muramatsu, T. Hayashi, Y. A. Kim, M. Endo, J. S. Park, R. Saito, M. Terrones and M. S. Dresselhaus, “Strong and stable photoluminescence from the semiconducting inner tubes within double walled carbon nanotubes”, *Appl. Phys. Lett.* 94, 083106, pp. 1-3, 2009.
- [94] K. Liu, C. Jin, X. Hong, *et al.* “Van der Waals-coupled electronic states in incommensurate double-walled carbon nanotubes”, *Nature Phys* 10, pp. 737–742, 2014.
- [95] H. N. Tran, J. C. Blancon, R. Arenal, R. Parret, A. A. Zahab, A. Ayari, F. Vallée, N. Del Fatti, J. L. Sauvajol, and M. Paillet, “Quantum interference effects on the intensity of the G modes in double-walled carbon nanotubes”, *Phys. Rev. B* 95, 205411, pp.1-9, May 2017.
- [96] D. I. Levshov, R. Parret, H. N. Tran, T. Michel, T.T. Cao, V. C. Nguyen, R. Arenal, V. N. Popov, S. B. Rochal, J. L. Sauvajol, A. A. Zahab, M. Paillet, ‘Photoluminescence from an individual double-walled carbon nanotube’, *Phys. Rev. B*, 96, 195410, November 2017.
- [97] S. Zhao, P. Moon, Y. Miyauchi, T. Nishihara, K. Matsuda, M. Koshino, and R. Kitaura, “Observation of Drastic Electronic-Structure Change in a One-Dimensional Moiré Superlattice”, *Phys. Rev. Lett.* 124, 106101, pp.1-6, March, 2020.
- [98] D. V. Chalin and S. B. Rochal, “Band structure and inter-tube optical transitions in double-walled carbon nanotubes”, *Phys. Rev. B* 102, 115426, pp. 1-12, September, 2020.
- [99] S. Zhao, T. Kitagawa, Y. Miyauchi, *et al.* “Rayleigh scattering studies on inter-layer interactions in structure-defined individual double-wall carbon nanotubes”. *Nano Res.* 7, 1548–1555, 2014.
- [100] D. I. Levshov, T. Michel, R. Arenal, H. N. Tran, T. X. Than, M. Paillet, Yu. I. Yuzyuk, and J.-L. Sauvajol, “Interlayer Dependence of G-Modes in Semiconducting

- Double-Walled Carbon Nanotubes”, *The Journal of Physical Chemistry C* 119 (40), 23196-23202, 2015.
- [101] L. Brey *et al.* “Edge states and the quantized Hall effect in graphene”. *Phys. Rev. B*, 73, 195408, 2006.
- [102] F. Schwierz, J. Pezoldt and R. Granzner, “Two-dimensional materials and their prospects in transistor electronics”, *Nanoscale*, 7, 8261-8283, 2015.
- [103] C. N. Bondja, Z. Geng, R. Granzner, J. Pezoldt and F. Schwierz, “Simulation of 50-nm Gate Graphene Nanoribbon Transistors”, *Electronics* 5, 3, 2016.
- [104] Li, G., Yoon, KY., Zhong, X. *et al.* “A modular synthetic approach for band-gap engineering of armchair graphene nanoribbons”, *Nat Commun* 9, 1687, 2018.
- [105] N. M. Díez, A. G. Lekue, E. C. Sanroma, J. Li, M. Corso, L. Colazzo, F. Sedona, D. S. Portal, J. I. Pascual and D. G. de Oteyza, “Width-Dependent Band Gap in Armchair Graphene Nanoribbons Reveals Fermi Level Pinning on Au(111)”, *ACS Nano*, 11, pp. 11661–11668, 2017.
- [106] W. X. Wang, M. Zhou, X. Li, S. Y. Li, X. Wu, W. Duan and L. He, “Energy gaps of atomically precise armchair graphene sidewall nanoribbons”, *Phys. Rev. B*, 93, 241403(R), 2016.
- [107] B. O. Tayo, “Band gap engineering in finite elongated graphene nanoribbon heterojunctions: Tight-binding model”, *AIP Advances* 5, 087121, 2015
- [108] Y. W. Son, M. L. Cohen, and S. G. Louie, “Energy Gaps in Graphene Nanoribbons”, *Phys. Rev. Lett.* 97, 216803, 2006.
- [109] K. Wakabayashi, K. Sasaki, T. Nakanishi and T. Enoki, “Electronic states of grapheme nanoribbons and analytical solutions”, *Sci. Technol. Adv. Mater.* 11 054504, 2010.
- [110] L. Yang, C. H. Park, Y. W. Son, M. L. Cohen, and S. G. Louie, “Quasiparticle Energies and Band Gaps in Graphene Nanoribbons”, *Phys. Rev. Lett.* 99, 186801, 2007.
- [111] A. Pandya, K. Sangani, P. K. Jha, “Band gap determination of nanoribbons of Graphene, h- boron nitride, phosphorene, silicene, stanene, and germanene”, *J. Phys. D: Appl. Phys.* 53 415103, 2020.

- [112] M. Y. Han, B. Özyilmaz, Y. Zhang, and P. Kim, “Energy Band-Gap Engineering of Graphene Nanoribbons”, *Phys. Rev. Lett.* 98, 206805, 2007.
- [113] H. Raza and E. C. Kan, “Armchair graphene nanoribbons: Electronic structure and electric-field modulation”, *Phys. Rev. B* 77, 245434, 2008.
- [114] N. Kharche and V. Meunier, “Width and Crystal Orientation Dependent Band Gap Renormalization in Substrate-Supported Graphene Nanoribbons”, *J. Phys. Chem. Lett.* 7, pp. 1526-1533, 2016.
- [115] H. Söde, L. Talirz, O. Gröning, C. A. Pignedoli, R. Berger, X. Feng, K. Müllen, R. Fasel and P. Ruffieux, “Electronic band dispersion of graphene nanoribbons via Fourier-transformed scanning tunneling spectroscopy”, *Phys. Rev. B*, 91, 045429, 2015.
- [116] P. Ruffieux, J. Cai, N. Plumb, L. Patthey, D. Prezzi, A. Ferretti, E. Molinari, X. Feng, K. Müllen, C. A. Pignedoli, “Electronic structure of atomically precise graphene nanoribbons”, *ACS Nano*, 6, pp. 6930–6935, 2012.
- [117] S. Linden, D. Zhong, A. Timmer, N. Aghdassi, J. H. Franke, H. Zhang, X. Feng, K. Müllen, H. Fuchs, L. Chi, “Electronic structure of spatially aligned graphene nanoribbons on Au(788)”, *Phys. Rev. Lett.* 108, 216801, 2012.
- [118] L. Talirz, H. Sode, T. Dumsloff *et al.* “On-Surface Synthesis and Characterization of 9-Atom Wide Armchair Graphene Nanoribbons”, *ACS Nano*, 11, 1380-1388, 2017.
- [119] O. Deniz, C. Sanchez, T. Dumsloff, X. Feng, A. Narita, K. Mullen, N. Kharche, V. Meunier, M. Fasel and P. Ruffieux, “Revealing the Electronic Structure of Silicon Intercalated Armchair Graphene Nanoribbons by Scanning Tunneling Spectroscopy” *Nano Lett.* 17, 4, 2197–2203, 2017.
- [120] J. Yamaguchi, H. Hayashi, H. Jippo, “Small bandgap in atomically precise 17-atom-wide armchair-edged graphene nanoribbons”, *Commun Mater* 1, 36, 2020.
- [121] A. Kimouche, M. Ervasti, R. Drost, “Ultra-narrow metallic armchair graphene nanoribbons”, *Nat Commun* 6, 10177, 2015.
- [122] Y. C. Chen, D.G. de Oteyza, Z. Pedramrazi, C. Chen, F.R. Fischer, M. F. Crommie, “Tuning the band gap of graphene nanoribbons synthesized from molecular precursors”, *ACS Nano* 7, 6123–6128, 2013.

- [123] H. Telg, J. Maultzsch, S. Reich, C. Thomsen, “Resonant-Raman intensities and transition energies of the E_{11} transition in carbon nanotubes”, *Phys. Rev. B* 74, 115415, 2006.
- [124] S. K. Doorn, D. A. Heller, P. W. Barone, M. L. Usrey, M. S. Strano, “Resonant Raman excitation profiles of individually dispersed single walled carbon nanotubes in solution. *Appl. Phys. A* 78, 1147-1155, 2004.
- [125] H. Telg, J. Maultzsch, S. Reich, F. Hennrich, C. Thomsen, “Chirality Distribution and Transition Energies of Carbon Nanotubes” *Phys. Rev. Lett.* 93(17), 177401, 2004.
- [126] A. Jorio, A. P. Santos, H. B. Ribeiro, C. Fantini, M. Souza, J. P. M. Vieira, C. A. Furtado, J. Jiang, R. Saito, L. Balzano, D. E. Resasco, M. A. Pimenta, “Quantifying carbon-nanotube species with resonance Raman scattering”, *Phys. Rev. B* 72, 075207, 2005.
- [127] C. Fantini, A. Jorio, M. Souza, M. S. Strano, M. S. Dresselhaus, M. A. Pimenta, “Optical Transition Energies for Carbon Nanotubes from Resonant Raman Spectroscopy: Environment and Temperature Effects”. *Phys. Rev. Lett.* 93(14), 147406, 2004.
- [128] Q. Cao, J. Tersoff, D. B. Farmer, Y. Zhu, S. J. Han, ‘Carbon nanotube transistors scaled to a 40-nanometer footprint’, *Science*, 356 (6345), pp.1369-1372, 2017.
- [129] M. Kociak, A. Yu. Kasumov, S. Guéron, B. Reulet, I. I. Khodos, Yu. B. Gorbatov, V. T. Volkov, L. Vaccarini, and H. Bouchiat, “Superconductivity in Ropes of Single-Walled Carbon Nanotubes” *Phys. Rev. Lett.* 86, 2416, 2001.
- [130] A. A. Green, M. C. Hersam, “Colored semitransparent conductive coatings consisting of monodisperse metallic single-walled carbon nanotubes”, *Nano Lett.* 8, pp. 1417–1422, 2008.
- [131] M. S. Strano, S. K. Doorn, E. H. Haroz, C. Kittrell, R. H. Hauge and R. E. Smalley, “Assignment of (n, m) Raman and Optical Features of Metallic Single-Walled Carbon Nanotubes”, *Nano Lett.*, Vol.3, No.8, pp.1091-1096, 2003.
- [132] S. Berciaud, V. V. Deshpande, R. Caldwell, Y. Miyauchi, C. Voisin, P. Kim, J. Hone and T. F. Heinz, “All-optical structure assignment of individual single-walled carbon nanotubes from Rayleigh and Raman scattering measurements”, *Phys. Status Solidi B*, 249, No. 12, pp. 2436–2441, 2012.

- [133] Miyauchi, Yuhei, Z. Zhang, M. Takekoshi, Y. Tomio, H. Suzuura, V. Perebeinos, V. V. Deshpande. “Tunable Electronic Correlation Effects in Nanotube-Light Interactions”, *Phys. Rev. B*, 92 (20), 2015.
- [134] A. Graf, C. Murawski, Y. Zakharko, J. Zaumseil and M. C. Gather, “Infrared Organic Light-Emitting Diodes with Carbon Nanotube Emitters”, *Adv. Mater.*, 30, 1706711, 2018.
- [135] J. Maultzsch, C. Thomsen, “Characterization of Carbon Nanotubes by Optical Spectroscopy, Advanced Micro and Nanosystems”, *Carbon Nanotube Devices*, Vol. 8., Edited by Christofer Hierold, Verlag GmbH and Co. KGaA, Weinheim, Berlin, Germany, 2008.
- [136] C. Thomsen, H. Telg, J. Maultzsch and S. Reich, “Chirality assignments in carbon nanotubes based on resonant Raman scattering”, *Phys. stat. sol. (b)* 242, No. 9, pp.1802–1806, 2005.
- [137] D. I. Levshov, R. Parret, H. N. Tran, T. Michel, T.T. Cao, V. C. Nguyen, R. Arenal, V. N. Popov, S. B. Rochal, J. L. Sauvajol, A. A. Zahab, M. Paillet, ‘Photoluminescence from an individual double-walled carbon nanotube’, *Phys. Rev. B*, 96, 195410, 2017.
- [138] S. Chiashi, K. Kono, D. Matsumoto, J. Shitaba, N. Homma, A. Beniya, T. Yamamoto and Y. Homma, “Adsorption effects on radial breathing mode of single-walled carbon nanotubes”, *Phys. Rev. B* 91, 155415, 2015.
- [139] K. Liu, W. Wang, M. Wu, F. Xiao, X. Hong, S. Aloni, X. Bai, E. Wang, and F. Wang, “Intrinsic radial breathing oscillation in suspended single-walled carbon nanotubes”, *Phys. Rev. B* 83, 113404, 2011.
- [140] Y. Piao, J. R. Simpson, J. K. Striet, G. Ao, M. Zheng, J. A. Fagan, A. R. Hight Walker, “Intensity Ratio of Resonant Raman Modes for (n, m) Enriched Semiconducting Carbon Nanotubes”, *ACS Nano*, vol. 10 (5), pp. 5252–5259, 2016.
- [141] H. Telg, J. G. Duque, M. Staiger, X. Tu, F. Hennrich, M. M. Kappes, M. Zheng, J. Maultzsch, C. Thomsen, S. K. Doorn, Chiral index dependence of the G⁺ and G⁻ Raman modes in semiconducting carbon nanotubes, *ACS Nano*, vol. 6 (1), pp. 904–911, 2012.

- [142] K. Goß, N. Peica, C. Thomsen, J. Maultzsch, C. M. Schneider, C. Meyer, “Index assignment of a carbon nanotube rope using tip-enhanced Raman spectroscopy”, Vol. 248, Issue 11, pp.2577–2580, 2011.
- [143] R. D Rodriguez, M. Toader, S. Hermann, E. Sheremet, S. Müller, O. D. Gordan, H. Yu, S. E. Schulz, M. Hietschold and D. RT Zahn, “Nanoscale optical and electrical characterization of horizontally aligned single-walled carbon nanotubes”, *Nanoscale Res. Lett.*, Vol. 7 (1), p.682, 2012.
- [144] S. Wang, Q. Zeng, L. Yang, Z. Zhang, Z. Wang, T. Pei, L. Ding, X. Liang, M. Gao, Y. Li and L. Peng, “High-Performance Carbon Nanotube Light-Emitting Diodes with Asymmetric Contacts”, *Nano Letters* 11 (1), pp. 23-29, 2011.
- [145] T. Mueller, M. Kinoshita, M. Steiner, V. Prebeinos, A. A. Bol, D. B. Farmer, P. Avouris, “Efficient narrow-band light emission from a single carbon nanotube p–n diode”, *Nature Nanotech* 5, pp. 27–31, 2010.
- [146] D. Yu, S. Wang, L. Ye, W. Li, Z. Zhang, Y. Chen, J. Zhang, L. Peng, “Electroluminescence from Serpentine Carbon Nanotube Based Light- Emitting Diodes on Quartz”, *Small* 10(6), pp.1050-6, 2014.
- [147] M. H. P. Pfeiffer, N. Stürzl, C. W. Marquardt, M. Engel, S. Dehm, F. Hennrich, M. M. Kappes, U. Lemmer and R. Krupke, "Electroluminescence from chirality-sorted (9,7)-semiconducting carbon nanotube devices," *Opt. Express* 19, pp.1184-1189, 2011.
- [148] A. Vijayaraghavan, F. Hennrich, N. Stürzl, M. Engel, M. Ganzhorn, M. Oron-Carl, C. W. Marquardt, S. Dehm, S. Lebedkin, M. M. Kappes and R. Krupke, “Toward Single-Chirality Carbon Nanotube Device Arrays”, *ACS Nano* 4 (5), pp.2748-2754, 2010.
- [149] S. K. Choi, J. Deslippe, R. B. Capaz and S. G. Louie, “An Explicit Formula for Optical Oscillator Strength of Excitons in Semiconducting Single-Walled Carbon Nanotubes: Family Behavior”, *NanoLett.*,13 (1), pp.54–58, 2013.
- [150] S. Kilina and S. Tretiak, “Excitonic and Vibrational Properties of Single-Walled Semiconducting Carbon Nanotubes”, *Adv. Funct. Mater.* 17, 3405–3420, 2007.
- [151] T. Ando, “Excitons in carbon nanotubes”, *J. Phys. Soc. Jpn.* Vol. 66, p.1066, 1997.

- [152] C. D. Spataru, S. Ismail-Beigi, L. X. Benedict, S. G. Louie, “Excitonic effects and optical spectra of single-walled carbon nanotubes”, *Phys. Rev. Lett.* 92, 077402, 2004.
- [153] C. L. Kane and E. J. Mele, “Ratio Problem in Single Carbon Nanotube Fluorescence Spectroscopy”, *Phys. Rev. Lett.*, Vol. 90, No. 20, 207401, 2003.
- [154] E. J. Mele and C. L. Kane, “Many body effects in carbon nanotube fluorescence spectroscopy”, *Sol. Stat. Commn.*, Vol. 135, pp. 527–531, 2005.
- [155] C. L. Kane, E. J. Mele, “Electron interactions and scaling relations for optical excitations in carbon nanotubes”, *Phys. Rev. Lett.* 93, 197402, 2003.
- [156] V. Perebeinos, J. Tersoff, P. Avouris, “Effect of exciton-phonon coupling in the calculated optical absorption of carbon nanotubes”, *Phys. Rev. Lett.* 94, 027402, 2005.
- [157] T. G. Pedersen, “Exciton effects in carbon nanotubes”, *Carbon* 42, pp.1007–1010, 2004.
- [158] J. Jiang, R. Saito, Ge.G. Samsonidze, A. Jorio, S.G. Chou, G. Dresselhaus, M.S. Dresselhaus, “Chirality dependence of the exciton effects in single-wall carbon nanotubes:Tight-binding model”, *Phys. Rev. B* 75 035407, 2007.
- [159] K. Sato, R. Saito, J. Jiang,G. Dresselhaus and M.S. Dresselhaus, “Chirality dependence of many body effects ofsingle wall carbon nanotubes”, *Vibrational Spectroscopy*, Vol. 45, Issue 2, pp.89–94, 2007.
- [160] H. Zhao and S. Mazumdar, “Excitons in semiconducting single-walled carbon nanotubes”, *Synth. Met*, 155, pp.250–253, 2005.
- [161] H. Zhao and S. Mazumdar, “Electron-Electron Interaction Effects on the Optical Excitations of Semiconducting Single-Walled Carbon Nanotubes”, *Phys. Rev. Lett.*, Vol. 93, No. 15, 157402, 2004.
- [162] Z. Wang, D. Psiachos, R. F Badilla and S. Mazumdar, “Electron–electron interaction effects on the photophysics of metallic single-walled carbon nanotubes”, *J. Phys.: Condens. Matter* 21, 095009, 2009.
- [163] T. Ando, “Excitons in carbon nanotubes revisited: Dependence on diameter, Aharonov–Bohm flux, and strain”, *J. Phys. Soc. Jpn.* 73, 335, 2004.

- [164] T. Ando, “Family Effects on Excitons in Semiconducting Carbon Nanotubes”, *J. Phys. Soc. Jpn.* Vol. 78, No. 10, pp.104703, 2009.
- [165] A. Jorio, C. Fantini, M.A. Pimenta, R.B. Capaz, Ge.G. Samsonidze, G. Dresselhaus, M. S. Dresselhaus, J. Jiang, N. Kobayashi, A. Gruneis, R. Saito, “Resonance Raman spectroscopy (n , m) dependent effects in small diameter single-wall carbon nanotubes”, *Phys. Rev. B* 71, 075401, 2005.
- [166] Z. Wang, H. Pedrosa, T. Krauss and L. Rothberg, “Determination of the Exciton Binding Energy in Single-Walled Carbon Nanotubes”, *Phys Rev Lett.*, 96, 047403, 2006.
- [167] M. Ichida, S Mizuno, Y Saito, H Kataura, Y Achiba, A Nakamura. “Coulomb effect on the fundamental optical transition in semiconducting single-walled carbon nanotubes: divergent behavior in the small-diameter limit”, *Phys Rev B* 65, 241407, 2002.
- [168] M. Ichida, S Mizuno, Y Tani, Y Saito, A. Nakamura, “Exciton effects of optical transitions in single-wall carbon nanotubes”, *J Phys Soc Jpn*, 68, pp.3131–3, 1999.
- [169] J. Maultzsch, R. Pomraenke, S. Reich, E. Chang, D. Prezzi, A. Ruini, E. Molinari, M.S. Strano, C. Thomsen, C. Lienau, “Exciton binding energies in carbon nanotubes from two-photon photoluminescence”, *Phys. Rev. B* 72, 241402, 2005.
- [170] J. Maultzsch, R. Pomraenke, S. Reich, E. Chang, D. Prezzi, A. Ruini, E. Molinari, M. S. Strano, C. Thomsen, and C. Lienau, “Excitons in carbon nanotubes”, *Phys. stat. sol. (b)* 243, No. 13, pp. 3204–3208, 2006.
- [171] H. Lin, J. Lagoute, V. Repain, C. Chacon, Y. Girard, J.-S. Lauret, F. Ducastelle, A. Loiseau and S. Rousset, “Many body effects in electronic bandgaps of carbon nanotubes measured by scanning tunnelling spectroscopy”, *Nature Nanomaterials*, Vol 9, pp. 235-238, 2010.
- [172] G. Dukovic, F. Wang, D. Song, M. Y. Sfeir, T. F. Heinz and L. E. Brus, “Structural dependence of excitonic optical transitions and band-gap energies in carbon nanotubes”, *NanoLett.* 5, pp. 2314-2318, 2005.
- [173] F. Wang, G. Dukovic, L. E. Brus, T. F. Heinz, “The optical resonances in carbon nanotubes arise from excitons”, *Science* 308, pp.838-841, 2005.

- [174] T. Michel, M. Paillet, J. C. Meyer, V. N. Popov, L. Henrard and J. L. Sauvajol, “ E_{33} and E_{44} optical transitions in semiconducting single-walled carbon nanotubes: Electron diffraction and Raman experiments”, *Phys. Rev. B* 75, 155432, 2007.
- [175] T. Michel, M. Paillet, J. C. Meyer, V. N. Popov, L. Henrard, P. Poncharal, A. Zahab and J. L. Sauvajol, “Raman spectroscopy of (n,m)-identified individual single-walled carbon nanotubes”, *Phys. stat. sol. (b)* 244, No. 11, pp.3986–3991, 2007.
- [176] P. T. Araujo, S. K. Doorn, S. Kilina, S. Tretiak, E. Einarsson, S. Maruyama, H. Chacham, M.A. Pimenta, A. Jorio, “Third and fourth optical transitions in semiconducting carbon nanotubes”, *Phys. Rev. Lett.* 98, 067401, 2007.
- [177] A. Jorio, P.T. Araujo, S. K.Doorn, S. Maruyama, H. Chacham, M.A. Pimenta, “The Kataura plot over broad energy and diameter ranges”, *Phys. Stat. Sol. (b)* 243 3117, 2006.
- [178] M. K. Niranjana, “Theoretical investigation of electronic bandgaps of semiconducting single-walled carbon nanotubes using semi-empirical selfconsistent tight binding and ab-initio density functional methods”, *J. Phys. Commun.* 4, 015004, 2020.
- [179] P. Umari, O. Petrenko, S. Taioli, *et al.*, “Electronic band gaps of semiconducting zig-zag carbon nanotubes from many-body perturbation theory calculations”, *J. Chem. Phys.* 136, 181101, 2012.
- [180] E. H. Haroz, S. M. Bachilo, R. B. Weisman and S. K. Doorn, “Curvature effects on the E_{33} and E_{44} exciton transitions in semiconducting single-walled carbon nanotubes”, *Phys. Rev B*, 77, 125405, p,1-9, 2008.
- [181] J. G. Duque, H. Telg, H. Chen, A. K. Swan, A. P. Shreve, X. Tu, M. Zheng and S. K. Doorn, “Quantum Interference between the Third and Fourth Exciton States in Semiconducting Carbon Nanotubes Using Resonance Raman Spectroscopy”, *Phys. Rev. Lett.* 108, 117404, p.1-5, 2012.
- [182] Y. Zhao, A. Liao and E. Pop, “Multiband Mobility in Semiconducting Carbon Nanotubes”, *IEEE Electron Device Lett.*, Vol. 30, No. 10, pp.1078-1080, 2009.
- [183] S. Kim and S. Mohammadi, *Single-walled carbon nanotube transistors*, F. Rahman, Ed., Nanostructures in electronics and photonics, Singapore, Pan Stanford Publishing Pte. Ltd., 2008.
- [184] H. Yorikawa, S. Muramatsu, “Electronic structure characteristic of carbon nanotubules”, *Z. Phys. B, Condensed Matt.*, vol. 104, pp. 71–76, 1997.

- [185] H. Yorikawa and S. Muramatsu, “Energy gaps of semiconducting nanotubes”, *Phys. Rev. B*, Vol.52, No.4, pp.2723-2727, 1995.
- [186] H. Yorikawa and S. Muramatsu, “Chirality-dependence of energy gaps of semiconducting nanotubes”, *Solid State Communications*, Vol. 94, Issue 6, Pages 435-437, 1995.
- [187] S. M. Bachilo, M. S. Strano, C. Kittrell, R. H. Hauge, R. E. Smalley, R. B. Weisman, “Structure-Assigned Optical Spectra of Single-Walled Carbon Nanotubes”, *Science*, Vol 298 No. 5602, pp.2361, 2002.
- [188] J. Maultzsch, H. Telg, S. Reich, and C. Thomsen, “Radial breathing mode of single-walled carbon nanotubes Optical transition energies and chiral-index assignment”, *Phys. Rev. B* 72, 205438, 2005.
- [189] A. Jorio, C. Fantini, M. A. Pimenta, R. B. Capaz, Ge. G. Samsonidze, G. Dresselhaus, M. S. Dresselhaus, J. Jiang, N. Kobayashi, A. Grüneis and R. Saito, “Resonance Raman spectroscopy (n,m)-dependent effects in small-diameter single-wall carbon nanotubes”, *Phys. Rev. B* 71, 075401, 2005.
- [190] G. Lanzani, L. Luer, “Carbon Nanotubes: Electronic Structure and Spectroscopy”, *Comprehensive Nanoscience and Technology*, Vol. 1, pp. 23–39, 2011.
- [191] O. Gülseren, T. Yildirim and S. Ciraci, “A systematic ab-initio study of curvature effects in carbon nanotubes”, *Phys. Rev. B* 65, 153405, 2002.
- [192] P. V. Fedotov, D. V. Rybkovskiy, A. I. Chernov, E. A. Obraztsova, and E. D. Obraztsova, “Excitonic Photoluminescence of Ultra-Narrow 7-Armchair Graphene Nanoribbons Grown by a New “Bottom-Up” Approach on a Ni Substrate under Low Vacuum”, *The Journal of Physical Chemistry C*, 124 (47), pp.25984-25991, 2020.
- [193] Ma, C., Xiao, Z., Zhang, H. *et al.* Controllable conversion of quasi-freestanding polymer chains to graphene nanoribbons. *Nat Commun* 8, 14815, 2017.
- [194] Denk, R., Hohage, M., Zeppenfeld, P. *et al.* Exciton-dominated optical response of ultra-narrow graphene nanoribbons. *Nat Commun* 5, 4253, 2014.
- [195] B. V. Senkovskiy, M. Pfeiffer, S. K. Alavi, A. Bliesener, J. Zhu, S. Michel, A. V. Fedorov, R. German, D. Hertel, D. Haberer, L. Petaccia, F. R. Fischer, K. Meerholz, P. H. M. van Loosdrecht, K. Lindfors, and A. Grüneis, “Making Graphene Nanoribbons Photoluminescent”, *Nano Letters* 17 (7), 4029-4037, 2017.

- [196] G. B. Barin, A. Fairbrother, L. Rotach, M. Bayle, M. Paillet, L. Liang, V. Meunier, R. Hauert, T. Dumslaff, A. Narita, “Surface-Synthesized Graphene Nanoribbons for Room Temperature Switching Devices: Substrate Transfer and Ex Situ Characterization” *ACS Appl. Nano Mater.* 2, 2184–2192, 2019.